First-principles Theoretical Analysis of Bulk and Nano-scale Functional Materials

A Thesis

Submitted For the Degree of

DOCTOR OF PHILOSOPHY

in the Faculty of Science

by

Summayya Kouser

THEORETICAL SCIENCES UNIT
JAWAHARLAL NEHRU CENTRE FOR ADVANCED SCIENTIFIC RESEARCH
Bangalore – 560 064

DECEMBER 2015

To my mom

DECLARATION

I hereby declare that the matter embodied in the thesis entitled "**First-principles Theoretical Analysis of Bulk and Nano-scale Functional Materials**" is the result of investigations carried out by me at the Theoretical Sciences Unit, Jawaharlal Nehru Centre for Advanced Scientific Research, Bangalore, India under the supervision of Prof. Umesh V. Waghmare and that it has not been submitted elsewhere for the award of any degree or diploma.

In keeping with the general practice in reporting scientific observations, due acknowledgement has been made whenever the work described is based on the findings of other investigators.

Summayya Kouser

CERTIFICATE

I hereby certify that the matter embodied in this thesis entitled "**First-principles Theoretical Analysis of Bulk and Nano-scale Functional Materials**" has been carried out by Ms. Summayya Kouser at the Theoretical Sciences Unit, Jawaharlal Nehru Centre for Advanced Scientific Research, Bangalore, India under my supervision and that it has not been submitted elsewhere for the award of any degree or diploma.

Prof. Umesh V. Waghmare
(Research Supervisor)

Acknowledgements

I take this opportunity to thank my advisor Prof. Umesh V. Waghmare for his constant encouragement and excellent guidance throughout my Ph.D. Working with him has been a thoroughly enjoyable experience, and his contagious enthusiasm for science has motivated me at various times. His valuable comments and instructions in preparing for seminars and writing papers have helped me immensely. I am extremely grateful for his kindness, endless support and encouragement during my stay at JNCASR.

I would like to express my gratitude to Prof. C.N.R. Rao, Prof. T. Pradeep, Prof. Nacir Tit, Prof. Takeshi Nishimatsu and Prof. Venkatraman Gopalan for the interesting and fruitful scientific collaborations. I have greatly benefited from their expertise, and learned a lot in the process.

I would also like to thank Dr. Shihabudheen M. Maliyekkal, Dr. T. S. Sreeprasad, Dr. Abhishek Kumar Mishra, Dr. Amita Rani, Dr. Anil Kumar, Dr. Nitesh Kumar, Ajmala Shireen, S. R. Lingampalli, Anagha Thannikoth, Uttam Gupta and M. B. Sreedhara for helpful collaborations.

I thank Prof. Shobhana Narasimhan, Prof. Swapan K. Pati, Prof. Subir K Das, Prof. S. M. Shivaprasad, Prof. Chandrabhas Narayana and Prof. Balasubramanian for their instructive and enjoyable courses, and stimulating scientific interactions.

I thank my present and past lab mates Sharmila, Jayshree, Arghya, Sampson, Hembram, Abhishek, Koushik, Meenakshi, Niladri, Anjali, Meha, Vinay, Arpita, Suchitra, Krishnamohan, Pawan, Shashwat, Sandhya and Harish for the co-operative and cheerful environment.

I would like to thank Council of Scientific and Industrial Research, India for a research fellowship and Indo-Korea Science and Technology and JNCASR for funding my foreign visits.

I would like to acknowledge here the support in the form of computational facilities provided by the Centre for Computational Material Science (CCMS), JNCASR using which some of the calculations in the work presented here were performed. I would also like to thank the Complab staff and, Bharathi, Vijay and Amit from CCMS for tending to our problems at any time of the day.

I am grateful to Dhanvantri staff: Dr. Archana, Dr. Kavita, Dr. Chandralekha, Dr. Subba Rao, Ms. Uma, Ms. Tara and Ms. Anjum.

I also extend my gratitude to Academic and Administrative staff for their efficiency and helpfulness.

I take this opportunity to thank all my friends: Ankush, Dhanya, Gayatri, Darshana, Priyank, Rajaji, Loukya, Manjusha, Shajahan, Gangaiah, Sharma, Uttam, Bhawani, Altaf, Humera, Esha, Mounika, Yasmeen, Asma, Sushmita and Reema for the fun times.

I would also like to thank the Hostel staff, Mess workers and Chandraiah canteen for keeping me well fed. Not to forget, Sharanappa and Shivuanna for the hot cup of coffee, and Raju for refreshments till late night.

I am thankful to Aruna mam and Kruti for their warm hospitality, and for making us feel like a family.

I would like to thank my paternal and maternal families for their support and encouragement.

Last but not the least, my mom, brother and Kumar Satyam for their unending support and encouragement.

Synopsis

The development of nano-scale functional materials is at the heart of modern technological break throughs and at the forefront of materials research. With continued advances in computational power, algorithms and techniques of simulations, computational research has become increasingly effective in understanding and complementing experiments. In particular, first-principles Density Functional Theory-based simulations provide fundamental insights into structural stability and properties of a material under the influence of external stimulii. They help in prediction of new materials and exploring their potential for new functionalities. On the other hand, classical atomistic modeling of materials helps in the study of their properties at long time and length scales by using molecular dynamics, possibly through construction of first-principles effective Hamiltonian.

The thesis has broadly three parts based on the kind of technological applications and functionality of the materials studied. The first part consisting of chapter 3 and 4, focuses on the microscopic understanding of the origin of inhomogeneously ordered domain structures in ferroelectric materials like $PbTiO_3$ and $BaTiO_3$ that can be tuned by electrical and mechanical boundary conditions. This has relevance to applications in nano-electro-mechanical systems. The second part consists of chapter 5 and 6, explores the applications of large surface area atomically thin 2-D honeycomb lattices like graphene and 2D-ZnO for removal of toxic materials: pesticides and H_2S gas from the ground water and atmosphere respectively for clean environment and we also study the effect of aliovalent doping in V_2O_3 on its structural stability and electronic structure that is relevant to its use as gas sensor based on transition edge sensing. The third part consists of chapter 7 and 8, presents our work on sulphides (CdS, ZnS and GaS) exploring their properties for photocatalytic applications and tuning the band structure for their use as photocatalysts in conversion of solar energy for water splitting to produce H_2, a green fuel.

List of Publications

(1) S. M. Maliyekkal, T. S. Sreeprasad, D. Krishnan, **S. Kouser**, A. K. Mishra, U. V. Waghmare and T. Pradeep "Graphene: a reusable substrate for unprecedented adsorption of pesticides", *Small* **9**, 273, **2013**.

(2) **S. Kouser**, T. Nishimatsu and U. V. Waghmare, "Ferroelectric domains and diffuse transitions in ultra-thin films of PbTiO3: Effects of strain and electrodes", *Phys. Rev. B* **88**, 064102, **2013**.

(3) **S. Kouser**, U. V. Waghmare and N. Tit, "Adsorption and Splitting of H_2S on 2D-$ZnO_{1-x}N_y$: First-principles Analysis", *Phys. Chem. Chem. Phys.* **16**, 10719, **2014**.

(4) **S. Kouser**, S. R. Lingampalli, P. Chitaiah, A. Roy, S. Saha, U. V. Waghmare and C. N. R. Rao, "Extraordinary changes in the electronic structure and properties of CdS and ZnS by anionic substitution: Co-substitution of P and Cl in place of S ", *Angew. Chem. Int. Ed.* **54**, 8149, **2015**.

(5) **S. Kouser**, A. Thannikoth, U. Gupta, U. V. Waghmare and C.N.R Rao, "2D-GaS as photocatalyst for solar water splitting to produce H_2 ", *Small* **11**, 4723, **2015**.

(6) N. Kumar, M. B. Sreedhara, **S. Kouser**, U. V. Waghmare and C.N.R. Rao, "Effect of nitrogen substitution in V_2O_3 on the metal-insulator transition ", *ChemPhysChem*, **16**, 2745, **2015**.

(7) **S. Kouser**, A. Kumar, K. Rabe, V. Gopalan and U. V. Waghmare, "Origin of gaint dielectric response in 180° domains of $PbTiO_3$ ", *preprint available.*

List of Figures

List of Tables

Contents

Chapter 1

Introduction

Much needed advances in technology to tackle the problems of sustainable energy and environment requires continuous efforts to develop new functional materials and devices that are more energy efficient and eco-friendly. With continued advances in computational power, algorithms and techniques of simulations, computational material research plays a key role in predicting and engineering novel materials with desired properties. In particular, first-principles Density Functional Theory-based simulations provide fundamental insights into structural stability and properties of a material under the influence of external stimulii. On the other hand, classical atomistic modeling of materials helps in the study of their properties at long time and length scales through use of Molecular Dynamics or Monte Carlo simulations, possibly with effective Hamiltonian or model constructed from first-principles.

This thesis is divided into three parts based on the kind of technological applications and functionality of the materials studied. The first part focuses on the microscopic understanding of the origin of inhomogeneously ordered domain structures in ferroelectric materials like $PbTiO_3$ and $BaTiO_3$ that can be tuned with electrical and mechanical boundary conditions. This has relevance to applications in nano-electro-mechanical systems (NEMS). The second part explores applications

of large surface area atomically thin 2-D honeycomb lattices like graphene and 2D-ZnO for removal of toxic materials: pesticides and H_2S gas from the ground water and atmosphere respectively for clean environment, and we also study the effect of aliovalent doping in V_2O_3 on its structural stability and electronic structure that is relevant to its use to its use as gas sensor based on transition edge sensing. The third part presents our work on sulphides (CdS, ZnS and GaS) exploring their properties for photocatalytic applications, and tuning their band structure for their use as photocatalysts in the conversion of solar energy into chemical energy through water splitting to produce H_2, a green fuel.

1.1 Ferroelectrics

Ferroelectric materials exhibit a spontaneous polarization (below a certain temperature) that can be switched by the application of an external electric field. Many important ferroelectrics have a general formula of ABO_3 ($BaTiO_3$, $SrTiO_3$ and $PbTiO_3$ etc) with perovskite structures. At high temperatures, these perovskites have a cubic structure with A cation occupying the corner of the cube, B cation occupies the center of the cube and O occupies the face centers of the cube [Figure 1.1a]. As the temperature is lowered, the inversion symmetry is broken due to the off-centering of the B cation w.r.t BO_6 octahedra leading to a switchable spontaneous polarization [Figure 1.1b]. This property of switchability of polarization and its coupling with strain has many technological applications like capacitors, sensors, actuators, non-volatile memory devices etc [2, 3].

Ferroelectric thin films are known to exhibit a wide range of applications in integrated electronics like multilayer capacitors, nonvolatile FeRAMS, and nano-actuators etc, due to relatively low voltages required to switch the polarization in comparison to their bulk structures [4]. There are efforts to further reduce the

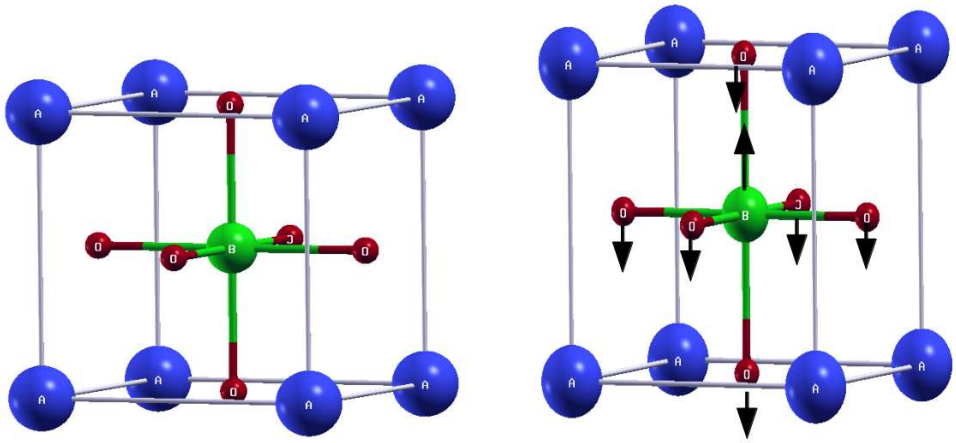

(a) (b)

Figure 1.1: Structures of cubic perovskite (a) and tetragonal peroskite (showing off-centering of B cations w.r.t BO_6 octahedra) (b).

size of ferroelectric thin-film structures. It is now possible to grow atomically controlled epitaxial ultra-thin films with advance vapor deposition techniques including molecular beam epitaxy, sputtering and pulsed laser deposition etc [5]. However, ferroelectricity in structures of finite sizes is very sensitive to electrical and mechanical boundary conditions [6, 7], that are determined by properties of its interface with the substrate on which it is grown and the electrodes. While understanding ferroelectricity at nano-scale has been a fundamental issue [7, 8], a clever choice of an electrode and a substrate can be used effectively in designing ultra-thin films of ferroelectrics with enhanced and optimal properties [5, 9].

Since different polar orientations of polarization are energetically equivalent in general due to cubic symmetry, At nano-scale, ferroelectrics often spontaneously divide into small regions of different polarity, such regions are called “domains” and the boundaries between adjacent domains are called “domain walls” or “domain boundaries.” Domain formation is typically driven by the need to minimize the cost of electrostatic energy due to finite size effects [8, 10, 11]. The structural symmetry of the domain walls is different from that of domains, and hence domains-structure

exhibits different properties from those of the bulk material, and can influence or even dominate the overall behavior of films [2]. Hence, fundamental understanding of the nature of these domains, domain walls and factors affecting their behavior is necessary to improve the device performance.

In this thesis, we first study ferroelectricity in ultra-thin films of $PbTiO_3$ as a function of nature of electrode, thickness and epitaxial strain and show how engineering of the inhomogeneous structures and domains can be achieved. To further understand the effect of domains and domain wall on the properties of the ferroelectrics, we examine dielectric response of the simplest and widely observed 180° domains wall in two well known ferroelectric materials i.e., bulk $PbTiO_3$ and $BaTiO_3$.

1.2 Materials for Environment[†]

The rapid industrialization and urban development have greatly affected our environment by producing hazardous wastes and poisonous gases which are released to the environment. Hence, providing clean air and water is a challenging task. Chemical degradation, filtration, adsorption, biological degradation and coagulation etc are few of the conventional technologies to treat all types of organic and toxic waste [13].

The advent of nanotechnology has immense scope for fabrication of desired nanomaterials with unique functionalities to treat pollutants [14]. Nanomaterials can be effective in environmental remediation and are known to be excellent adsorbents, catalysts and sensors etc due to their large surface areas and high reactivities [13, 14]. The high reactivity of the surface is mainly due to the presence of dangling bonds (low co-ordination number) at the surface, edges and vortices. Apart from that, due to the high mobility of nanomaterials in solution pertaining to their small size, the

[†]Few text excerpts are taken from *Phys. Chem. Chem. Phys.*, 2014 [12]. Reproduced by permission of the Royal Society of Chemistry, URL: http://dx.doi.org/10.1039/C4CP01092B.

whole volume can be quickly scanned with small amounts of nanomaterials. These unique properties make them an important class of materials to help degrade and scavenge pollutants in water and air.

Adsorption is the most frequently used technique to purify water and remove toxic gases from the atmosphere [15]. Adsorption is a process of physical adherence or weak bonding of ions and molecules onto the surface of the adsorbent. The most common and widely used adsorbents are activated carbon, zeolites, silica gel and polymers for removal of heavy metals/toxic materials from contaminated water and polluted air [13]. If the adsorption is mainly physisorption, the species adsorbed onto the nanomaterials can be removed easily making it affordable and reusable [16]. Apart from the treatment of contaminated water and air, *environmental monitoring* is also critical to detect pollutants and develop new remediation technologies. However, this requires rapid reliable analytical tools that can perform sample analysis with minimal sample handling. Nanomaterials based environmental sensors have the potential to detect toxins, heavy metals and organic pollutants in air, water and soil, and are expected to play an increasingly important role in environmental monitoring [17–19].

Since nano-scale activated carbon has advantages over conventional materials due to their (1) unique electronic properties, (2) great capacity to adsorb a wide range of pollutants, (3) large surface area and (4) selectivity towards aromatic solutes [20] and semiconducting metal oxides (SMO) are also natural candidates for gas sensing applications [17–19]. In this thesis, we have studied the adsorption of pesticides and toxic H_2S gas on graphene and 2D-ZnO respectively. We have also studied the effect of anion doping on structural and electronic properties of V_2O_3, to investigate its possible applications in gas sensing based on transition edge sensing.

1.3 Semiconductor Photocatalysts

A photocatalyst is a material that functions as a catalyst (alters the rate of a chemical reaction) when exposed to sun-light. Such materials have a wide range of applications from antifogging, self-cleaning, water purification, gas decomposition and water splitting to produce Hydrogen as a green fuel. .

The present crisis due to dwindling energy resources and production of harmful gases upon combustion of non-renewable fossil fuels requires solutions that tackle issues of energy and environment in an integrated manner. Hydrogen is one of the cleanest sources of energy that produces only water upon burning and has the highest energy density per unit mass. It is considered to be the ultimate fuel for the future. Traditionally, H_2 is generated from water using catalysts in different chemical processes such as electrocatalysis, photocatalysis, or photoelectrocatalysis [21]. Maeda and Domen reported that more than 10,000 photocatalytic water splitting systems with energy conversion efficiency above 10% need to be established to meet even one-third of the energy requirement of human beings by 2050 [22].
Water splitting involves two steps:

$$\text{Oxidation: } 2H_2O \rightarrow 4H^+ + O_2 + 4e^- \text{ (-5.67 eV on SHE)}$$

$$\text{Reduction: } 4H^+ + 4e^- \rightarrow 2H_2 \text{ (-4.44 eV on SHE)}$$

For electrochemical decomposition of water, potential difference between the anode and cathode thus needs to be 1.23 eV. This potential difference is slightly less than the energy of the visible radiation. Therefore, a suitable photocatalyst must have its electronic band positions that straddle the redox potentials [Figure 1.2], i.e., hydrogen evolution reaction (HER) and oxygen evolution reaction (OER) and an energy band gap less than $\approx$1.6 eV to efficiently use solar energy and split H_2O to H_2 [23].

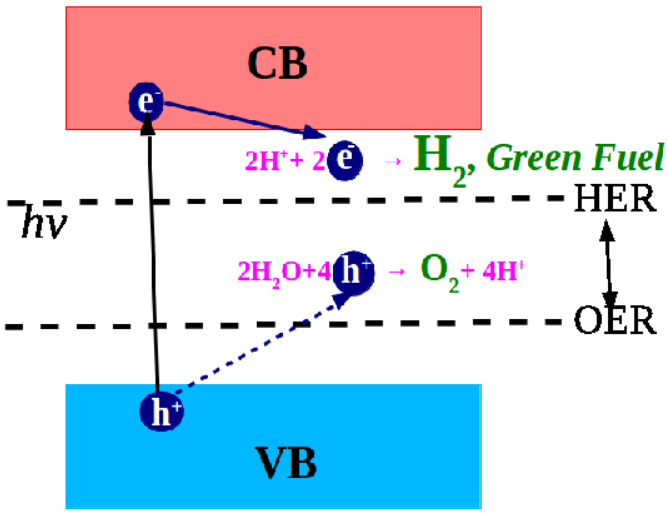

Figure 1.2: A schematic showing band alignment on standard hydrogen electrode (SHE). Copyright (2015) by John Wiley and Sons Inc.

Metal oxides such as $SrTiO_3$, TiO_2, and $NaTaO_3$ [24–28] are non-toxic and have electronic band energies meeting the thermodynamic requirement for water splitting. However, most of them are active only under UV light, which accounts for only about 4% of the solar energy spectrum. So far, only a few efforts have focused on the development of sulfide-based photocatalysts for hydrogen production [29]. Sulphides possess relatively high conduction band positions suitable for reducing H_2O and exhibit better sunlight response than oxides, which originates from (a) the higher valence band positions composed of S $3p$-orbitals and conduction band positions negative enough to reduce H_2O to H_2, and (b) narrow band gaps with better absorptive response to the solar spectrum [30–32].

Chalcogenide semiconductors are some of the common photocatalysts reported till now, for example, ZnS, CdS, $Cd_{1-x}Zn_xS$ solid solutions. Recently layered transition metal sulfides or selenides such MoS_2, $MoSe_2$, and TaS_2 have been found effective in catalyzing solar water splitting [32–35]. Zhuang and Hennig [36] have

theoretically predicted that the monolayer of group III monochalcogenides has ideal band edges for over-all water splitting. These semiconducting photocatalysts are known to exhibit high apparent quantum yield because of their high conduction band positions [37], but cannot efficiently utilize visible light due to the wide band gap with few of them also undergoing photo-corrosion. Numerous efforts (elemental doping and tuning band gap by applying external strain) have been made to improve response to visible light while maintaining the high conduction band. In this present thesis, we have focused on tuning the band gaps for (i) CdS and ZnS by aliovalent anion doping and (ii) 2D-GaS with thickness and external strains, while maintaining their high conduction band position.

1.4 Overview of the Thesis

After a brief introduction to the work carried out in this thesis emphasizing motivation and central ideas in chapter 1. I give a brief overview of the formalism and computational methods in chapter 2.

Part I: Materials for NEMS

In chapter 3, we present a thorough analysis of ferroelectricity in epitaxially strained ultra-thin films of $PbTiO_3$ using MD simulations based on first-principles model Hamiltonian. We have shown that the ferroelectric ordering in these films is often inhomogeneous, characterized by the presence of 90°, flux closure domain structure and rectangular wave-like domain structure. More importantly, such inhomogeneously ordered structure is shown to be tunable with film thickness, epitaxial strain, electric field, and the nature of electrodes, and we show that the origin of this lies in the microscopic strain-phonon coupling. We demonstrate a diffuse phase transition to the flux-closure domain structure as reflected in a rather broad peak

in the temperature-dependent dielectric response. Our work opens up a way of developing diffuse or relaxor ferroelectrics in ultra-thin films with a suitable choice of substrate or electrodes and epitaxial strain.

Having shown that how one may achieve a fine control on the domain structure, we present work in chapter 4 to understand the effect of domain walls on the dielectric properties of $PbTiO_3$ and $BaTiO_3$. We see that presence of domain wall separating domains of opposite (180°) polarization of tetragonal perovskites leads to a giant dielectric response arising in PTO through a soft IR active phonon mode localized on the DW. We find that 180° domains of $BaTiO_3$ have a rhombohedral structure at 0 K similar to its bulk structure, and thus, similar dielectric response. Our findings are relevant to low power applications devices such as non-volatile ultra-high-density memory devices.

Part II: Materials for Environment

In chapter 5(A), we report first-principles theoretical study of adsorption of three of the widely used pesticides present in the environment of developing countries (endosulfan, chlorpyrifos and malathion), on graphene in the presence of water. We confirm large adsorption capacities of the order ∼103 mg g^{-1} of C seen in experiments (Prof. Pradeep group, IIT Madras). Comparative analysis of binary (graphene-water and graphene-pesticide) and ternary (graphene-water-pesticide) complexes showed that the adsorption involves interactions mediated by water molecules, while the direct interaction between graphene and pesticides is rather weak. Our work opens up a route to an effective purification of water from pesticides.

In chapter 5(B), we present a thorough analysis of molecular adsorption of a toxic gas, H_2S, on pristine, defective and N-substituted 2D-ZnO. We find that the binding of H_2S with pristine 2D-ZnO is relatively weaker (adsorption energy E_A = -29 to -36 $kJmol^{-1}$) as it is mainly involves vdW interaction. However, substitution of nitrogen

for oxygen in 2D-ZnO leads to a drastic increase in the adsorption energy (E_A = -152 kJmol^{-1}) resulting in dissociation of H_2S molecule. This originates fundamentally from a strong covalent bonding interaction between an unpaired electron in the *p*-orbital of nitrogen with an electron in *s*-orbital of H. While O-vacancies in 2D-ZnO has little effect on its interaction with H_2S at lower coverages, a strong interaction at higher coverages leads to splitting of H_2S and formation of H_2 molecule. Our work shows that 2D-ZnO has the potential to facilitate capture of toxic H_2S from environment, and its possible conversion to hydrogen, a green source of energy.

In Chapter 6, we determine the effects of anionic (N) substitution on structural and electronic properties of V_2O_3 in corundum and monoclinic phases. This work was done in collaboration with experiments by Prof. C. N. R. Rao's group, JNCASR, where they observed a reduction in metal-insulator transition temperature on N-substitution. Our calculations reveal that anionic (N) substitution and the accompanying oxygen vacancies reduce the energy of high-temperature metallic corundum phase relative to monoclinic one leading to the observed reduction in Nèel temperature along with a drastic decrease in band gap (ΔE_g = 0.4 eV). We even report emergence of weak magnetic moment in monoclinic phase of N-substituted V_2O_3 with O-vacancies, localized on vanadium atoms in the vicinity of oxygen vacancies.

Part III: Materials for Energy Conversion

In Chapter 7, we consider tuning the band gap of important photocatalytic materials like CdS and ZnS for efficient use of visible light through anion substitution, which is expected to bring about major changes in the electronic structure. We find that CdS and ZnS become p and n-type semiconducting with substitution of A (=P or N) and B (=F or Cl) anions respectively. However, the co-substitution is found to be energetically preferred over the individual anionic substitution by more than

1.94 eV per (A,B) pair and A, B atoms preferentially occupy the sites that bond to the same cation (Cd or Zn) atom. The reduction in band gap in co-substituted CdS/ZnS is due to the emergence of an isolated sub-band at the top of valence band, which is primarily contributed by the less electronegative trivalent anions like P and N. In contrast, bands of more electronegative anions (Cl and F) lie deep in energy below the valence band. We find that changes in electronic band gap are more pronounced in hexagonal crystal structure for anion co-substituted CdS and ZnS. In the cubic crystal structure, change in band gap of N, F co-substituted CdS or ZnS is larger than that of P, Cl co-substituted CdS or ZnS, indicating that the effects of anion co-substitution on electronic structure are quite sensitive to the host lattice structure, specific host compound and the nature of dopants. Our findings have stimulated experimental efforts (Prof. C.N.R. Rao's group, JNCASR) in the design of experiments to develop anion-substituted CdS and ZnS.

In chapter 8, we present thickness dependent electronic structure of layered GaS and stability of its polytypes, and show that ultra-thin (thickness < 5.5 nm) films of GaS exhibit electronic structure with valence and conduction bands that straddle the redox potentials of hydrogen evolution and oxygen evolution reactions (OER), making them suitable as photocatalysts for splitting of water and conversion of solar energy into chemical energy in the form of hydrogen. We show that (a) the band gap of a GaS film decreases with increasing thickness making it more efficient in absorption of wider range of solar spectrum, though its valence band edge becomes unfavorable for OER for $t > 5.5$ nm, and (b) the edges of nano-scale flakes of GaS interact more effectively with water molecule leading to their splitting. Thus, we predict that GaS synthesized with controlled thickness and edges should be an efficient photocatalyst for the solar splitting of water. Our prediction is partially verified by experiments (Prof. C.N.R. Rao's group, JNCASR) that show moderate hydrogen evolution in the presence of different sacrificial agents.

As the band gap (E_g^{expt} = 3.05 eV) of monolayered GaS is a bit high for efficient use of visible light, we explored the possibility of tuning the band gap by applying the mechanical strains. We have shown that application of tensile or compressive strain (+5%) reduces the band gap significantly (∼0.7 eV) due to the presence of strong electron-phonon coupling (deformation potential). We report a semiconductor-to-metal phase transition for one of its polytype (BAAC). Our results reveal a strong electron-phonon coupling allows the external mechanical strain to reduce the band gap of semiconducting 2D-GaS in all its polytypes making it more efficient for better photocatalytic activity.

Chapter 2

Methods and Formalism

2.1 First-principles Methods

2.1.1 Introduction

Theoretical analysis of the electronic structure of solid matter (electron and nuclei) provides an understanding of a variety of observed phenomena. In principle, solution of Schrödinger equation of a system which describes its quantum mechanical behavior exactly could provide deep insight into the system. Unfortunately, there is no accurate and efficient method to solve the Schrödinger equation for many electrons system exactly. On this front, the development of Density Functional Theory proposed by Walter Kohn with a few approximations to ease the computational effort has led to significant advances in the theoretical study of the material properties with remarkably good agreement with the experiments. This section gives a brief account of (i) the formalism of first-principles density functional theory, (ii) the technical details of calculating total energies, and (iii) linear response theory or density functional perturbation theory (DFPT) used to determine the response of a system to external perturbations given by second derivatives of total energy.

2.1.2 The Many Body Problem

The Hamiltonian of a many body electron system with interacting electrons and nuclei is:

$$\hat{H} = -\frac{\hbar^2}{2m_e}\sum_i \nabla_i^2 - \sum_{i,I}\frac{Z_I e^2}{|\mathbf{r}_i - \mathbf{R}_I|} + \frac{1}{2}\sum_{i\neq j}\frac{e^2}{|\mathbf{r}_i - \mathbf{r}_j|} - \sum_I \frac{\hbar^2}{2M_I}\nabla_I^2 + \frac{1}{2}\sum_{I\neq J}\frac{Z_I Z_J e^2}{|\mathbf{R}_I - \mathbf{R}_J|}, \tag{2.1}$$

where $\hbar$ is the Planck's constant, m_e and M_I are the masses of electron and I^{th} ion respectively, e is the charge of an electron, and Z_I is the atomic number of the I^{th} ion. $\mathbf{r}_i$ and $\mathbf{R}_I$ are the position vectors of i^{th} electron and I^{th} ion respectively. The first and the third terms in Eq.2.1 are the kinetic and potential energies of electrons respectively, fourth and fifth terms are the kinetic and potential energy of ions respectively, and the second term is the potential energy of interaction between ions and electrons.

As mentioned earlier, one can determine the ground state properties of a system by solving a time independent Schrödinger equation:

$$\hat{H}\psi(\mathbf{R},\mathbf{r}) = \epsilon\psi(\mathbf{R},\mathbf{r}), \tag{2.2}$$

where ϵ and $\psi(\mathbf{R},\mathbf{r})$ are the eigen value and the corresponding eigenfunction of the system. Exact solution of Eq.2.2 is difficult as the wavefunctions are function of $3N$ variables, N being total number of electrons in the system.

To solve Schrödinger equation (Eq.2.2), we make two approximations. Since $M_I \gg m_e$, the kinetic energy of the nuclei is negligible i.e., electrons move much faster than the nuclei and follow the nuclear motion remaining in their instantaneous ground state. This approximation is known as the adiabatic or Born-Oppenheimer approximation [38]. The total wavefunction of a many body electron system can be

written as the product of electronic and nuclear wavefunction as:

$$\psi(\mathbf{R},\mathbf{r}) = \sum_{n} \chi_n(\mathbf{R})\phi_n(\mathbf{R},\mathbf{r}), \tag{2.3}$$

where $\chi_n(\mathbf{R})$ are nuclear wavefunctions independent of electronic position ($\mathbf{r}$) and $\phi_n(\mathbf{R}, \mathbf{r})$ are the electronic wavefunctions of eigenfunctions corresponding to nuclear position ($\mathbf{R}$).

Substituting Eq.2.1 and Eq.2.3 in Eq.2.2, we get:

$$\Big[-\frac{\hbar^2}{2m_e}\sum_i \nabla_i^2 + \sum_{i,I}\frac{Z_I e^2}{|\mathbf{r}_i - \mathbf{R}_I|} + \frac{1}{2}\sum_{i\neq j}\frac{e^2}{|\mathbf{r}_i - \mathbf{r}_j|} + \frac{1}{2}\sum_{I\neq J}\frac{Z_I Z_J e^2}{|\mathbf{R}_I - \mathbf{R}_J|}\Big]\phi_n(\mathbf{R},\mathbf{r}) = E_n(\mathbf{R})\phi_n(\mathbf{R},\mathbf{r}), \tag{2.4}$$

and

$$\Big[-\frac{\hbar^2}{2M_I}\sum_I \nabla_I^2 + E_n(\mathbf{R})\Big]\chi_n(\mathbf{R}) = \epsilon\chi_n(\mathbf{R}). \tag{2.5}$$

We can now solve Eq.2.5 more efficiently by first solving electronic Hamiltonian (equation 2.4) for fixed nuclear positions to obtain the electronic energy $E_n(\mathbf{R})$ (also known as Born-Oppenheimer energy surface). However, solving the many-body electronic Hamiltonian (Eq.2.4) is still not tractable yet, owing to the fact that it is still a function of $3N_e$ variables (N_e is the number of electrons in the system), necessitating further approximations.

2.1.3 Hohenberg-Kohn Theorem

Hohenberg and Kohn (HK) [39] proposed two theorems that address the exact solution of an interacting quantum many body Hamiltonian, Eq.2.4.

Theorem I

The external potential $V_{ext}(\mathbf{r})$ of a many body interacting system can be determined uniquely (within a additive constant) by the ground state density $n^0(\mathbf{r})$.
As a result, all the properties are determined in principle uniquely by ground state n($\mathbf{r}$).

Theorem II

A universal functional of the energy E[n] in terms of the density can be defined for any external potential V_{ext}(r). The global minimum of this functional for a given $V_{ext}(\mathbf{r})$ gives the exact ground state energy and density ($n^0(\mathbf{r})$) of the system.

From these two theorems, energy in Eq.2.4 can be expressed as a functional of $n(\mathbf{r})$ i.e., only 3 variables from $3N_e$ variables. The total energy functional (also known as HK functional) can be written as:

$$\begin{aligned} E_{HK}[n] &= T[n] + V_{ee}[n] + \int d\mathbf{r} V_{ext}(\mathbf{r}) n(\mathbf{r}) + E_{ion-ion}, \\ &= F_{HK}[n] + \int d\mathbf{r} V_{ext}(\mathbf{r}) n(\mathbf{r}) + E_{ion-ion}, \end{aligned} \tag{2.6}$$

where $T[n]$ and V_{ee} are the kinetic and interaction energies of electrons, respectively and $E_{ion-ion}$ is the Coulomb ion-ion interaction energy. F_{HK} is universal since it is only a functional of the density.
These theorems by Hohenberg and Kohn make a significant contribution towards calculating the ground state energy by reducing the minimization problem from 3N dimension to 3 dimension. However, these theorems do not provide a practical way to determine F[$n(\mathbf{r})$] or ground state density $n^0(\mathbf{r})$. Kohn and Sham [40] in 1965 proposed an ansatz to determine the ground state density $n^0(\mathbf{r})$ of an interacting many-body system.

2.1.4 Kohn-Sham Ansatz

Kohn and Sham [40] proposed a formalism of mapping the exact Hamiltonian of an interacting many-body system onto fictitious non-interacting single particle Hamiltonians, which can be tackled more readily. In Kohn-Sham treatment, the total energy functional can be written as:

$$\begin{aligned} E[n(\mathbf{r})] &= \frac{-\hbar^2}{2m}\sum_{i=1}^{N_e}\langle\psi_i|\nabla^2|\psi_i\rangle + \frac{1}{2}\int d\mathbf{r}d\mathbf{r}'\frac{n(\mathbf{r})n(\mathbf{r}')}{|\mathbf{r}-\mathbf{r}'|} + \int d\mathbf{r}n(\mathbf{r})V_{ext}(\mathbf{r}) + E_{xc}[n(\mathbf{r})] + E_{ion-ion}, \\ &= T_s[n(\mathbf{r})] + E_{Hartree}[n(\mathbf{r})] + \int d\mathbf{r}n(\mathbf{r})V_{ext}(\mathbf{r}) + E_{xc}[n(\mathbf{r})] + E_{ion-ion}, \end{aligned} \tag{2.7}$$

where, T_s is the non-interacting kinetic energy of electrons, $E_{Hartree}$ and E_{xc} are the Hartree and exchange-correlation energies. The Kohn-Sham non-interacting single particle Hamiltonian is given as:

$$H_{KS} = -\frac{\hbar^2}{2m}\nabla^2 + V_{KS}(\mathbf{r}), \tag{2.8}$$

where, V_{KS} is the Kohn-Sham potential for non-interacting system given as:

$$V_{KS}(\mathbf{r}) = V_{ext}(\mathbf{r}) + \int d\mathbf{r}'\frac{n(\mathbf{r}')}{|\mathbf{r}-\mathbf{r}'|} + V_{xc}[n(\mathbf{r})], \tag{2.9}$$

where, the first term is the external potential, the second term is the Hartree potential and the third term is the exchange-correlation potential. Equation based on the single particle Kohn-Sham Hamiltonian is given as:

$$H_{KS}\phi_i(\mathbf{r}) = \epsilon_i\phi_i(\mathbf{r}), \tag{2.10}$$

and the ground state charge density $n(\mathbf{r})$ is represented in terms of one electron wavefunctions, $\phi_i(\mathbf{r})$ as

$$n(\mathbf{r}) = 2\sum_{i}^{N_e/2} |\phi_i(\mathbf{r})|^2. \tag{2.11}$$

Since Kohn-Sham equation (2.10) are nonlinear, a self consistent iterative scheme used to solve them, as illustrated in Figure 2.1.

2.1.5 Exchange correlation energy

The exchange-correlation interaction (E_{xc}) is defined as the difference between the exact energy and the Hartree-Fock energy. Formally, the exchange-correlation energy can be defined as:

$$E_{xc}[n(\mathbf{r})] = T[n((r)] - T_0[n(\mathbf{r})] + E_{ee}[n(\mathbf{r})] - E_{Hartree-Fock}[n(\mathbf{r})], \text{ and} \tag{2.12}$$

The exact form of exchange-correlation energy functional is not known and hence approximate functionals are used to calculate various properties of the system. We have primarily used two approximations to determine the exchange-correlation energy *i.e.,* local density approximation (LDA) and generalized gradient approximation (GGA).

The simplest approximation for $E_{xc}[n(\mathbf{r})]$ is the local density approximation which approximates that the exchange-correlation density at each point is the same as in a homogeneous electron gas of the same density given as:

$$E_{xc}^{LDA} = \int d\mathbf{r} n(\mathbf{r}) \epsilon_{xc}^{homo}(n(\mathbf{r})), \tag{2.13}$$

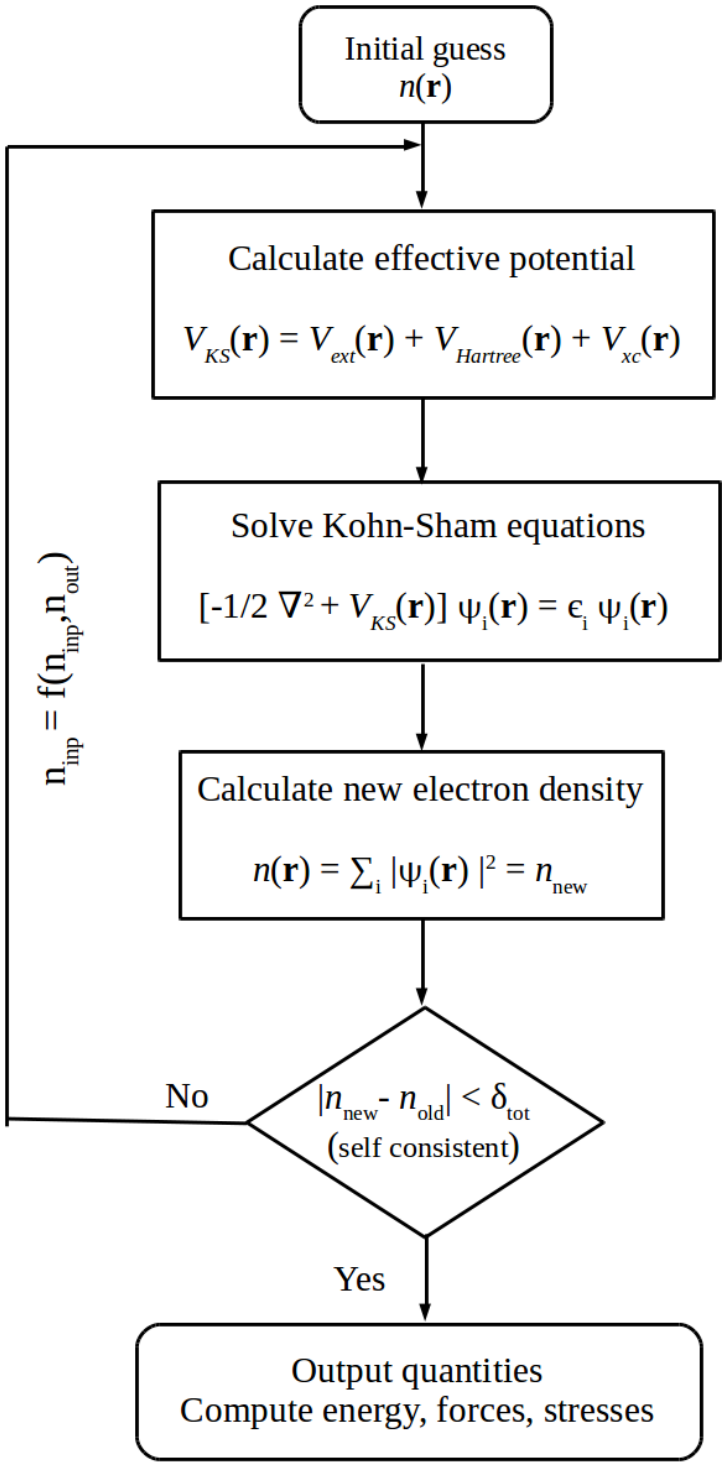

Figure 2.1: Flow chart showing the self-consistency loop for the iterative solution of the Kohn-Sham equations.

where $\epsilon_{xc}^{homo}(\mathbf{n})$ is the exchange-correlation energy per particle of a homogeneous electron gas of density. The approximate forms of ϵ_{xc}^{homo} is obtained from interpolation between quantum monte carlo calculations of Ceperly and Alder [41] and random phase approximation (RPA) calculation, and later parametrized by Perdew and Zunger [42]. Though the corrections to the exchange-correlation energy arising from inhomogeneities in the electron density about $\mathbf{r}$ are ignored, LDA describe many of the properties of weakly correlated systems like semiconductors and homogeneous electron gas reasonably well.

For inhomogenous charge densities, where charge density varies rapidly in space, the GGA has been proved to be an improvement over LDA in estimating total energies. The exchange-correlation energy is expressed in terms of the gradient and spatial derivatives of the charge density as:

$$E_{xc}^{GGA} = \int d\mathbf{r} n(\mathbf{r}) \epsilon_{xc}^{hom}(n(\mathbf{r}), \nabla n(\mathbf{r})). \tag{2.14}$$

Some of the widely used approximations of exchange-correlations energy functional within GGA are the ones developed by Perdew and Wang (PW91) and Perdew, Burke and Ernzerhof (PBE) etc [43, 44].

2.1.6 Basis set

To solve Kohn-Sham equations, electronic wavefunctions are usually expanded in terms of set of a suitable basis function. A variety of basis sets can be used in the expansion of wavefunctions, i.e. plane waves, atomic orbital and mixed basis (plane-waves + atomic orbital).

Due to the simplicity and absence of Pulay forces, plane wave basis ($e^{i(\mathbf{k}+\mathbf{G}).r}$) is an excellent choice for the description of single particle wavefunctions (ϕ_i) in metals or

semiconductors as follows:

$$\phi_i(\mathbf{r}) = \sum_{|G|} C_{i,\mathbf{k}+\mathbf{G}} e^{i(\mathbf{k}+\mathbf{G}).r}, \tag{2.15}$$

where, k is a wavevector at which the Kohn-Sham equations are solved and G is a reciprocal lattice vector [45, 46]. This expansion is infinite in principle and hence needs to be truncated to make it computationally feasible. A kinetic energy cutoff is used to truncate the finite mesh of **G** vectors is used. The maximum number of plane waves in a basis set ($\mathbf{G}_{cut}$) is determined by an energy parameter E_{cut} using the following relation:

$$\frac{\hbar^2}{2m}|\mathbf{k}+\mathbf{G}|^2 < \frac{\hbar^2}{2m}|\mathbf{k}+\mathbf{G}_{cut}|^2 = E_{cut}. \tag{2.16}$$

The value of E_{cut} is determined by checking the convergence of the total energy with E_{cut}.

On the other hand, the atomic orbital basis captures the essence of atomic, orbital character of extended wavefunctions. Mixed basis is a more general basis where the atomic-like features are incorporated near the core, and smoothly varying (plane waves) away from the nucleus. All the calculations in this thesis are done using plane wave basis sets. The size of the Hamiltonian matrix depends on the size of the basis set, which can be made further smaller by using ultrasoft pseudopotentials (see next section).

2.1.7 Pseudopotentials

The electrons that are tightly bound to the nucleus are called core electrons and have highly localized wavefunctions that oscillate rapidly in space. For an all-electron DFT calculation, one would require a very large number of plane waves for an

accurate description of the core states, making it computationally expensive. One can get rid of this problem by using a pseudopotential, which replaces the true potential of core electrons and nucleus of an atom with a hypothetical potential, and avoid explicit treatment of the core electrons. The justification for such a seemingly drastic approximation is that it is generally the valence electrons that determine the bonding and many properties of a system with little or no contribution from its core electrons.

A pseudopotential is constructed by considering a cutoff radius (r_c) beyond which that the pseudo-wavefunction matches exactly with the true wavefunction [Figure 2.2]. Inside this core radius, the pseudo wavefunction is nodeless and goes smoothly to zero, so as to get rid of large Fourier components.

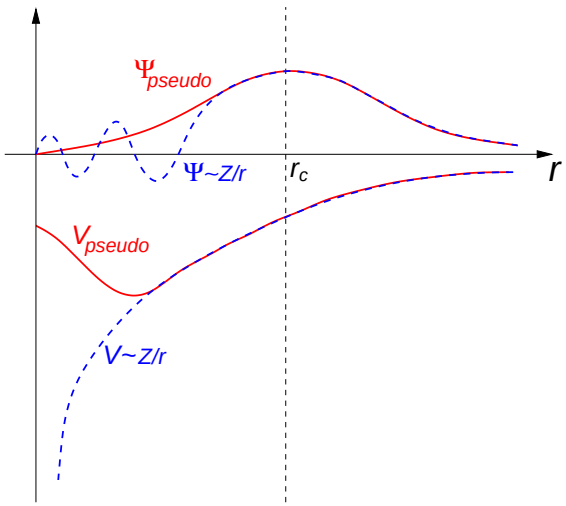

Figure 2.2: Schematic representation of an all electron potential (dotted line) and pseudopotential (solid line) with corresponding wavefunctions.

If the total charge within the cutoff radius of pseudo wavefunctions is the same as the corresponding all-electrons wavefunctions, the pseudopotential is known as

norm-conserving pseudopotential [47]. Pseudopotentials can be made even softer by generalizing the constraint of norm conservation while maintaining transferability, these are called as ultrasoft pseudopotentials [47]. These further reduce the computational cost. However, the charge density has to be augmented in the core region in order to recover the full electronic charge, necessitating a separate energy cut-off on the basis for its representation.

2.1.8 Dispersion interactions

Though GGA describes inhomogeneous charge density of molecular systems, it does not describe non-local long-range electron correlations that are responsible for van der Waals (vdW, dispersive) forces. These interactions between atoms and molecules decay rapidly in space and play an important role in many chemical systems [48]. Several methods have been developed in recent years to include these dispersive interactions in DFT calculations. These are broadly divided into two classes, (1) one class of methods adds the dispersion interaction as semi-empirical corrections on top of existing local functionals, and (2) another class of methods attempts to develop non-local exchange-correlation energy functionals that can incorporate the London interactions [49, 50]. In this thesis, to account for such weak interactions between substrate and molecules (pesticides H_2S and H_2O), we have used parametrized DFT-D2 treatment of Grimme [49]. This gives a fairly accurate treatment of London dispersion interactions at relatively low computational cost, and we briefly describe the formulation below.

The total energy with dispersion correction is given as,

$$E_{DFT-D2} = E_{KS-DFT} + E_{disp}, \tag{2.17}$$

where E_{KS-DFT} is the self consistent Kohn-Sham energy (Eq.2.7) and E_{disp} is the empirical dispersion correction which is given as,

$$E_{disp} = -s_6 \sum_{I=1}^{N_{at}-1} \sum_{J=I+1}^{N_{at}} \frac{C_6^{IJ}}{R_{IJ}^6} f_{damp}(R_{IJ}) \tag{2.18}$$

Here, N_{at} is the number of atoms in the system, C_6^{IJ} denotes the dispersion coefficient for a pair of atoms I and J, s_6 is a global scaling factor that depends only on the approximate functional used, and R_{IJ} is an interatomic distance. To avoid the singularities for small R_{IJ}, a damping function (f_{damp}) is used, given as,

$$f_{damp} = \frac{1}{1 + e^{d[(R_{IJ}/R_r)-1]}}. \tag{2.19}$$

Here, R_r is the sum of atomic van der Waals radii, The parameter d determines the dispersion corrections to the total energy and is fixed to 20 by Grimme to give accurate dispersion energies, but still maintaining negligible energies for typical covalent bonding situations. The dispersion coefficient C_6^{IJ} for a given pair of atoms I and J, is written as a geometric mean of the individual coefficients:

$$C_6^{IJ} = \sqrt{C_6^I C_6^J}. \tag{2.20}$$

The dispersion coefficients are calculated for an atom species a with ionization potential I_p and static dipole polarizability α (determined using DFT/PBE0 [51]) using the relation:

$$C_6^a = 0.05 N_a I_P^a \alpha_a, \tag{2.21}$$

where N_a has values 2, 10, 18, 36, and 54 for atoms from rows $1-5$ of the periodic table respectively.

2.1.9 Density Functional Perturbation Theory

Many interesting physical properties (response functions) correspond to response to application of an external perturbation to the system. The response functions are second, third, or higher order derivatives of the total energy with respect to applied perturbations (λ: atomic displacements, strain, external electric or magnetic fields etc). Few of physical properties of interest related to derivatives of the total energy are forces, stresses, phonons, Born effective charges, dielectric constant, elastic constants, Raman cross-sections etc.

Density Functional Perturbation Theory (DFPT) provides a linear response technique to compute the second and third derivatives of the ground state energy w.r.t. external perturbation ($\lambda \equiv \lambda_i$). The first and second derivatives of the ground-state energy are given as,

$$\frac{\partial E}{\partial \lambda_i} = \frac{\partial E_{ion-ion}}{\partial \lambda_i} + \int d\mathbf{r} \frac{\partial V_{ext}}{\partial \lambda_i} n(\mathbf{r}),$$

$$\frac{\partial^2 E}{\partial \lambda_i \partial \lambda_j} = \frac{\partial^2 E_{ion-ion}}{\partial \lambda_i \partial \lambda_j} + \int d\mathbf{r} \frac{\partial^2 V_{ext}}{\partial \lambda_i \partial \lambda_j} n(\mathbf{r}) + \int d\mathbf{r} \frac{\partial n(\mathbf{r})}{\partial \lambda_i} \frac{\partial V_{ext}}{\partial \lambda_j} \tag{2.22}$$

Thus, we need to calculate the response of electron density, $\partial \mathrm{n}(\mathbf{r})/\partial \lambda_i$, which can be obtained by linearizing equation 2.11 as

$$\Delta n(\mathbf{r}) = 2Re \sum_{i}^{N_e/2} \psi^*(\mathbf{r}) \Delta\psi(\mathbf{r}). \tag{2.23}$$

where $\Delta \mathrm{n}(\mathbf{r})$ is $\partial \mathrm{n}(\mathbf{r})/\partial \lambda$, the variation in wavefunction, $\Delta\psi_i(\mathbf{r})$ can be obtained by standard first-order perturbation theory given by Sternheimer equation [52]:

$$(H_{KS} - \epsilon_i)|\Delta\psi_i\rangle = -(\Delta V_{KS} - \Delta\epsilon_i)|\psi_i\rangle, \tag{2.24}$$

where ΔV_{KS} and $\Delta\epsilon_i$ are the first order variations of Kohn-Sham effective potential and eigenvalues (ϵ_i) respectively, given by,

$$\begin{aligned} \Delta V_{KS}(\mathbf{r}) &= \Delta V_{ext}(\mathbf{r}) + e^2 \int d\mathbf{r}' \frac{\Delta n(\mathbf{r}')}{|\mathbf{r}-\mathbf{r}'|} + \frac{dV_{xc}}{dn}\Big|_{n=n(\mathbf{r})} \Delta n(\mathbf{r}); \\ \Delta\epsilon_i &= \langle\psi_i|\Delta V_{KS}|\psi_i\rangle. \end{aligned} \tag{2.25}$$

As the electron density responds to only those perturbations that couple both the occupied and empty states, equation 2.24 can be defined in terms of empty states as,

$$(H_{KS} - \epsilon_i)|\Delta\psi_i\rangle = -\hat{P}_{empty}\,\Delta V_{KS}|\psi_i\rangle, \tag{2.26}$$

where $\hat{P}_{empty}$ is the projector onto the empty states manifold defined in terms of occupied states ($\hat{P}_{occ}$) given by,

$$\hat{P}_{empty} = 1 - \hat{P}_{occ};\ where \hat{P}_{occ} = \sum_{i=1}^{N_e/2} |\psi_i\rangle\langle\psi_i|. \tag{2.27}$$

By solving this set of linear equations (Eq.2.25), one can calculate the relevant response properties of the system efficiently and with reasonable accuracy [53, 54].

2.2 Molecular Dynamics

First-principles based Density Functional Theory techniques are quite effective in determining ground state structural and electronic properties. However, computation of statistical phenomena relevant for systems that undergo temperature dependent structural phase transitions involves longer length and time scales. Statistical properties of a system can be calculated from its partition function, which requires the knowledge of material specific Hamiltonian in terms of relevant degrees of freedoms (DoFs). This Hamiltonian can be readily simulated using Molecular Dynamics or

Monte Carlo methods to study temperature dependent phenomena.

In this thesis, we are interested in temperature dependent properties of epitaxial ultra-thin films of $PbTiO_3$ under different boundary conditions mainly due to interface between ferroelectric films and the substrates on which it is grown and the electrodes. A ferroelectric transition involves very small structural distortions from its high symmetry cubic structure that involve long wavelength acoustic modes and low energy TO modes. Based on these observations, Waghmare and Rabe [55] have obtained a simple effective Hamiltonian for $PbTiO_3$ that captures the relevant physics.

Through this effective Hamiltonian of $PbTiO_3$, the energy surface is expressed as a symmetry-invariant Taylor expansion in terms of atomic displacements (u_i) with respect to the high symmetry paraelectric phase. As long wavelength acoustic modes and only low energy unstable transverse modes are relevant to these phase transitions, high frequency phonons are essentially integrated out from the partition function with a trivial contribution to the free-energy. The first order term in the Taylors expansion (linear in u_i) vanish as per symmetry requirement, the second order terms gives the force constants relevant to the unstable optic and acoustic modes, while higher order terms in u_i's capture the anharmonic interactions necessary for the thermal stability of cubic phase at high temperature *i.e.*, strain-phonon coupling, elastic energy etc. The 15 DoFs per unit cell are reduced by mapping localized atomic displacements to 3-D Wannier vector (η_i) and expressing the energy surface as Taylors expansion of optical u_i's, acoustic η_i's and strain, reducing the number of DoFs per unit cell to 6. We have used this first-principles effective Hamiltonian of $PbTiO_3$ in Molecular Dynamics as implemented in FERAM [56]. As the calculation of long-range dipolar interactions energy is computationally expensive, we use mixed space molecular dynamics to simulate systems at large scales on moderate computing resources by treating them in the reciprocal space, reducing

the computational time from $O(N^2)$ to $Nlog(N)$, where N is the size of simulation cell [57]. To model a ferroelectric film sandwiched between two electrodes, we have treated electrodes as electrostatic mirrors within doubly periodic boundary conditions [56].

Part I

Materials for NEMS

Chapter 3

Strain engineering of ferroelectricity and domain structure in ultra-thin epitaxial films of $PbTiO_3$*

3.1 Introduction

With a strong coupling of their spontaneous electric dipole (polarization) with external mechanical and electric fields, ferroelectric materials are used in smart structures and applications that include sensors, actuators, transducers and memory devices. This coupling also makes them sensitive to various boundary conditions, that qualitatively change their structure and technologically important properties particularly when the size of their devices is small [3]. At nano-scale, novel structures consisting of domains of differently oriented polar phases of ferroelectrics can get stabilized, giving rise to new functionalities [2]. The interface between the domains is called as a

*This work has been published in *Phys. Rev. B* [58]. Copyright (2013) by the American Physical Society, URL: *htpp* : *//dx.doi.org*/10.1103/*PhysRevB*.88.064102.

"domain wall", and it is now possible to image the atomic-scale structure of a domain wall [59, 60]. Recent experiments have shown rather interesting domain structure in normal and relaxor ferroelectrics, and formation of vortex nanodomain arrays at ferroelectric heterointerfaces [61–65]. Such heterogeneously ordered structures of ferroelectrics, stable primarily at nano-scale, naturally affect switching and dielectric properties of ferroelectrics that are relevant to ultrahigh-density nonvolatile memory devices. It is important to understand how different types of domains and domain walls form, and how they affect the properties of nano-ferroelectrics.

Fundamental to structure and properties of ferroelectrics are the structural phase transitions they undergo, and there have been many theoretical [66–68] and experimental [8, 69] studies to determine and understand how these transitions are influenced by the boundary conditions at nano-scale. For example, mechanical clamping of ultra-thin films results in changes of the sequence of ferroelectric phases and transition temperatures due to strong polarization-strain coupling [65, 70–73]. Strain engineering of Ferroelectric domains was demonstrated for $BaTiO_3$ films and $BaTiO_3$ nanodot using phase field models [74–77]. Such models do not adequately capture effects of the nature of the substrate, specifically how well it provides free carriers to compensate surface charges of a ferroelectric, which plays an important role in the ferroelectricity of the film [8, 69]. Proper choice of the film thickness, strain and electrodes leads to phenomena such as ferroelectric tunnel junction and giant electro resistance enabling newer functionalities [78].

Our goal here is to determine and understand nano-scale ferroelectricity and domain structure of $PbTiO_3$, an end-member of the lead zirconate titanate family, one of the most important technological materials. It undergoes a single phase transition from cubic paraelectric phase to tetragonal ferroelectric phase with polarization along (001) direction at 763 K [79]. Strain-temperature phase diagrams for ultra-thin films of $PbTiO_3$ have been predicted earlier using Landau theory and

phase field simulations [75]. However, the atomically sharp domain wall structure of a nano-thin film is not quite readily captured by such analysis. Dependence of ferroelectricity on the thickness of $PbTiO_3$ films grown on different substrates was studied experimentally, and stripe-like domain structure was observed by Fong *et al* [8, 69]. Evidently, the nature of ferroelectric phases and ordering into domains in these ultra-thin films are influenced by thickness, epitaxial strain and the electrostatic screening of the surface charges by substrate and electrodes, and their mechanisms need to be understood.

In this chapter, we present a thorough analysis of the effects of electrical and mechanical boundary conditions on ultra-thin films of $PbTiO_3$ using first-principles effective hamiltonian in molecular dynamics with Ferroelectrics and Relaxor Analyzing Machine (FERAM) [56] code. We determine thickness (l) dependent ferroelectricity and temperature (T)-epitaxial strain (η) phase diagrams of $PbTiO_3$ films sandwiched between perfect and imperfect electrodes. We show that a stripe domain phase stable at low temperatures leads to a diffuse phase transition characterized by a broad peak in dielectric constant of these films sandwiched between imperfect electrodes. Our results reveal a possible mechanism of the relaxor behavior of ferroelectrics in their nano-scale domain structure. Secondly, we show that the strain-phonon coupling is responsible for the domain structure and these properties emerging in the nano-scale films of $PbTiO_3$.

3.2 Computational Details

Our Molecular Dynamics (MD) simulations are based on a model Hamiltonian of $PbTiO_3$ derived from first-principles [55], as implemented in the FERAM code [56]. This hamiltonian captures the quadratic inter-site and local anharmonic interactions between local dipolar degrees of freedom, their coupling with local and global

strain, and elastic energy associated with the strain degrees of freedom. We treat electric dipoles and their electrostatic images in the electrodes using mirror or doubly periodic boundary conditions with systems of size 16 x 16 x L_z unit cells, where L_z=2($l+d$), l is the number of unit cells in z-direction and d indicates thickness of a dead layer between the film and electrodes in terms of unit cell parameters [Figure 3.1a], and models the nature of electrodes: a film sandwiched between *perfect* electrodes ($d = 0$: no dead layer) has a vanishing depolarization field due to complete compensation of surface charges by the electrode, and a film sandwiched between *imperfect* electrodes ($d \neq 0$) has a nonzero depolarization field scaling as $\frac{d}{l+d}$. We worked with a gap with $d = 1$ to model imperfect electrodes (refer Ref.[25] for detail schematic). We have considered film thickness (l) ranging from 2 to 64 unit cells (8-254 nm) and a wide range of epitaxial strains from -0.02 to 0.02. We carry out both heating and cooling simulations in steps of +5 K and -5 K respectively. A heating simulation is started with a state with polarization along z-axis in the initial configuration, while a cooling simulation is started with a random paraelectric state as the initial configuration. At each temperature, the system is thermalized with 40,000 time steps and thermodynamic averaging is done using configurations at subsequent 60,000 time steps. We use a time step of $\Delta t = 2$ fs employing a Nosé-Poincaré thermostat [80], thus our typical cooling/heating simulation corresponds to evolution of the system for over tens of nanosecond.

3.3 Results and Analysis

3.3.1 Thickness dependent ferroelectricity

We first demonstrate how the ferroelectric transition in $PbTiO_3$ depends on the thickness of its film and the electrodes interfacing with it. When the electrodes are *perfect* ($d = 0$), *i.e.*, they are effective in completely screening the bound charges

at the surfaces of the film, we find that (a) transition occurs from the cubic paraelectric (PE) phase to ferroelectric tetragonal phase with polarization perpendicular to the plane of the film (P_z), (b) the transition temperature T_C of the film under -0.5 % epitaxial strain saturates to a value for $l > 24$ (about 10 *nm* thickness, Figure 3.1a), higher than the bulk transition temperature of 763 K, and (c) while T_C drops rapidly (by more than 30 %) with reducing thickness, ferroelectricity survives down to less than a *nm* thick film. However, the nature of this transition changes drastically when the electrodes are *imperfect* ($d = 1$) and hence the surface charges are only partially screened resulting in a nonzero depolarization field. In this case, the transition occurs from the PE phase to an inhomogeneously ordered phase, "*flux closure domain phase*", as was reported experimentally [61, 62]. The transition temperature is somewhat (by 100 K) lower than the one for films interfacing with perfect electrodes, and its dependence on thickness is rather similar [Figure 3.1b]. We fit the transition temperature as a function of thickness to the Michaelis-Menten function [81] commonly used in enzyme catalysed reactions and known for glass transitions [82]:

$$T_C(l) = \frac{T_C^{max} l}{\zeta + l} \tag{3.1}$$

where T_C^{max} is the T_C in the bulk limit, ζ is a fitting parameter (T_C^{max}=976 K and 945 K, $\zeta = 2.28$ and 5.96, for films with perfect and imperfect electrodes respectively). Secondly, the stripe-type domains in this low temperature phase are very similar to those observed earlier in $PbTiO_3$ [8, 61–63, 69]. We note that the domain wall here is in the $\langle 100 \rangle$ plane, in contrast to that in ultra-thin film of $BaTiO_3$, where it is in the $\langle 110 \rangle$ planes [56, 83]. The origin of the stability of flux-closure stripe domain phase is indeed in the reduced depolarization field and energy cost $P.E_d$ (energy per unit volume), where P is the polarization, E_d is the depolarization field given by $4\pi \frac{d}{l+d} P_z$ associated with it [61]. Indeed, our analysis reveals that care

must be taken in assessing the size limit on ferroelectricity [84], as an inhomogeneous ordering may win if the electrodes are not good metals.

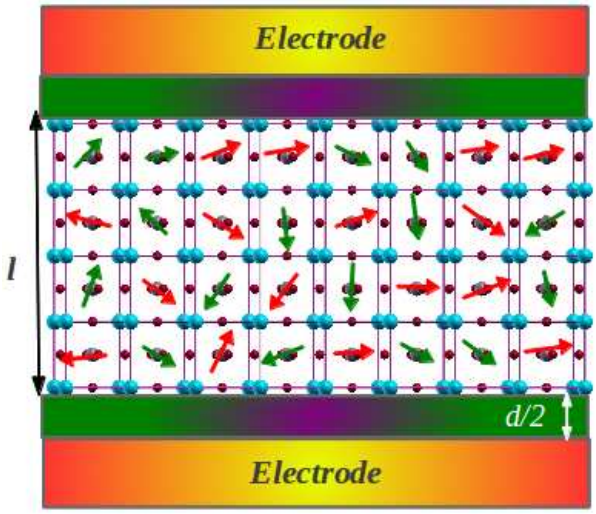

(a)

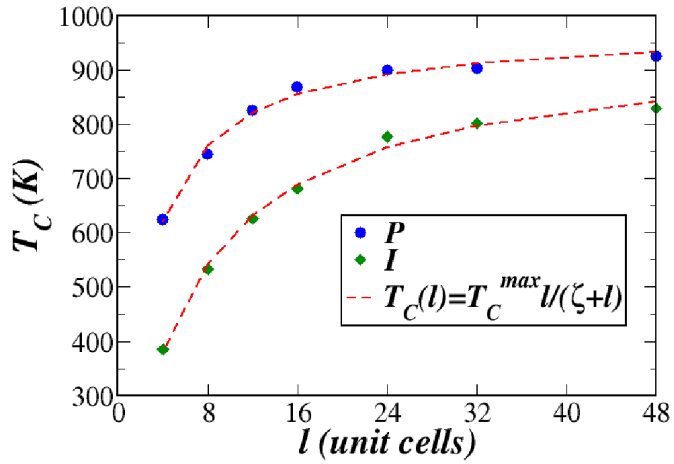

(b)

Figure 3.1: Schematic of a system (a) used to simulate a film sandwiched between electrodes. Thickness dependent ferroelectric transition temperature of $PbTiO_3$ films (b) sandwiched between perfect (P, d=0) and imperfect electrodes (I, d=1) under epitaxial strain, $\eta = -0.005$, dotted line shows the Michaelis-Menten based fit. Copyright (2013) by the American Physical Society.

Dielectric response is an important property of ferroelectrics that (a) makes them useful in capacitive memories, and (b) bears the primary signature of onset of ferroelectric ordering. Dielectric constant has been calculated using the expression

of susceptibility in terms of fluctuations in polarization:

$$\chi = \frac{\Omega}{\varepsilon_o k_B T}[< P^2 > - < P >^2] \tag{3.2}$$

Indeed, the onset of ferroelectric order with polarization along z and later at lower temperatures along x, y directions is accompanied by diverging dielectric response of the films sandwiched between perfect electrodes [Figure 3.2a]. The ordering of polarization in the plane of the film is a new feature that emerges in the nano-scale epitaxial films of $PbTiO_3$ (note that its bulk form exhibits a transition to only the tetragonal, $P_z \neq 0$). The dielectric signature of ordering to flux closure stripe domain phase in the films (epitaxial strain of -0.5 %) interfacing imperfect electrodes is quite different [Figure 3.2b]: the dielectric constant exhibits a very broad peak as a function of temperature, characteristic of a diffuse phase transition. A Landau-Ginzburg-Devonshire theory of a ferroelectric sandwiched between electrodes [85,86] has been used to understand the mechanism of smearing of a ferroelectric transition in thin films [87]. In these works, smearing was associated with surface or interfaces or other defects that give rise to a field that couple with polarization. In the present work, the electrostatic nature of the interface of the film with electrodes favors formation of inhomogeneous distribution of polarization, *i.e.* domains, which are responsible for a diffuse phase transition. The discontinuous change in the slope of strain as a function of temperature marks the initiation of formation of domains of ordered states. However, the broad peak in the dielectric constant is at a slightly lower temperature, where the polarization fluctuations relevant to formation of domain structure are most prominent. As the estimation of T_C involves large error and can be tricky in this case, we determined it as the temperature at which the slope of strain, η_{zz} as a function of T changes [Figure 3.2b]. The diffuse character

of the transition becomes weaker (the dielectric peak becomes sharper) with an increase in the film thickness (as $E_d \to 0$) (Inset of Figure 5.7), and marks a transition to a phase with stripe domain. The broad dielectric peak was reported earlier in $BaTiO_3$ films and attributed to the surface induced dipole inhomogeneities [66, 88]. We note that T_a and T_b are the Curie temperatures corresponding to dipolar ordering along a and b-axis respectively (we use T_{ab} as the average of T_a and T_b). These temperatures are clearly identified as those where the xx and yy components of the dielectric response diverge in the films with perfect electrodes [Figure 3.2a]. On the other hand, the in-plane dielectric response of the films with imperfect electrodes is unusual with ($\varepsilon_{xx} \neq \varepsilon_{yy}$). The origin of this is in the fact that the symmetry group of the flux closure domain phase which does not include C_{4z} and other symmetries that transform a direction to b. We find that the domain structure is also associated with in-plane ordering of polarization. In contrast to the flux-closure domains which are controlled by the screening ability of the electrode, the in-plane domain structure involves mainly 90° domains and is controlled mainly by the strain, and only weakly by the electrodes, similar domains were reported for Bulk $PbTiO_3$ [89]. Visualization of the 3 ordering of polarization at two different epitaxial strains for films ($l = 8$) sandwiched between perfect ($d = 0$) electrodes at T=145 K shows no in-plane domains at compressive epitaxial strain, $\eta = -0.01$ [Figure 3.3a], while we clearly see a 90° domain structure at a tensile strain of $\eta = 0.01$ [Figure 3.3b]. The domain walls in this case are perpendicular to [110]-type directions. A transition from a ferroelectric phase with P_z to the one with 90° domains in the ab-plane is accompanied by fluctuations in polarization in the ab-plane near T_{ab} and divergences in ε_{xx}, ε_{yy} [Figure 3.2].

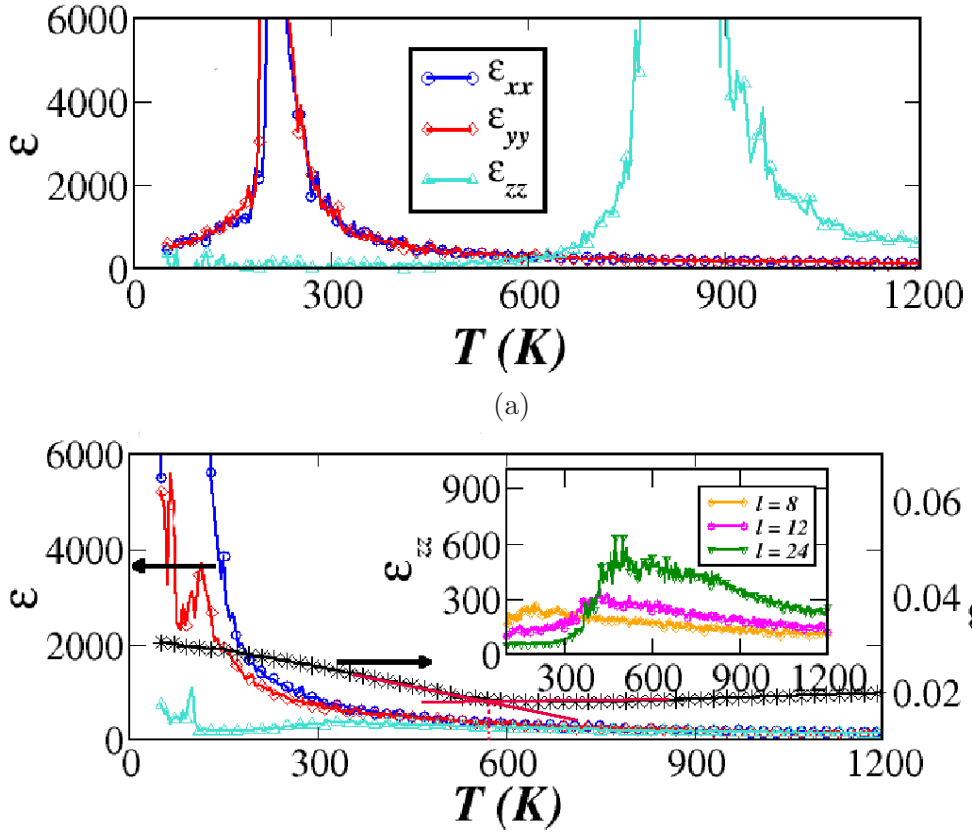

Figure 3.2: Temperature dependence of dielectric constant of a film ($l = 12$), sandwiched between (a) perfect electrodes ($d = 0$) and (b) imperfect electrodes ($d = 1$). Change in the slope of temperature dependent strain η_{zz} (highlighted by red lines) is used in the latter to detect T_C; zz-component of dielectric constant of films of different thickness (l) sandwiched between imperfect electrodes, under $\eta = -0.005$ is shown in the inset (obtained from cooling simulations). Copyright (2013) by the American Physical Society.

3.3.2 Temperature-epitaxial strain phase diagrams

We now discuss the temperature-epitaxial strain phase diagrams of $PbTiO_3$ films interfaced with imperfect ($d = 1$) [Figure 3.4a] and perfect electrodes ($d = 0$) [Figure 3.5a] determined here for films of thickness of 8 unit cells (3.2 nm) and $-0.02 \leq \eta \leq 0.02$. As pointed out earlier, the nature of electrodes qualitatively changes the ordering of polarization in z direction, while its effects on the ordering of in-plane components (at temperatures T_a, T_b) are weak. Thus, the T_{ab} line, below

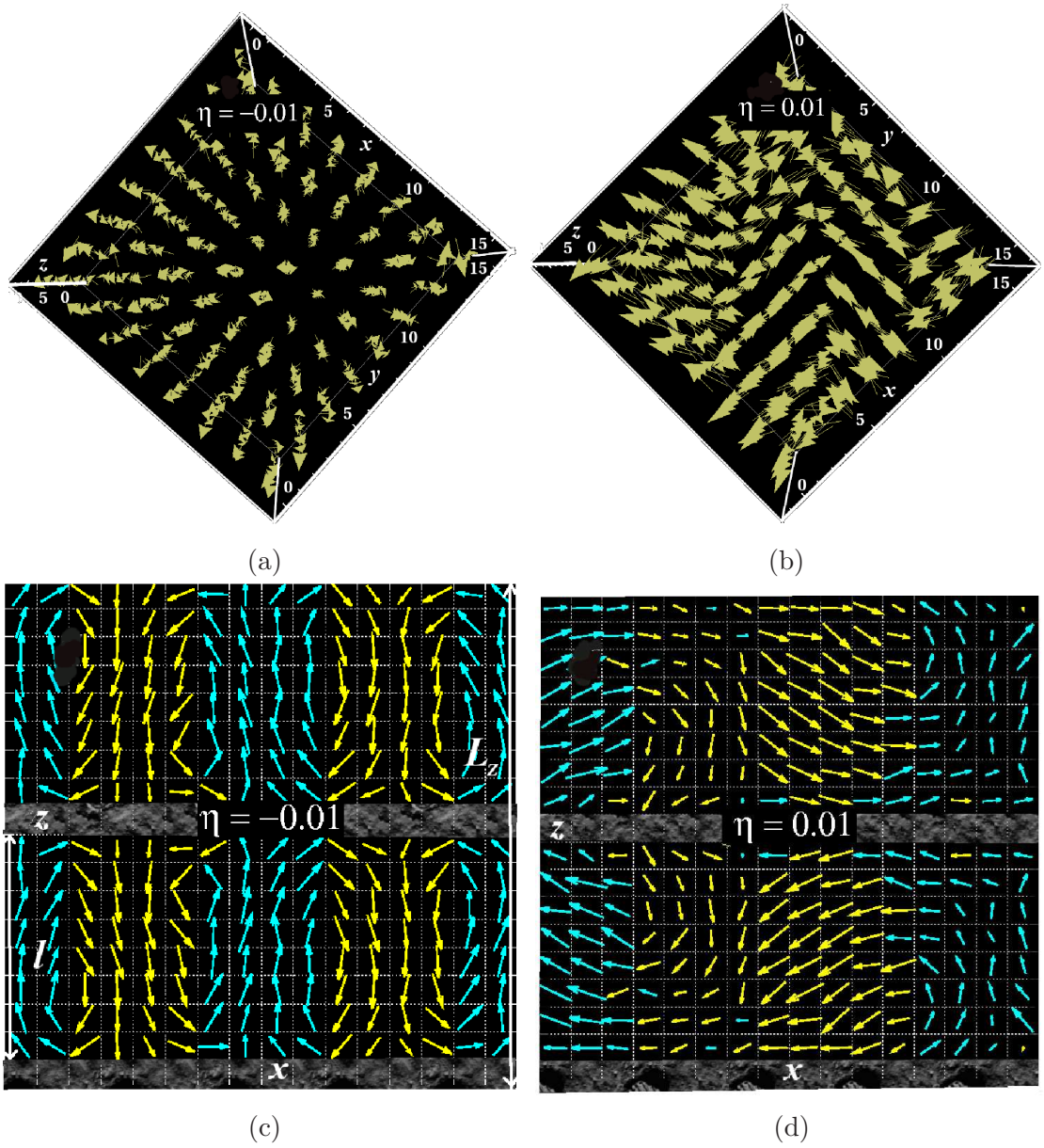

Figure 3.3: Snapshots of 3D ordering of polarization show a transition from a homogeneously ordered phase (a) at compressive strain ($\eta = -0.01$) to 90° domains (b) at tensile epitaxial strain ($\eta = 0.01$) for a film sandwiched between perfect electrodes with $l = 8$ at 145 K (heating simulations). Snapshots of polarization ordering along a cross section show a transition from FCSD phase (c) at compressive epitaxial strain ($\eta = -0.01$) to RWD phase (d) at tensile epitaxial strain for a film sandwiched between imperfect electrodes with l=8 at 55 K (cooling simulations). Copyright (2013) by the American Physical Society.

which a phase with 90° in-plane domain structure gets stabilized (Region III, IV), is much the same in the two phase diagrams. Similar to that in the T-η phase diagram of $BaTiO_3$ [68], this ordering temperature increases with tensile strain. However, the ordering in this phase of $BaTiO_3$ is uniform and involves local dipoles and total polarization along [110] direction. In contrast, the *local* in-plane polarization in this phase of $PbTiO_3$ is along [100] or [010] directions and domain walls separating them, and an overall *"domain"* polarization P_D [Figure 3.4b] that is along [110] direction. The T_C line that marks ordering of polarization along z direction has a negative

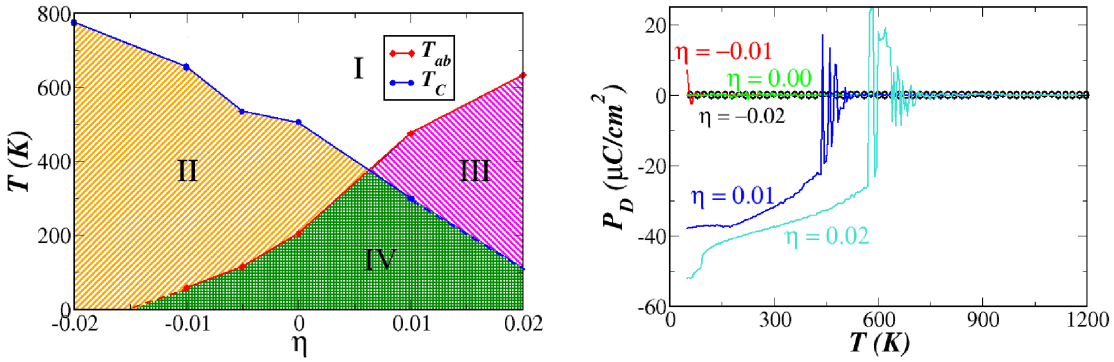

(a) (b)

Figure 3.4: Temperature-epitaxial strain phase diagram (a) of $PbTiO_3$ film ($l = 8$) sandwiched between imperfect electrodes ($d = 1$) representing regions with different stable phases (extrapolations are indicated by the dotted lines). Region I represents PE, II represents flux-closure stripe domain phase, III represents in-plane 90° domain phase and IV represents (i) flux-closure stripe domain phase (Figure 3.3c) and in-plane 90° domain phase for $\eta < 0.0063$, (ii) rectangular wave like 90° domain phase (Figure 3.3d) and in-plane 90° domains for $\eta > 0.0063$. Polarization (b) at different epitaxial strains (cooling simulations). Copyright (2013) by the American Physical Society.

slope (T_C decreases as η changes from compressive to tensile strain) in both the phase diagrams, similar to that in the phase diagram of $BaTiO_3$ [68]. However, we report here two important differences: (a) T_C drops by almost 350 K as the electrode changes from being perfectly screening ($d = 0$) to an imperfect ($d = 1$) one, and (b) the ordering in the latter involves the flux-closure stripe domain phase in contrast to

a simple stripe domain phase in $BaTiO_3$ phase with imperfect electrodes [68]. The strain engineering of the domain structure in $PbTiO_3$ is indeed quite spectacular, and we now focus on that.

In the films sandwiched between imperfect electrodes, with $-0.02 < \eta < -0.014$. We find that, there is a single phase transition from the PE to a flux closure stripe domain (FCSD) phase consisting of elliptic domains (region II) observed recently [61]. For $-0.014 < \eta < 0.0063$, there are two phase transitions: one from the PE (region I) to the FCSD phase [Figure 3.3c] (region II), and another at a lower temperature to the one with in-plane 90° domain phase (while maintaining the FCSD structure) marked as region IV [Figure 3.4a]. Thus the anomaly in the dielectric response of ε_{xx} and ε_{yy} at lower temperatures and compressive strains ($\eta = -0.005$, Figure 3.2b) is associated with the transition from one type of a domain structure (FSCD) to another. For $0.0063 < \eta < 0.02$, the film undergoes a transition from the PE to an in-plane 90° domain phase (Region III) at a higher temperature, and to a rectangular wave-like 90° domain (RWD) phase [Figure 3.3d] (maintaining the in-plane 90° domain structure) (region IV in Figure 3.4a). There is a gradual polar rotation of the local dipole rather than sharp 90° domains at higher temperatures (> 150 K), very similar to the experimentally observed polar rotations of out-of-plane 90° domains at high tensile epitaxial strains $\eta = 0.03$ [10]. For all η, $P_x = P_y$ (P_D) and $P_z \simeq 0$ in films interfacing with imperfect electrodes, where P_D increases as epitaxial strain is varied from compressive to tensile strains [Figure 3.4b].

As the ordering of P_z is uniform in the films sandwiched between perfect electrodes ($d = 0$, Figure 3.5b), the domain structure in these films is largely controlled by the stability of in-plane 90° domains and their interaction with P_z. For $-0.02 < \eta < 0.0076$, these films exhibit two phase transitions, one from PE (region I) to FE phase with P_z (region II) at T_C, and another to an in-plane 90° domain phase (region IV for $\eta < 0.0076$) at much lower temperatures. For $0.0076 < \eta < 0.02$, a

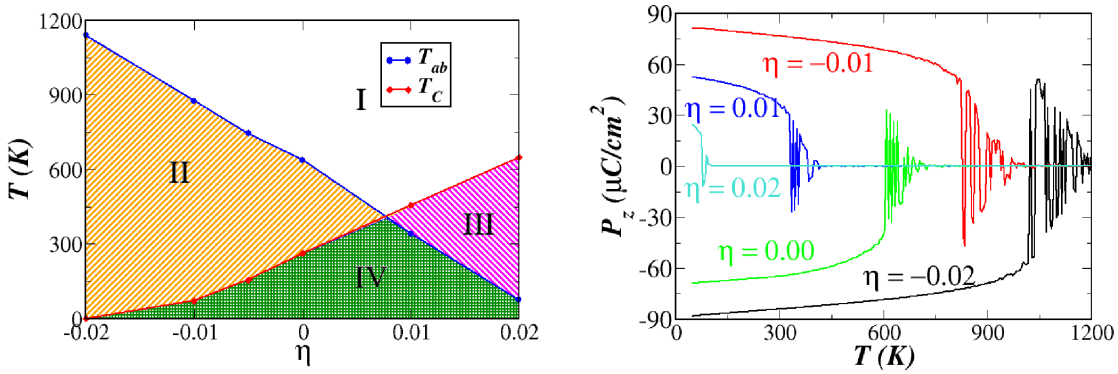

(a) (b)

Figure 3.5: Temperature-epitaxial strain phase diagram (a) of $PbTiO_3$ film ($l = 8$) sandwiched between perfect electrodes ($d = 0$) representing regions with different stable phases. Region I represents PE, II represents tetragonal phase, III represents in-plane 90° domain phase and IV represents FE and in-plane 90° domain phase. Polarization (b) at different epitaxial strains (cooling simulations). Copyright (2013) by the American Physical Society.

film undergoes a transition from PE to in-plane 90° domain structure at a higher temperature (region III), and then to an out-of-plane 90° (ac/bc) domain phase [Figure 3.3b] with in-plane 90° domains [Figure 3.5a].

3.3.3 Microscopic mechanism of domain stability

We now turn to identifying the microscopic mechanisms that are responsible for the stability of domain structure. Strain-phonon coupling was shown to play an important role in the ferroelectric phase transition [55, 90] and the relevant domain structure in bulk $PbTiO_3$, and in the stability of low-symmetry homogeneously ordered ferroelectric phases [67] in general. To determine and understand the impact of the strain-phonon coupling on the domain structures in ultra-thin ($l = 8$) films of $PbTiO_3$ with imperfect electrodes, we carried out simulations by switching off the strain-phonon coupling, *i.e.* setting the parameters $B_{1xx} = B_{1yy} = B_{4yz} = 0$ (refer Ref. [91] for notation). We find that the transition temperature reduces by a factor

of two to 300 K, and this is accompanied by a complete elimination of the domain structure in the $ab-$plane; and stabilization of a phase with uniform polarization along (110) direction across the film, like an orthorhombic phase [Figure 3.6a, 3.6b]. Next, we analyzed the relevance of shear strain-phonon coupling parameter, by switching off B_{4yz} alone. We find that this results in an increase in the average domain size, while the transition sequence and nature of domain structure and phases are unchanged. The former can be rationalized in terms of an increase in the energy cost associated with shear strain localizing at the 90° domain wall. Clearly, strain-phonon coupling is an important microscopic ingredient that strongly influences the domain structures in ultra-thin films of $PbTiO_3$.

3.3.4 Effect of external electric field

We finally study the response of the ferroelectric domains in ultra-thin films of $PbTiO_3$ to electric field, as we expect the strain induced by electric field through piezo-electric coupling to affect the domain stability and dynamics. Electric field controlled directional motion, velocities of domain walls, poling in magnetic and ferroelectric materials have been of investigated experimentally earlier [92,93]. Here, we carried out simulations with an electric field of 0.01 V/Å applied along negative z-direction of a film of $l = 8$ unit cell thickness sandwiched between imperfect electrodes. We find that the presence of electric field of this magnitude does not change the sequence of phase transitions, but has a strong impact on the domain size and walls. The number of domain walls decreases leading to an increase in the average domain size, *i.e.* poling [Figure 3.6c]. P_z is non-zero (~ 8 μC/cm^2) as the dipoles are induced by the applied an electric field, value of the induced P_z confirms a large dielectric constant associated with domain structure and magnitude of P_x, P_y is comparable to that of zero electric field.

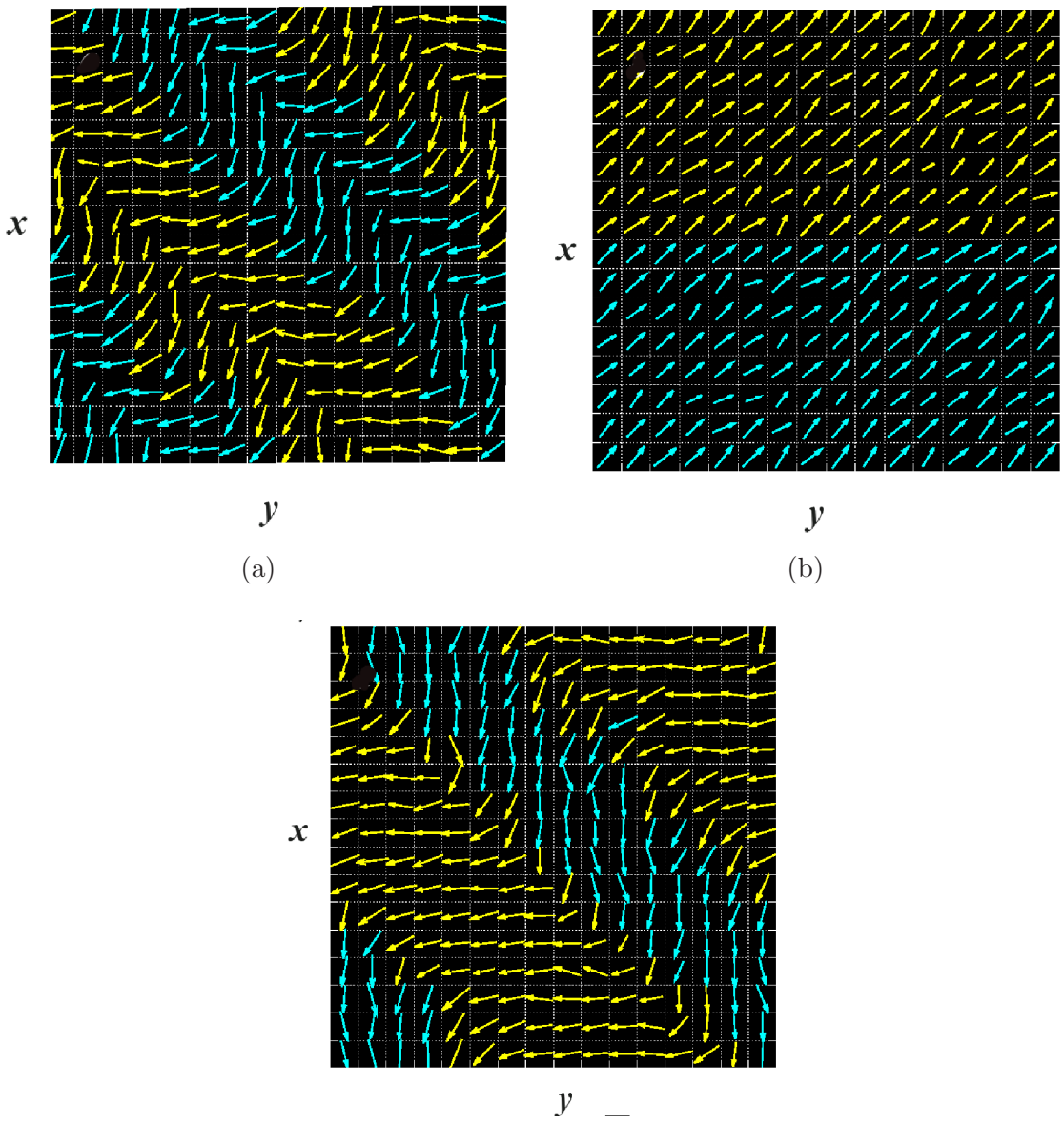

Figure 3.6: Effects of the strain-phonon coupling seen in the snapshots of in-plane polarization ordering of $PbTiO_3$ film ($l = 8$) sandwiched between imperfect electrodes (d=1) under $\eta = 0.01$ (a) with strain-phonon coupling, $E = 0$ V/Å, (b) with strain-phonon coupling turned off, $E = 0$ V/Å and (c) with strain-phonon coupling and finite electric field ($E_z = -0.01$ V/Å) shows poling. Copyright (2013) by the American Physical Society.

3.4 Conclusions

We presented a thorough analysis of ferroelectricity in epitaxially strained ultra-thin films of $PbTiO_3$ using first-principles model based MD simulations. We have shown that the ferroelectric ordering in these films is often inhomogeneous, characterized by the closure flux domain structure and rotating local dipolar rectangular wave-like structure, seen in recent experiments [8, 10, 61–63]. More importantly, such structure is shown to be sensitive to and hence tunable with film thickness, epitaxial strain, electric field and the nature of electrodes, and the origin of this lies in the microscopic strain-phonon coupling. We demonstrated a diffuse phase transition to the flux-closure domain structure as reflected in a rather broad peak in temperature dependent dielectric response. Our work opens up a way of developing diffuse or relaxor ferroelectrics in ultra-thin films with suitable choice of substrate or electrodes and epitaxial strain, and the mechanism of the strain engineering of nano-scale domain structure uncovered here will be useful in the design of ultra-high density memory devices.

Chapter 4

Origin of giant dielectric response of 180° ferroelectric domain structure of $PbTiO_3$ and comparison with $BaTiO_3$

4.1 Introduction

Ferroelectric ordering at nanoscale is often inhomogeneous due to electrostatic and mechanical boundary conditions, which can give rise to new functionalities [8, 64, 94–97]. Engineering of such ordering or ferroelectric domain structure at nano-scale has been achieved by applying strain, electric field, etc, with a goal to enhance their functional properties or to create new functional properties [58, 96–98]. The interface between ferroelectric domains of different spontaneous polarization is called a domain wall (DW), and it is now possible to image the atomic-scale structure of a domain wall [59, 60]. Interestingly, the properties of ferroic domain walls may differ from those of the bulk domains themselves, leading to a variety of interesting

properties from conductive, optical and magnetic making them an active element in nanotechnological applications [96, 99–103]. This is particularly attractive because the domain walls can be created, annihilated, rewritten and displaced electrically inside the material.

Elucidating the DW behavior experimentally is quite challenging, and the origin of many of the newly discovered effects remains unclear. In fact, we still lack a detailed picture of dynamical properties of the DWs, and it is desirable to use predictive theoretical tools in tackling the DWs at the atomistic level. We employ first-principles density functional theory based calculations to investigate the simplest DWs occurring in many perovskite ferroelectrics, namely, 180° boundaries separating regions of opposed polarization. These are several first-principles studies of 180° DWs of $PbTiO_3$ (PTO) and $BaTiO_3$ (BTO) reported in the literature, which have some ambiguity in the polar order within the DW plane [104–108]. Recently Wojdel *et al* [108]. looked at 180° domain structures in $PbTiO_3$, and showed the presence of large non-zero polarization at DW with huge dielectric response using first-principles model potential. Our findings confirm a non-zero polarization in the DW though of relatively lower magnitude in case of PTO, which we discuss in detail later through a comparative analysis with BTO, and understand the microscopic origin of huge dielectric response of the 180° domains structure of PTO.

In this chapter, we first determine the stable structure of multi-domain configuration of PTO and BTO by using first-principles calculations. We present a detailed structural analysis of 180° domain structure, and discuss the polarization profiles as a function of distance from the domain wall in both PTO and BTO. We present a comparative analysis of dielectric behavior for 180° domains of PTO and BTO, and contrast it with that of their bulk structure, and explain the microscopic mechanisms of the observed giant dielectric response of PTO in terms of its 180° domain structure.

4.2 Computational Details

Our calculations are based on first-principles density functional theory (DFT) as implemented in QUANTUM ESPRESSO package [45], with interaction between ionic cores and valence electrons represented using ultrasoft pseudopotentials [47]. We have used a local density approximation (LDA) of Perdew-Zunger parameterized form (for PTO) and generalized gradient approximation (GGA) of Perdew Burke-Ernzerhof (for BTO) for exchange-correlation energy functional [42, 44]. We employ plane wave basis truncated with energy cutoffs of 30 Ry and 180 Ry in representation of wave functions and charge density respectively. We use differet size of supercells *i.e.,* N x 1 x 1 (N = 8 to 20) to simulate domain structures and a uniform mesh of 1 x 8 x 6 k-points in sampling integrations over Brillouin zone. We relax the structure to minimize energy until the Hellman-Feyman forces are less than 0.03 eV/Å in magnitude. Phonons and Born effective charges are obtained from the second derivatives of energy calculated using density functional perturbation theory (DFPT).

4.3 Results and Discussion

4.3.1 Structure and polarization

We first investigate the structure and energetics of 180° domain structure in PTO and BTO. We have used a N x 1 x 1 supercell of tetragonal PTO and BTO, with the initial polarization in $+z$-direction in first half of the supercell and $-z$-direction in the other half supercell modelling the 180° domains [Figure 4.1a], keeping the lattice parameters fixed to experimental value [see Table 4.1]. To quantify the atomic displacements contributing to a ferroelectric distortion, we determined the polarization (P^i_α) per unit cell i, along the Cartesian direction α by using the technique given by

Table 4.1: Experimental lattice parameters of PTO and BTO used in our calculations.

System	a (Å)	$\frac{c}{a}$
PTO	3.845	1.063
BTO	3.992	1.011

Meyer and Vanderbilt, [104]

$$P_{\alpha}^{i} = \frac{e}{V} \sum_{x} w_x Z_x^{*}.u_x^{i} \tag{4.1}$$

where e is the charge of electron, V is the volume of a unit cell, x represent all atoms belonging to the unit cell, w_x is the fractional weight factor of the corresponding atom and u is its atomic displacement. In case of 180° domains of PTO (PTO−D), we find a very high onset polarization along z-direction (P_z) *i.e.,* 0.85 C/m^2, and a sizeable nonzero polarization in the y-direction (P_y = 0.24 C/m^2) in the planes near the domain wall, which vanishes as one moves into the centre of the domain [Figure 4.1b for 8 x 1 x 1 supercell]. Antiparallel P_y at the consecutive domains walls is switchable with energy cost of about ∼0.04 meV/f.u., indicating that both the configurations are equally favorable. Our findings are similar to those of Wojdel *et al.* except that they have found relatively higher value (0.75 C/m^2) of P_y, this is possibly because the initial structure used in first-principles calculations was relaxed using a first-principles model potential [108]. On other hand, BTO-D has a relatively low onset polarization in z-direction, P_z (∼0.27 C/m^2) with an equal magnitude of P_x and P_y throughout the inhomogeneous domain structure [see Figure 4.1c for 8 x 1 x 1 supercell], consistent with the fact that the rhombohedral phase is the stable bulk structure at 0 K.

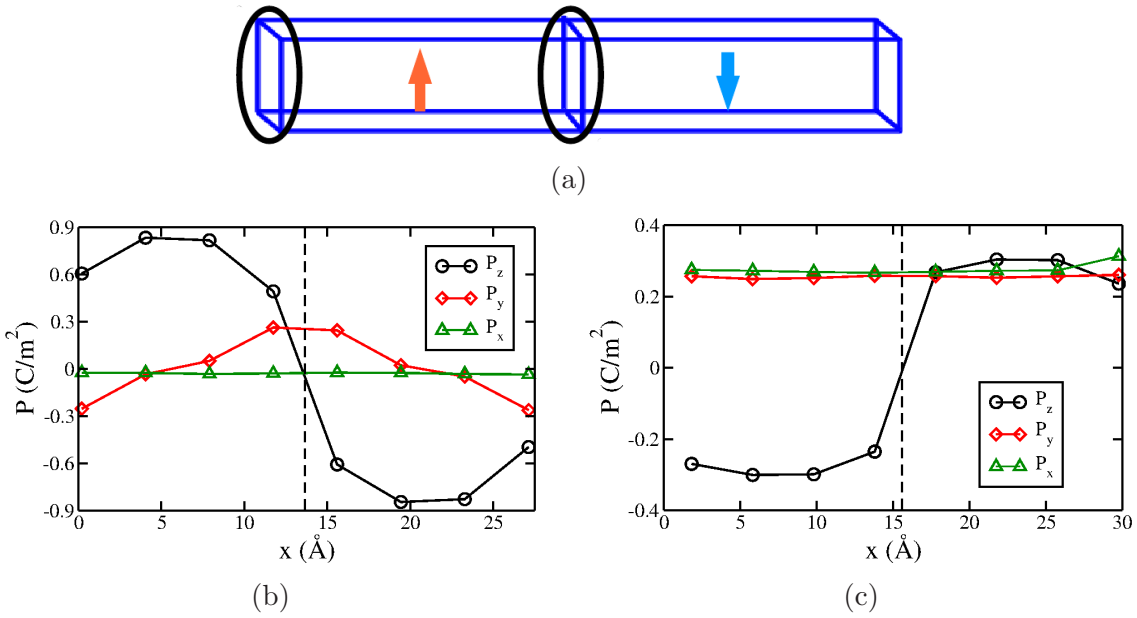

Figure 4.1: Schematic of 180° domain structure (a), polarization profiles for 180° domain structures of PTO (b) and BTO (c). The latter is consistent with the rhomobohedral structure of BTO with P along (111) direction.

4.3.2 Effect on electronic properties

We now determine the effects of domain walls on electronic structure of PTO and BTO. We compare calculated density of electronic states of bulk and 180° domain structures of PTO and BTO [see Fig. 4.2]. The presence of domain wall in PTO leads to a negligible change in the band gap, on the other hand the band gap increases significantly ($\Delta E_g = \sim 0.57$ eV) for BTO-D. To understand such a large change in the band gap for BTO-D, we analyzed the projected density of states and find that $3d$-orbitals of Ti which lie at the top of valence band shift lower in energy, leading to a widening of the band gap.

The Born effective charges (BEC), Z^*, reflect the degree of hybridization in the

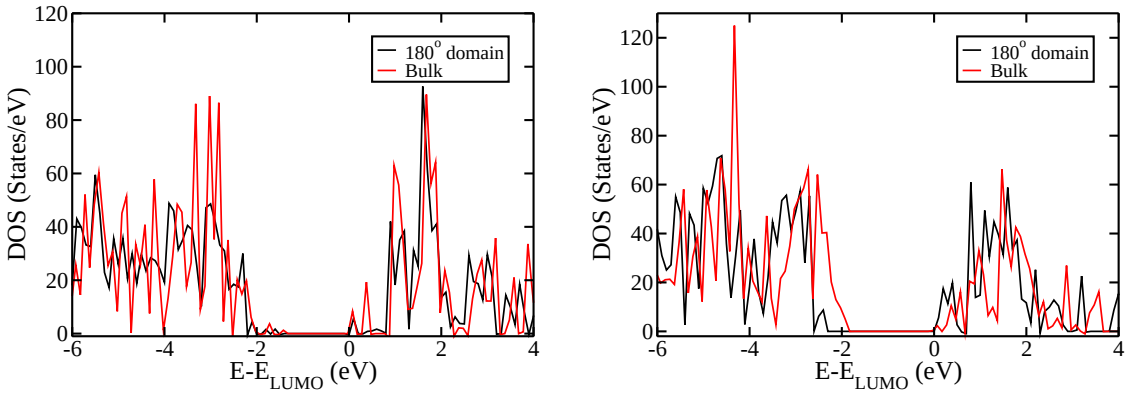

Figure 4.2: Comparison of electronic density of states of 180° domain structure with bulk structure of PTO (a) and BTO (b).

system and is calculated as a first derivative of polarization w.r.t atomic displacement (u),

$$Z^*_{i\alpha\beta} = V\frac{\partial P_\alpha}{\partial u_{i\beta}} \tag{4.2}$$

where i labels the atomic site, α and β indicates Cartesian direction and V is the volume of the unit cell. Comparison of BEC's of atoms in the 180° domain structure with the bulk counter parts show slight reduction in BEC of A cation and O with nearly same amount of increase in Ti atom near the domain wall (ΔZ^*=$\sim$ 0.1 - 0.2) for both PTO and BTO with significant non-zero off diagonal elements for atoms near the domain wall ($\sim$0.1-0.3) indicating lower symmetry and covalent nature of TiO_6 octahedra [Table 4.2].

4.3.3 Dielectric response and vibrational analysis

We now move to dielectric constant , the electronic contribution of dielectric constant ($\kappa^{\alpha\beta}_\infty$) is calculated as second derivative of total energy (E_{tot}) wrt electric field (E):

$$\kappa^{\alpha\beta}_\infty = \frac{4\pi}{\Omega}\frac{d^2E_{tot}}{dE_\alpha dE_\beta} \tag{4.3}$$

Table 4.2: Comparison of Born effective charges of ions near domain wall (nDW) with one in the center of domain (fDW).

System	Ion	nDW			fDW		
		Z^*_{xx}	Z^*_{yy}	Z^*_{zz}	Z^*_{xx}	Z^*_{yy}	Z^*_{zz}
PTO-D	Pb	3.71	3.77	3.81	3.86	3.77	3.53
	Ti	6.53	6.49	5.37	6.42	6.30	5.44
	O_1	-2.44	-5.42	-2.24	-2.67	-5.22	-2.21
	O_2	-2.41	-2.38	-4.89	-2.66	-2.22	-4.97
BTO-D	Ba	2.82	2.56	2.56	2.81	2.56	2.57
	Ti	6.02	6.00	5.75	6.04	6.01	5.76
	O_1	-1.95	-4.91	-1.92	-1.94	-4.92	-1.94
	O_2	-1.98	-1.97	-4.88	-1.98	-1.98	-4.90

where Ω is the volume of supercell. From $\kappa_\infty^{\alpha\beta}$ (different components of dielectric constant) of both bulk and domain structure of PTO or BTO [Figure 4.2a], we find that presence of DW in PTO or BTO has a negligible effect on electronic contribution of dielectric constant as expected from changes in their electronic gap. To estimate

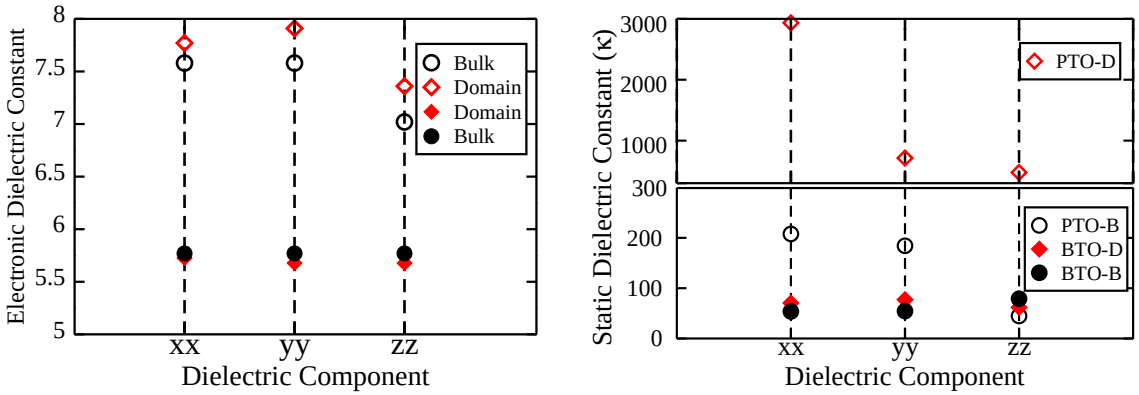

Figure 4.3: Electronic (a) and static (b) dielectric constant of bulk and domain structures of PTO and BTO.

the static dielectric constant, we determine vibrational spectrum at zone center. The vibrational density of states at zone center (Γ) shows that $\omega > 0$, for all the normal modes indicating that the 180° domain structure is locally stable in both

PTO and BTO at T = 0 K [Figure 4.3a].

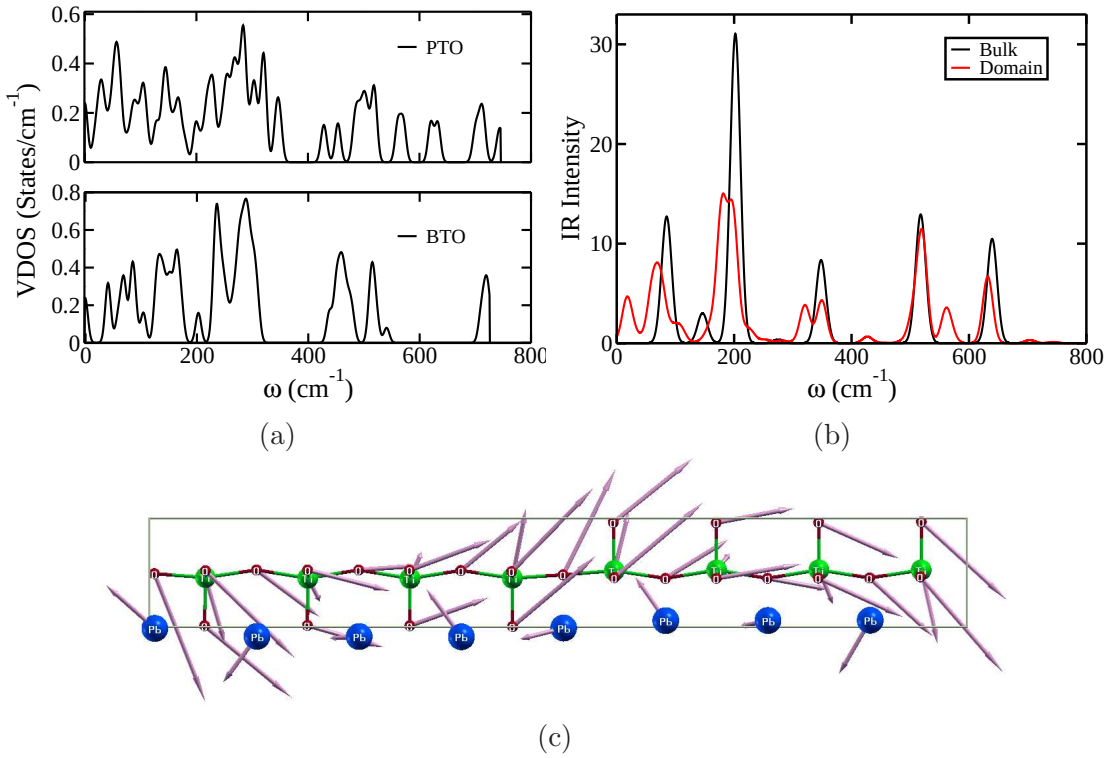

Figure 4.4: Vibrational density of states of 180° domain structures of PTO and BTO (a), IR spectra (b) and IR active soft mode with $\omega = 17$ cm^{-1} (c) of PTO-D.

The static dielectric constant (κ), which is a sum of electronic and phononic contribution's and is calculated using

$$\kappa_{\alpha\beta} = \kappa_{\infty}^{\alpha\beta} + \sum_{\omega_{\mu}^2=0} \frac{Z^*_{\mu\alpha} Z^*_{\mu\beta}}{V \epsilon_0 m_0 \omega_{\mu}^2} \tag{4.4}$$

where μ labels zone-center (q = 0) normal modes, ω_{μ} being their (angular) frequencies. In case of BTO, we find that the static dielectric constant of the domain structure is comparable to that of its bulk [Figure 4.3b]. In contrast, the static dielectric constant of PTO-D, along the direction perpendicular to the plane of the domain wall is anomalously high. Such huge lattice contribution to dielectric constant has to be due to the presence of infrared active soft phonon modes which

predominantly contribute to the static dielectric constant. From the projected out IR active modes of both PTO-D/BTO-D [Figure 4.4b], we indeed find a presence of IR active soft mode in case of 180° domain of PTO with a frequency, $\omega = 17$ cm^{-1}, Its eigen displacements show that it is localized on the DW, where the Pb atoms move in the direction opposite to TiO_6 octahedra. To identify the origin of this soft mode in 180° domain structure of PTO, we project the normal modes of the domain structure onto the bulk PTO, by calculating an overlap or correlation matrix given by

$$S_{\mu v} = \langle e_{\mu}^{B} | e_{v}^{D} \rangle \tag{4.5}$$

where e_{μ}^{B} is the eigen vector of the bulk PTO and e_{v}^{D} is the eigen vector of the PTO domain structure. The soft mode responsible for huge dielectric constant is a linear combination of several modes of long wavelength *i.e.,* near zone center.

4.4 Conclusion

We presented analysis of the effects of 180° domain walls on the dielectric properties of $PbTiO_3$ and $BaTiO_3$ using first-principles density functional theory, and have shown the presence of non-zero transverse polarization (along y-direction) confined to the domain wall in case of 180° domains in PTO. We show that the presence of domain wall separating domains of opposite (180°) polarization of tetragonal perovskites leads to a giant dielectric response of PTO. It is shown to originate from a soft IR active phonon mode localized at the DW. We find that 180° domains of $BaTiO_3$ involve rhombohedral structure at 0 K similar to that of its bulk structure, and hence a dielectric response comparable to its bulk.

Part II

Materials for Environment

Chapter 5

2-D honeycomb lattices of C and ZnO: Applications for clean environment

5.1 Unusal adsorption of pesticides on graphene[†]

5.1.1 Introduction

During the past decades, considerable understanding has been developed on the relationship between water quality and human health. Standards of drinking water have been revised several times, and with increased understanding of the health effects associated with several contaminants, the maximum permissible limits (MPL) of the contaminants are likely to reach molecular limits in due course [109]. Among the 92 regulated contaminant species as per environmental protection agencys (EPA), pesticides are of major concern due to their indiscriminate use and widespread occurrence in drinking water. The toxicity and health hazards posed by pesticides, even

[†]A part of this work is published in *Small*, 2013 [1]. Copyright (2013) by John Wiley & Sons, Inc., URL: http://dx.doi.org/10.1002/smll.201201125.

at very low concentrations, have become large concerns for both developing and developed countries [110, 111]. World health organization (WHO) drinking water standard prescribes a MPL for single pesticide as 0.1 μg L^{-1}. It is in this context that new adsorbents and new chemistry have to be developed to control these species. As a result of tireless search for new technology, which enables efficient separation of pesticides from water, many new materials with interesting properties have been evolved. Nair *et al.* [112] has reported the use of noble metal nanoparticles for the degradation of pesticides in water at ultra low concentrations. Carbon nanotubes (CNTs) are another category of materials investigated recently for pesticide uptake [113]. However, CNTs are reported to be cyto-toxic [114, 115] which may limit their utility in drinking water purification.

Since the discovery of graphene, single atomic layer of carbon in 2004 [116], it has attracted overwhelming attention due to its unique chemical and physical properties and low production cost compared to other graphitic forms [117, 118]. As of now, graphene and graphene-based materials are proposed for many applications. This include drug delivery [119], solid-state gas sensors [120], electrochemical sensors [121, 122], Raman scattering based molecular sensor [123], hydrogen storage [124, 125], energy storage devices [126], and catalysis [127]. Recent studies show that graphene-based materials have good potential in environmental cleanup as well. Large surface area [128], reduced cytotoxicity [129], the large delocalized π-electrons [130] and tunable chemical properties [131] make these materials perfect candidates for adsorption of chemicals and thus cleanup of water. The utility of graphene-based materials for arsenic removal has been proved very recently [132]. The antibacterial properties of graphene oxide (GO) and reduced graphene oxide (RGO) have also been studied and it has been found that both are antibacterial [129]. Gao and coworkers have demonstrated that GO-coated sand could be used as a low-cost water purification material for developing economies [133]. A recent investigation

shows that sulfonated graphene is a good medium for the separation of naphthalene and 1-naphthol from water and the adsorption capacities were estimated to be ∼2.3-2.4 mmol g^{-1} [134]. However, no systematic effort has been done to use RGO and GO to remove complex molecules such as pesticides from water.

Maliyekkal *et al.* [1] has explored the use of graphene oxide (GO) and reduced graphene oxide (RGO) for the removal of pesticides like chlorpyrifos (CP), endosulfan (ES) and malathion (ML) from water. ES belongs to the organochlorine (OC) group, CP and ML belong to the organophosphate group are are extensively used as insecticides in many countries [135] and are widely detected in the surface and groundwaters [136–138]. They found the adsorption capacities of CP, ES and ML to be as high as ∼1200, 1100 and 800 mg g^{-1} respectively [see Figure 5.1a for ES]. The adsorption kinetics has revealed rapid removal of pesticides i.e., more than 90% of the pesticide removal happened in <10 min contact time, and no traces were detected after 30 min contact [see Figure 5.1b for ES]. Moreover, the adsorbent was found to be reusable. In order to delineate the removal mechanism and to comprehend the observed uptake capacity, an analysis using first-principles pseudo-potential based density functional theory (DFT) is carried out. While all the experiments were carried out at room temperature, the first-principles calculations provide energies at 0 K, and we use them to develop a qualitative understanding of observations in the experiments. Although such calculations can be employed in molecular dynamics to simulate behavior at finite temperature, this approach is quite expensive and unrealistic particularly to access the time-scales relevant to separation of pesticides from water. We address the following issues in the observed capacity of graphene to adsorb these pesticides at unprecedented levels: 1. Is adsorption feasible and how is it influenced by water? 2. Is such a large capacity of adsorption possible, and what may be an upper limit on it? 3. What are the atomistic mechanisms responsible?

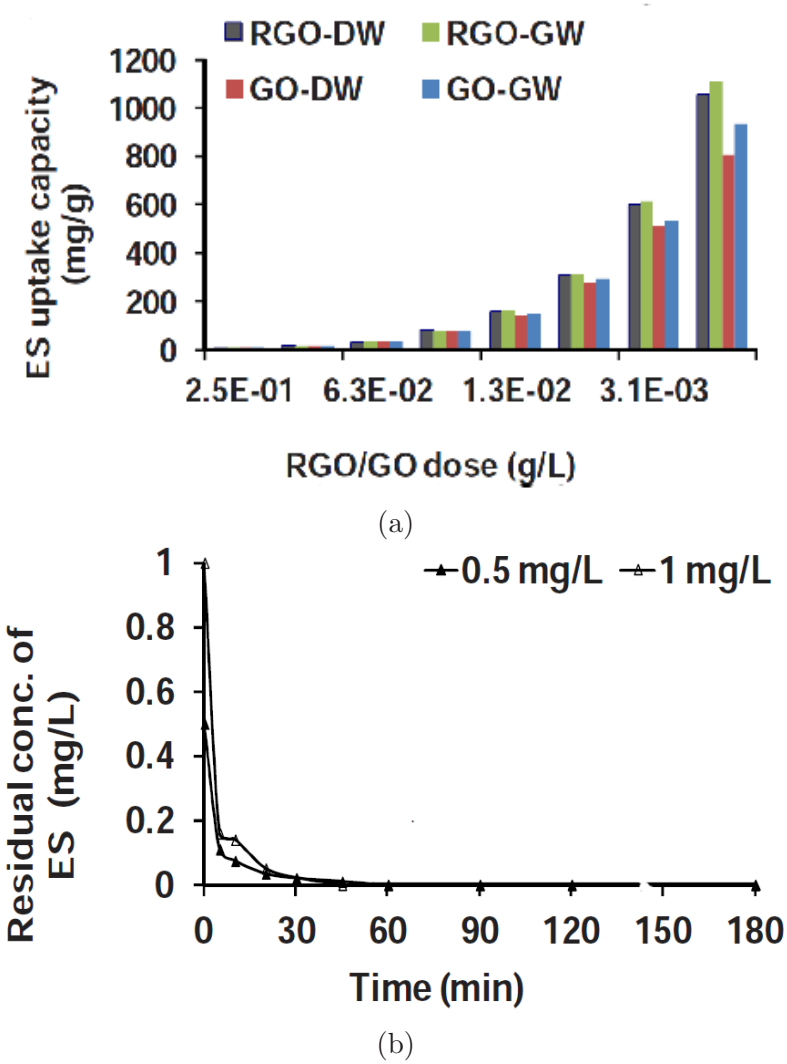

Figure 5.1: Adsorption of ES as a function of a function of RGO and GO dose in drinking water (DW) and ground water (GW) (a) and residual ES after contact with RGO dispersed in GW (b). This work was done by Maliyekkal *et al* [1]. Copyright (2013) by John Wiley & Sons, Inc.

5.1.2 Computational Details

We used PWSCF [45] implementation of DFT, which is based on ultra-soft pseudopotentials [47] to represent an interaction between ionic cores and valence electrons and a plane-wave basis. As the densities in molecular systems change rapidly

in space, we used a generalized gradient approximation (GGA) with Perdew Burke-Ernzerhof (PBE) [44] form of the exchange-correlation energy functional. Kohn-Sham wave functions were represented with a plane wave basis with an energy cutoff of 30 Ry and charge density with a cutoff of 180 Ry. We used periodic boundary conditions with 8 x 8 and 5 x 5 supercells of graphene to simulate different concentrations of pesticides and water molecules interacting with it, and include a vacuum up to 22 Å (minimum thickness of vacuum was 12.8 Å) in the direction perpendicular to graphene plane to keep interactions between periodic images of molecules minimal. Integrations over Brillouin zone (for these periodic supercells) were sampled with 3 x 3 x 1 and 1 x 1 x 1 uniform meshes of k-points, ensuring convergence with respect to k-points while using occupation numbers smeared with Fermi-Dirac scheme with a broadening of 0.003 Ry. We considered many structural configurations for each pesticide (β-ES, CP, and ML) obtained with different orientations and positions of pesticides and water molecules relative to graphene, and relaxed the structure to minimize energy until Hellman-Feynman forces on atoms were less than 0.001 Ry/bohr in magnitude.

Results and Discussion

5.1.3 Structure of pesticides

To facilitate comparative analysis of energetics that involve different species of atoms, we first considered the following systems: a free water molecule (W), pristine graphene (G), a free pesticide molecule (P = ES, CP, or ML), and an aggregate of n water molecules (nW). Energy of each of these was determined through structural relaxation in a large supercell. Our optimized structure of graphene has a lattice constant of 2.45 Å in good agreement with the experimental value of 2.46 Å [139]. Using experimental [140] hexagonal crystal structure of β-ES for the initial guess in

our structural optimization, we find that bond lengths of ES change by only a couple of percent during relaxation, within the typical errors of DFT calculations. Similarly, we used a monoclinic crystal structure of CP available experimentally [139] and find that our relaxed structure is in reasonable agreement with experiment. Detailed structure of ML is not available experimentally, and we determined it from our calculations. Since our pseudopotentials and other calculational parameters seem reliable in accurately describing the structures of ES and CP, we expect a similar level of accuracy in the structures of ML as well (see structures of pesticides in Figure 5.2).

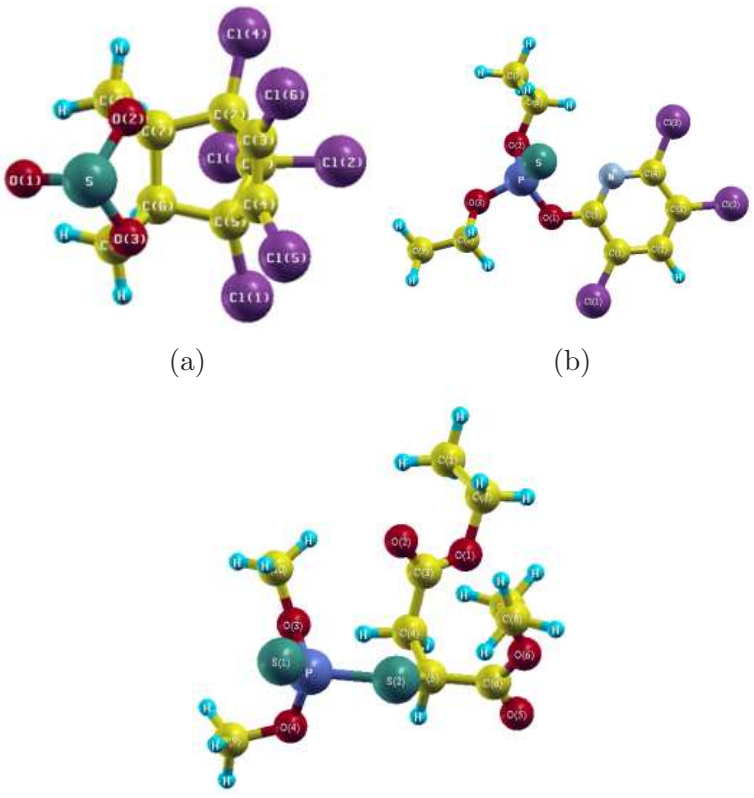

(a) (b)

(c)

Figure 5.2: Structures of pesticides considered under study: endosulfan (a), chlorphyrifos (b) and malathion (c). Copyright (2013) by John Wiley & Sons, Inc.

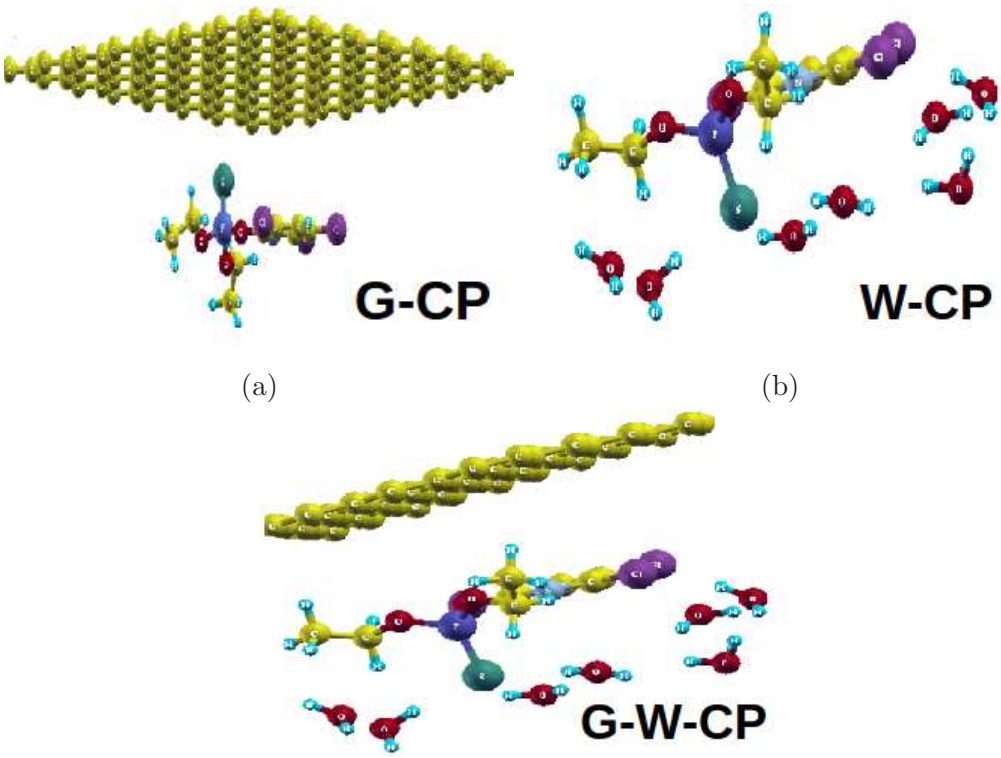

(a) (b)

(c)

Figure 5.3: Relaxed structures of different complexes considered in the present study, binary complexes (a, b), and ternary complex (c) shown for chlorphyrifos. Copyright (2013) by John Wiley & Sons, Inc.

5.1.4 Adsorption of pesticides on graphene

To understand the mechanism of adsorption, we have considered different binary and ternary complexes [Figure 5.3]. Among the binary complexes, we first considered different (three to four) configurations of pesticide-graphene (P-G) complexes with different orientation of each pesticide with respect to the graphene sheet. To quantify the strength of interaction between P and G, we obtain adsorption energy, E_A defined as

$$E_A = E_{P-G} - (E_P - E_G) \tag{5.1}$$

where , E_{P-G} , E_P , E_G are the energies of the optimized structures of pesticide-graphene complex, isolated free pesticide molecule and graphene supercell, respectively. Similarly, we quantify the energy of dissolution by

$$E_D = E_{W-G/P} - (E_W - E_{G/P}) \tag{5.2}$$

where $E_{W-G/P}$ is the energy of water and graphene or water and pesticide complex. Our results clearly reveal that (a) $E_A > 0$ with magnitudes from 30 to 50 kJmol^{-1} for ES and CP, while there is weak binding (-2 to -3 kJmol^{-1}) for ML, and thus adsorption of these pesticides on dry graphene is unlikely or at the best very weak, and (b) $E_D < 0$ meaning both graphene and pesticide have an attractive interaction with water molecules (relative to free water molecules). However, we also found that E_nW - $nE_W < 0$ (intermolecular water interaction), with magnitude comparable and even greater than of E_D in case of ML and CP. Thus, adsorption of pesticides or graphene in water is limited. Experimental samples of graphene used by Maliyekkal *et al.* [1] though, are partially functionalized which can alter the adsorption of graphene.

We turn to our results on ternary complexes G-W-P. To evaluate energetic stability, we examine the adsorption energy of the G-W-P complex as:

$$E_{G-W-P} = E_{complex} - (E_G + E_P + nE_W) \tag{5.3}$$

for n = 6, and compare with E_A and E_D defined earlier[Table 5.1]. First of all, we find that there is an energy gain associated with binding between graphene, pesticide and water molecules relative to any of the pair-complexes: $E_{G-P-W} < E_A$ and $E_{G-P-W} < E_D$, when we consider the lowest energy configuration for each [Table 5.1]. For each pesticide, energy of the G-W-P complex is lower by 20-40 kJmol^{-1} than the energy of a pair complex such as W-P or W-G or nW ($n = 6$). Thus, with

respect to free graphene or free pesticide in water, it is energetically preferable for a G-W-P complex to exist. Secondly, the energy gain associated with the formation of a graphene-pesticide-water complex increases with number of water molecules n, up to a value that gives reasonable packing of water molecules in the space available (about n = 50, depending on the pesticide) in the 5 x 5 supercell [Table 5.2 for a ternary complex with different orientation of ES w.r.t to graphene sheet (GWES*)].

Table 5.1: Comparison of binding energies (kJ/mol^{-1}) of binary and ternary complexes of ES, CP and ML.

Pesticide	System	Binding Energy
ES	P-G	34
	W-P	-203
	G-W-P	-217
CP	P-G	-32
	W-P	-95
	G-W-P	-181
ML	P-G	-3
	W-P	-97
	G-W-P	-163

Table 5.2: Variation in adsorption energy (kJmol^{-1}) as a function of number of water molecules for graphene-endosulfan-water complex.

System	n	Adsorption Energy
GWES*	3	-61.95
	6	-169.14
	12	-471.45

Visualization of the structure and charge density reveal polarity and suggests the electrostatic interaction [Figure 5.4a]. Naturally, water, with its polar structure, plays an important role in mediating effective interactions between graphene and a pesticide revealed from the energetics for different stacking of ternary complexes [Table 5.3, where G-W-ES represents water sandwiched between graphene sheet

and endosulfan, W-G-ES represents graphene sandwiched between water molecules and endosulfan and G-ES-W represents endosulfan sandwiched between graphene and water molecules]. We find that only a few bonds, particularly the polar ones, in a pesticide molecule, which are close to water molecules and graphene, change noticeably when it enters into an interaction with graphene and water. For example, while one of the P-S bonds in ML elongates and the other shortens by 1%, both P-O bonds contract by less than a percent. While a P-S bond in CP elongates by a percent, its P-O bonds are shortened by less than a percent. In ES, one of the S-O bonds becomes longer by a percent and the other contracts by half a percent. As the distance between any of the molecules and graphene is always greater than a typical bonding distance, we conclude that the origin of these structural changes and associated energetics is mainly electrostatic in nature. However, the nature of interaction between dry graphene and ES is slightly different in nature, and involves some bending (by 3.2°) of graphene sheet [Figure 5.4b] and costs energy of the order 30-50 kJmol^{-1}. In this case, the S=O (double bond) bonds elongate by 1.7% and both single S-O bonds elongate by 3.5% relative to the relaxed ES molecule. On the other hand, one of the C-Cl bonds closer to graphene sheet shortens by 1%, and the other elongates by 3.5%.

Table 5.3: Adsorption energies (kJ/mol^{-1}) of ternary complexes of endosulfan, water and graphene.

System	Configuration (n = 6)	Adsorption Energy
Ternary	G-W-ES	-217.94
	ES-G-W	-20.91
	G-ES-W	-184.45

Our calculations with n x n supercell of graphene correspond to pesticide adsorption capacities ranging from 600 to 2000 mg g^{-1}. Our results for G-W-ES [Figure 5.5, Table 5.4] clearly show that there is an overall binding between ES, graphene and water molecules for coverages lower than 1600 mg g^{-1}. Indeed, this confirms

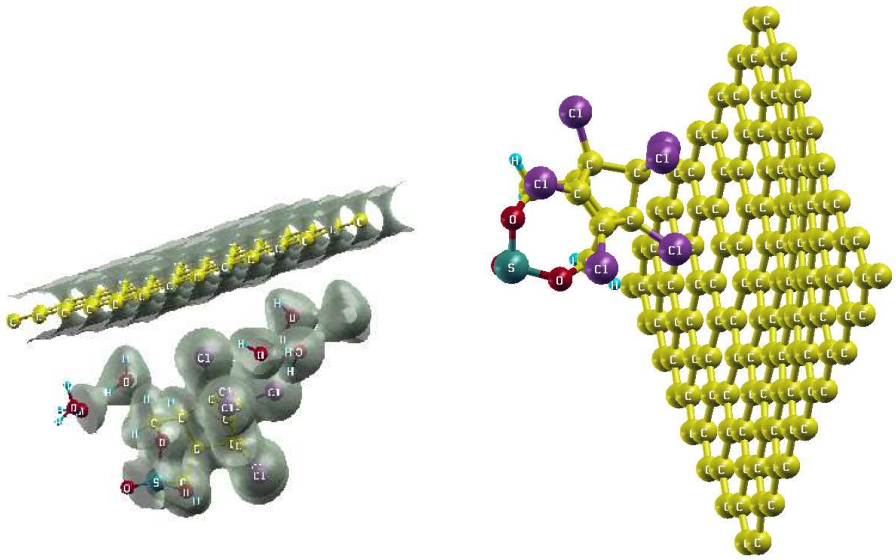

(a) (b)

Figure 5.4: Visualization of charge density for relaxed structure of G-W-ES complex (a) and bending in ES-G complex (b). Copyright (2013) by John Wiley & Sons, Inc.

the experimental observation that a pesticide can precipitate along with graphene and water at these high coverages/capacities. Our theoretical estimate of the upper limit on pesticide adsorption capacity is slightly higher than the experimental value because it corresponds to the most stable configuration (T = 0 K) among the ones considered here, and DFT calculations are known to typically overestimate the binding energies.

Table 5.4: Variation in energies of adsorption (kJmol^{-1}of G-W-ES complex as function of concentration of endosulfan (mg g^{-1} of C).

System	Amount of endosulfan	Adsorption Energy
G-W-ES	1878.9	258
	1409.24	-160
	1056.00	-195
	696.93	-218

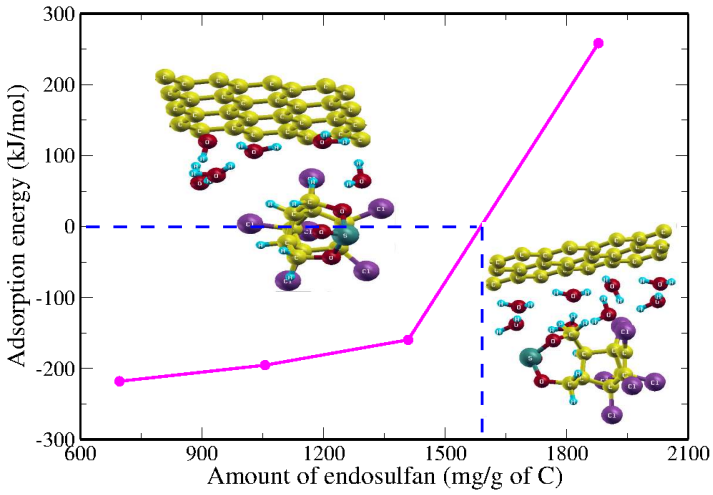

Figure 5.5: Energy of adsorption of endosulfan on graphene in the presence of water molecules as a function of coverage (expressed in the amount of ES per gram of graphene). The structures on the left correspond to 4 x 4 supercell and good binding in the complex, while the one on the right is for 3 x 3 supercell of graphene with no binding. Copyright (2013) by John Wiley & Sons, Inc.

5.1.5 Conclusions

Using first-principles DFT-based analysis, we have determined the energies of adsorptive interaction between graphene and a pesticide (binary complex) as well as graphene, pesticide and water complexes, revealing that the pesticide adsorption on graphene is thermodynamically feasible only in the presence of water molecules, and adsorption of any of the three pesticides on dry graphene is expected to be rather weak or unlikely. Hence, the observed removal of pesticides from water by graphene is proposed to be due to the formation and precipitation of G-W-P complexes through water-mediated, electrostatic interactions. The present study reveals the richness in interaction of graphene with molecular systems and opens a way for further research in this important field of environment friendly applications of graphene.

5.2 Adsorption of toxic H_2S on 2D-$ZnO_{1-x}N_y$[†]

5.2.1 Introduction

Hydrogen sulphide is a toxic and corrosive gas; exposure to H_2S causes broad range of health problems at low concentrations and can be lethal when inhaled in large concentrations [141]. H_2S is released in significant quantities in many industrial processes which include natural gas processing, petroleum refining, mining, and paper and pulp processing. Many methods have been implemented for the removal of H_2S in environment such as biological fixation, iron chloride dosing, water scrubbing etc [142]. These methods are either expensive or demanding in terms of their footprint.

Dissociation of H_2S leading to non-toxic by-products is one of the possible solutions [143,144]. The Claus process is widely used for dissociation of H_2S in industries, but the main drawback is that the by-product is water (H_2O) instead of clean fuel (H_2) [142]. Thermal decomposition of H_2S into H_2 and S has been investigated and is thermodynamically unfavorable [145]. Here, we explore the possibility of using a nano-material to facilitate splitting H_2S into H_2 and atomic S through chemical interaction, with two-fold goals: (i) elimination of toxic gas from environment, and (ii) production of clean energy fuel (H_2) with a much lower heat of formation (-4.77 kcal mol^{-1}) than H_2O (-68.32 kcal mol^{-1}). Needless to say, another application of the same material would be in the gas sensing.

Semiconducting metal oxides (SMO) nanoparticles have been natural candidates for gas sensing applications due to (i) large surface-to-volume ratio, (ii) high sensitivity to gaseous exposure through a change in their conductivities due to surface electron accumulation [17, 18], and (iii) a low fabrication cost. Gas sensing is

[†]This work has been published in *Phys. Chem. Chem. Phys.*, 2014 [12]. Reproduced by permission of the Royal Society of Chemistry, URL: http://dx.doi.org/10.1039/C4CP01092B.

essential for industrial process control, safety systems and environmental monitoring [146, 147]. Many semiconducting metal oxides are known for their use as gas sensors. For instance, Comini *et al.* [19] have used SnO_2 nanobelts for the effective detection of pollutants like CO and NO_2 and C_2H_5OH in breath analyzers and food control applications. Chao *et al.* [148] have used In_2O_3 nanowires for detection of small amounts of NO_2 and NH_3, and showed (a) a significant change in conductance (as high as 10^5 to 10^6 times), and (b) very short recovery time of the device by illuminating with UV light. Other metal oxides such as TiO_2, ZnO and Fe_2O_3 are also known for applications as gas sensors [148–150].

Change in conductivity resulting from the interaction with a gas necessarily involves modification of the electronic structure and bonding. Hence, SMO (eg. TiO_2, Fe_2O_3) have also been known for hydrogen fuel production by dissociation of H_2O [151,152]. Since O and S belong to the same group, we expect SMO to possibly facilitate the process of dissociation of H_2S. Rate of reaction of H_2S with different metal oxides surfaces such as Cr_2O_3, Al_2O_3 and ZnO have been studied and known to be inversely proportional to band gap of the metal oxide [144, 153]. To this end, N-substitution in ZnO is known to reduce its gap, and can be effective in enhancing its interaction with H_2S. [154]

In the bulk form, ZnO is a wide band-gap semiconductor (3.37 eV) with high exciton binding energy (60 meV) and a large piezoelectric constant [155–158]. The band gap of ZnO can be engineered by alloying with MgO and CdO, which is useful for optoelectronic devices [159–161]. Its unique set of properties makes it useful in many applications such as transparent electronics, spintronics, piezoelectric devices, optical devices and chemical sensors. Central to these is its ability to exist in diverse forms of nanostructures, which makes it a key technological material. Theoretical prediction of 2D-ZnO (inorganic analogue of graphene) with large surface area and a wide band gap ($E^{GW} = 3.57eV$) [162] makes it an interesting candidate for gas

adsorption/dissociation.

In addition to temperature, size and dimensionality, the presence of native defects and doping with impurities or promoters also influence the rate of adsorption and dissociation. Ahn *et al.* [163] have shown that gas sensing behavior is linearly proportional to the photoluminescence intensity of oxygen vacancies. Zhang and coworkers, [30] have reported that doping graphene with transition metal atoms like Ca, Co, Fe or Si lead to chemisorption of H_2S as compared to its weaker physisorption on pristine graphene. Lee and coworkers, [164] have shown 100% recovery and drastic improvement to the sensing ability of SnO_2 in detecting very low concentrations of H_2S (< 1 ppm) using MoO_3 and NiO as promoters. Bikondoa *et al.* [152] have shown defect (O-vacancies) mediated splitting of H_2O in thin-film of TiO_2. However, Hegde *et al.* [165] have studied adsorption of H_2S on pristine graphene and graphene with defects, and showed that H_2S interacts weakly through vdW interaction with both pristine graphene and graphene with defects [165].

In this chapter, we have studied the adsorption and possible modes of dissociation of H_2S gas on pristine 2D-ZnO, and explored how it can be enhanced through (a) substitutional nitrogen doping at oxygen sites and (b) introduction of O-vacancies. We have also examined the possibility of existence of Stone-Wales in 2D-ZnO, that might alter its interaction with H_2S.

5.2.2 Computational Details

Our first-principles calculations are based on density functional theory (DFT) as implemented in Quantum ESPRESSO package [45]. A local density approximation to the exchange-correlation energy functional is known to overestimate the binding energies, particularly the interaction of molecules with a surface. We have used a generalized gradient approximation (GGA) of Perdew Burke-Ernzehof (PBE) parameterized form [44] because the charge density varies more rapidly in the space

between a molecule and the adsorbing surface, and gradient corrections can be significant. Secondly, such interaction involves van der Waals (vdW) long range interactions whose parameterization is available along with a GGA functional implemented using Grimme scheme [49]. Since the improvised GGA functionals are known to give more accurate binding energies [43, 166, 167], we adopt the use of GGA in present calculations. We use plane wave basis with energy cutoffs of 30 Ry and of 180 Ry in representation of wave function and density respectively, and ultrasoft pseudopotentials [47] to represent the interaction between ionic cores and valence electrons. We employ periodic boundary conditions with 3 x 3 x 1 or 4 x 4 x 1 supercell (18 or 32 atoms) of 2D-ZnO with different concentrations of coverage of H_2S, and include a vacuum of 12 Å, in the direction perpendicular to 2D-ZnO sheet to keep interactions between periodic images low. We use uniform mesh of 7 x 7 x 1 k-points in sampling integrations over Brillouin zone, and smear the occupation numbers of electronic states with Fermi-Dirac distribution and smearing width (k_BT) of 0.04 eV. We consider configurations with different structural orientations and coverage of H_2S varying defect concentration and relax the structure to minimize energy until the Hellmann-Feynman forces on each atom is less than 0.03 eV/Å in magnitude.

Results and Discussions

5.2.3 Structure and stability of 2D-ZnO

Monolayer form of ZnO has a honeycomb lattice structure similar to BN [Figure 5.6a]. Our estimate of its lattice constant, a = 3.30 Å is in good agreement with Topsakal *et al.* (a_{GGA}=3.28Å) [168]. The 2D-ZnO is sp^2 hybridized with a Zn-O bond length of 1.89 Å, 5% less than the 3D equivalent (2 Å) of ZnO with sp^3 hybridization [168]. To bench mark our results, we have estimated the cohesive

energy, and analyzed the electronic structure and vibrational spectra of 2D-ZnO, and compared with the available results of Topsakal and coworkers [168], where they have used GGA approximated exchange-correlation energy functional of Perdew-Wang 91 (PW91) parameterized form. Cohesive energy(E_{coh}) of ZnO monolayer is determined using,

$$E_{coh} = E_T(2D - ZnO) - E_a^{isolated}(Zn) - E_a^{isolated}(O) \tag{5.4}$$

where, E_T is the total energy of the system and $E_a^{isolated}$ is the total energy of an isolated atom. Our estimate of E_{coh} is 8.29 eV per formula unit, in good agreement with Topsakal *et al.* (8.42 eV) [168]. Electronic structure of 2D-ZnO [Figure 5.6b] shows that it is a direct band gap semiconductor with a gap of 1.62 eV. Taking into account the fact that band gaps are usually underestimated in DFT calculations, we expect 2D-ZnO to be rather a good insulator. We project out the density of states on individual atoms and orbitals to study the character of valence and conduction bands [Figure 5.6b]. Energy band immediately below the gap, the valence band (-4 to -1.5 eV) is constituted primarily of p-orbital's of O and weakly of d-orbitals of Zn. Valence band deeper in energy (< -4 eV) arises from the d-orbitals of Zn. Upper conduction bands are primarily constituted of the s-orbitals of Zn.

Phonon spectrum, which is obtained as eigenvalues of the Hessian of total energy (dynamical matrix, second derivative of total energy with respect to atomic positions) reveal the structural stability of the system. Theoretical phonon dispersion of 2D-ZnO reveals that planar ZnO is locally stable [Figure 5.6c], and weak instabilities of the ZA branch (out-of-plane acoustic mode) around the Γ point is an artifact of a finite mesh size [168]. Our results for phonon dispersion shows similar behavior as predicted by Topsakal *et al* [168].

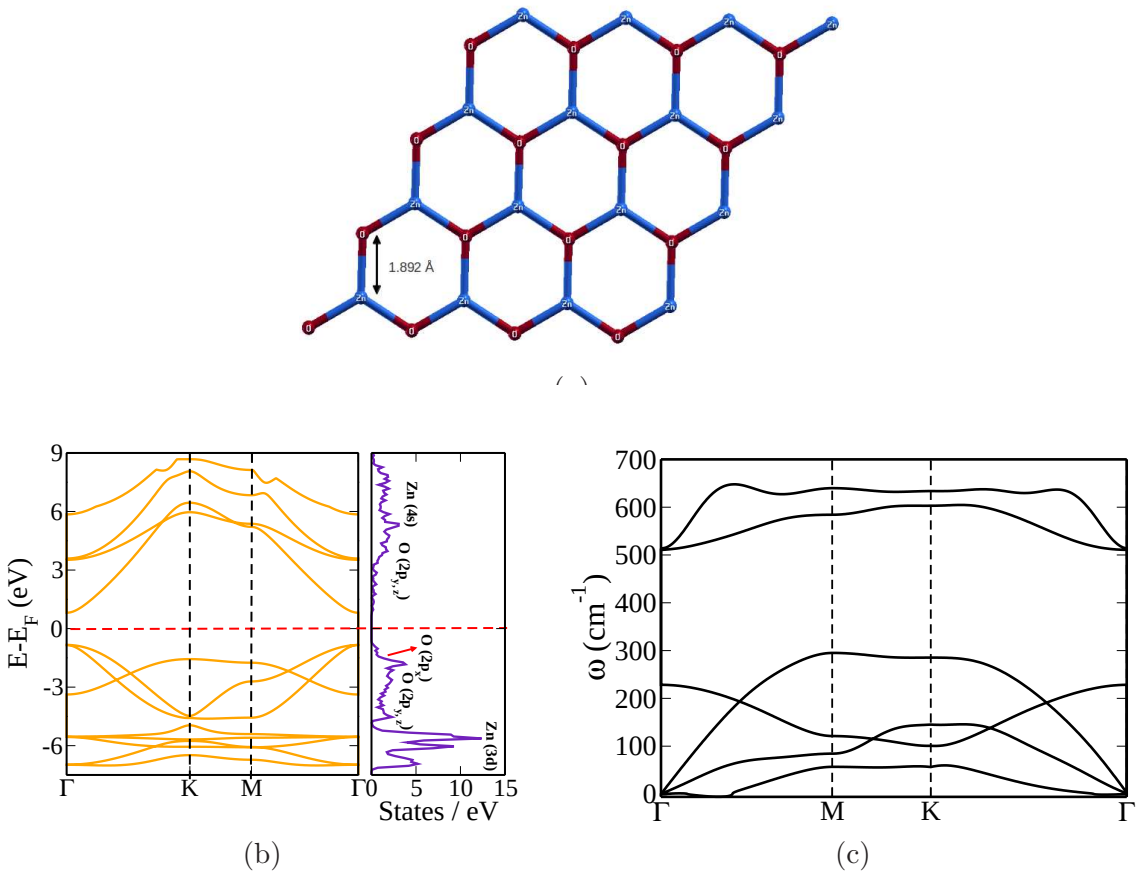

(b) (c)

Figure 5.6: (a) Relaxed structure,(b) electronic structure and (c) phonon dispersion of 2D monolayer ZnO. Reproduced by permission of the Royal Society of Chemistry.

5.2.4 Configurations of complex

We have considered four inequivalent configurations of 2D-ZnO-H_2S complex with different orientations of H_2S at various sites of the 2D-ZnO sheet: a) H_2S on the top of the center of the hexagonal ring, with the H atoms pointing away (configuration I), and towards (configuration II) the 2D-ZnO sheet, b) H_2S on top of the Zn-O bond with H and S lying in the same plane parallel to 2D-ZnO sheet, H near O (configuration III) and away from O (configuration IV).

To quantify the strength of interaction between H_2S and 2D-ZnO, we obtain

adsorption energy (E_A), as follows

$$E_A = \frac{E_{2D-ZnO-H_2S} - E_{2D-ZnO} - nE_{H_2S}}{n} \tag{5.5}$$

where $E_{2D-ZnO-H_2S}$, E_{2D-ZnO}, E_{H_2S} are the total energies of the optimized structures of 2D-ZnO-H_2S complex, 2D-ZnO, isolated free H_2S molecule respectively, and n is the total number of H_2S molecules. Our results clearly reveal that, E_A<0 with magnitudes from -30 to -17 kJ mol^{-1}[Table 5.5] revealing a relatively weak adsorption of H_2S on 2D-ZnO. These values are intermediate to those of physisorption and chemisorption. Among these configurations, the configuration II with $E_A = -29.7$ kJ mol^{-1} is energetically more stable with the H_2S adsorbed at the center of ring and the H atoms oriented towards the 2D-ZnO sheet [Figure 5.7b].

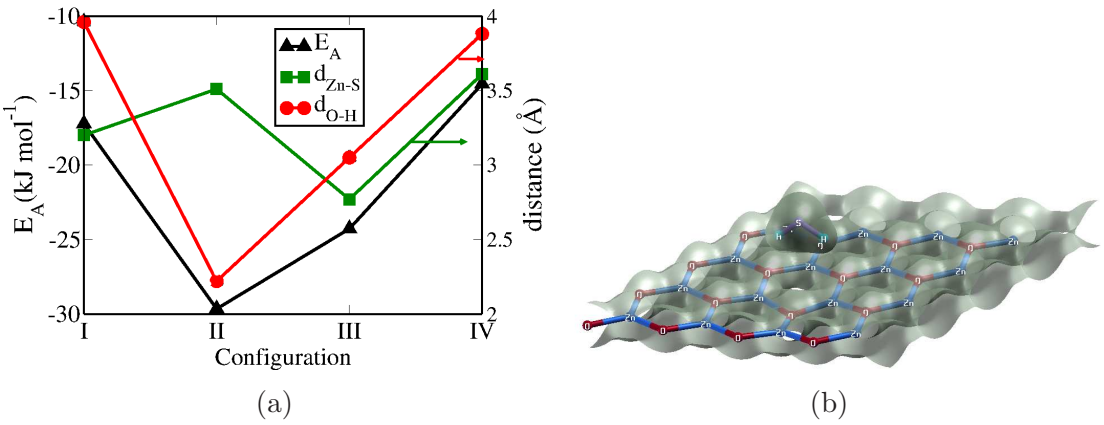

Figure 5.7: (a) Adsorption energy, nearest distances between the H_2S molecule and 2D-ZnO sheet for different configurations, (b) charge density plot for the coverage of 130.89 mg of H_2S per g of 2D-ZnO. Reproduced by permission of the Royal Society of Chemistry.

To identify the mechanism of adsorption at the atomistic level, we now consider the most stable configuration (configuration II). We find that only a few Zn-O bonds length in the vicinity of the adsorbed H_2S molecule change slightly, indicating a weak interaction between 2D-ZnO and H_2S. Zn-O bonds elongate by 0.8%, and there is

Table 5.5: Energy of Adsorption, E_A (kJ mol^{-1}) with nearest distances between the substrate and molecule for various configurations.

		Nearest distance	
Configuration	E_A	d_{Zn-S} (Å)	d_{O-H} (Å)
I	−17.2	3.2	3.96
II	−29.7	3.51	2.22
III	−24.3	2.77	3.05
IV	−14.6	3.61	3.88

slight bending (3.2°) in the 2D-ZnO sheet, while the H-S bond elongates by 1%. The distance between H_2S molecule and 2D-ZnO (O-H distance is 2.2 Å) is longer than a typical O-H bond length. To understand the nature of the interaction, we visualize the charge density plot of 2D-ZnO-H_2S complex [Figure 5.7b]. Charge density isosurface shows a weak electrostatic interaction between H_2S molecule and the substrate.

We estimate the van der Waals contribution (E_A^v):

$$E_{A^v} = \frac{E_{2D-ZnO-H_2S^v} - E_{2D-ZnO^v} - nE_{H_2S^v}}{n}, \tag{5.6}$$

where E_{x^v}, with x = 2D-ZnO-H_2S, 2D-ZnO, H_2S is the respective energy contribution due to dispersion correction. The vdW contribution(E_{A^v}) of configuration II is −24.4 kJmol^{-1} (where E_A= −29.7 kJmol^{-1}), showing that most of the binding during adsorption arises from vdW interactions.

5.2.5 Dependence of adsorption on H_2S coverage

The change in adsorption energy as a function of coverage of H_2S (for coverages of 26−230 mg of H_2S per g of 2D-ZnO) shows the same relative stability of four configurations, hence we will focus on the most stable configuration II. The amount of H_2S was varied while keeping the size of 2D-ZnO supercell (4 x 4 x 1) the same. We find that adsorption energy increases with concentration of H_2S, and saturates at

coverages greater than 200 mg of H_2S per g of 2D-ZnO [Figure 5.8a]. The adsorption energy increases with concentration due to (a) an increase in the intramolecular interaction (E_{A^v}(HS)) between the condensed H_2S molecules, (E_{A^v}(HS) is calculated by freezing the H_2S molecules after isolating it from the complex), and (b) nearest distance between the H_2S molecules and 2D-ZnO sheet decreases (from 2.2 to 1.7 Å), which is less than the sum of the van der Waal radii of O (1.5 Å) and H (1 Å), resulting in electrostatic interaction. The vdW contribution to the overall adsorption energy decreases, as the repulsive term in the potential energy becomes dominant at shorter distance between H_2S molecules and 2D-ZnO sheet, which becomes further less than the sum of van der Waal radii with coverage of H_2S [Figure 5.8a]. At higher coverages, buckling in 2D-ZnO is also significant, at the places where cations and anions (O and H, Zn and S) come close to each other. Here, visualization of charge density shows a relatively large overlap between densities of H_2S molecules and of the substrate indicating relevance of electrostatic interaction [see Inset Figure 5.8b for coverage of 130 mg of H_2S per g of 2D-ZnO].

We now examine the electronic structure (DOS) of 2D-ZnO with and without absorbed H_2S molecules. The Fermi level is set to 0 is all the three cases [see Figure 5.8b with the coverage of 130 mg of H_2S per g of 2D-ZnO]. Comparing the DOS of 2D-ZnO, frozen/condensed H_2S molecule and the complex, we see a weak overlap of wavefunctions of H_2S with 2D-ZnO, and a slight increase in band gap by $\sim$0.2 eV indicating a weak covalent interaction of 2D-ZnO with H_2S molecules, primarily associated with the interaction of p-orbitals of O with s-orbitals of H and s-orbitals of Zn with p-orbitals of S.

To understand further the adsorption, we have determined the charges using Löwdin method as implemented in Quantum ESPRESSO and estimated the charge transfer:

$$QT = Q^{H_2S}_{2D-ZnO-H_2S} - Q^{H_2S}_{frozen} \tag{5.7}$$

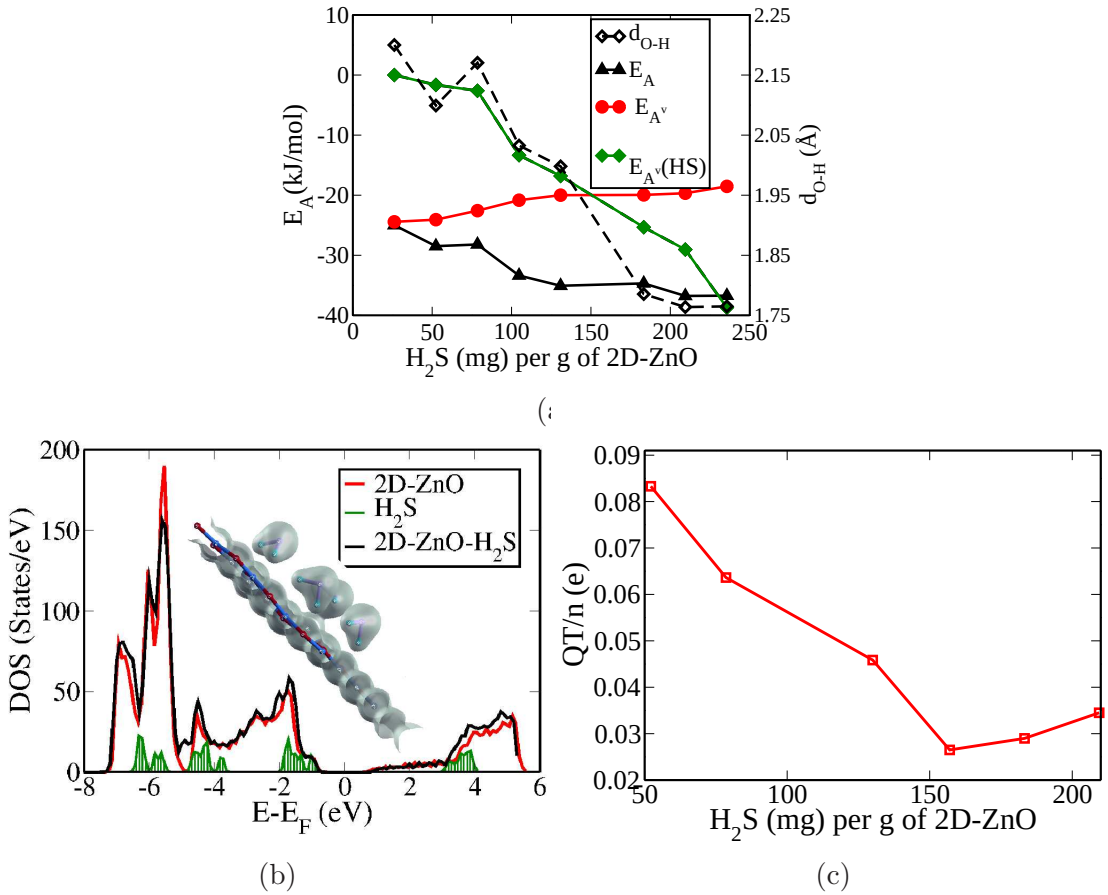

Figure 5.8: (a) Energy of adsorption, vdW contribution to total adsorption of H_2S on 2D-ZnO sheet as a function of coverage with the smallest distance between H_2S and 2D-ZnO sheet, (b) comparison of the electronic density of states of the complex with the coverage 130 mg of H_2S per g of 2D-ZnO with the pristine 2D-ZnO, inset shows charge density plot of the complex, and (c) total charge transfer per molecule from the substrate to molecules with respect to coverage. Reproduced by permission of the Royal Society of Chemistry.

where QT is the charge transfer, $Q^{H_2S}_{2D-ZnO-H_2S}$, $Q^{H_2S}_{frozen}$ is the sum of total charge on the atoms in frozen H_2S molecules, a positive value indicates the transfer of an electron from the substrate to molecule(s).

From the amount of charge transfer as a function of the coverage of H_2S [Figure 5.8c], it is clear that the total charge (e) transfer from the substrate to molecule increases with concentration, while the charge transfer per molecule (QT/n) decreases till $n = 6$ (156 mg of H_2S per g of 2D-ZnO), and increases with further increase in

coverage. The total charge transfer varies from 0.1 to 0.25 electron, for the coverages studied here, responsible for a weak electrostatic interaction between the H_2S and 2D-ZnO substrate. Thus the adsorption of H_2S on 2D-ZnO is intermediate to physisorption and chemisorption with mixed vdW, electrostatic and weak covalent interactions.

5.2.6 Defects in 2D-ZnO and their effects on adsorption

Stone-Wales defects

Stone-Wales (SW) defects are topological defects observed in two dimensional systems such as graphene and its sp^2 analogues [169]. We have explored the possibility of the existence of SW defects in 2D-ZnO obtained by in-plane rotation of one of the Zn-O bonds by 90°. On structural relaxation, we see that the Zn-O bond comes back to its original unrotated position, indicating that a SW defect is unstable. Stone-wales defects in other heteronuclear graphene analogues such as BN are known to be a meta-stable state due to high formation energy of homonuclear bonds between B-B and N-N, but the formation of Zn-Zn bond is very unlikely due to higher oxidation state and ionic size [170, 171]. We also considered the case in which one of the Zn-O bond is rotated out-of-plane by 90°, and see that on relaxation the out-of-plane Zn-O comes back to the original position, indicating that bond rotation does not lead to any metastable point defect formation.

N-substitution on oxygen site

We determined the effects of nitrogen substitution in 2D-ZnO, by replacing oxygen atoms with nitrogen. We considered N-substituted 2D-ZnO by replacing one of the oxygen atoms with nitrogen atom initially in a 4 x 4 supercell of 2D-ZnO. Structural relaxation and phonon reveal a weak instability leading to out-of-plane displacements

($\sim$ 0.03 to 0.05 Å) of the adjacent Zn and O atoms with a moderate energy cost of 1.14 eV per N atom. Electronic band structure reveals the presence of bands at Fermi level associated with p-orbital of nitrogen, similar to the isolated band corresponding to p-orbital of nitrogen in bulk ZnO resulting from substitutional doping with n-type elements (N and F) reported by Saha *et al.* [154] [Figure 5.9a for electronic band structure of 2D-$ZnO_{1-x}N_y$ (black curve) with doping concentration 11%].

We have placed a H_2S molecule at a distance of 1 Å from the N-site with H facing towards the sheet, and relaxed the structure. We find a rather strong interaction of H_2S molecule and doped 2D-ZnO, with H_2S molecule dissociating to H^+ and HS^-. The doped 2D-ZnO sheet undergoes a local structural distortion involving bending by 5° and elongation of few Zn-O bonds ($\sim$4%) near H_2S. The charge density shows a strong overlap of densities of N of doped 2D-ZnO and isolated H^+ of H_2S forming a strong covalent bond (d_{H-N}=1.03 Å), whereas HS^- weakly interacts with Zn (d_{Zn-HS}=2.46 Å) [Figure 5.9b]. The adsorption energy increases drastically to -152 kJ mol^{-1}. On comparing, the projected density of states of the complex with the substrate (not shown here), we observe that the increase in the adsorption is mainly due to overlap of s-orbital of H^+ with p-orbitals of N and there is a slight increase in the distance between HOMO and LUMO levels, with vanishing density of states at the Fermi level in the complex.

We now study the effect of concentration of substitutional nitrogen doping on the adsorption. We have considered a 3 x 3 x 1 supercell of ZnO with doping concentration varying from 5.5 to 22.2 atomic percent. Freezing of unstable modes to distort this structure leads to bending in 2D-$ZnO_{1-x}N_y$ sheet with out-of-plane displacement ($\sim$ 0.2 to 0.3 Å) of adjacent atoms with reasonable formation energy ($\sim$0.9 eV to 1.1 eV/N atom). We have placed the H_2S molecule at a distance of 1 Å above one of the nitrogen atoms with hydrogen atoms closer to the sheet.

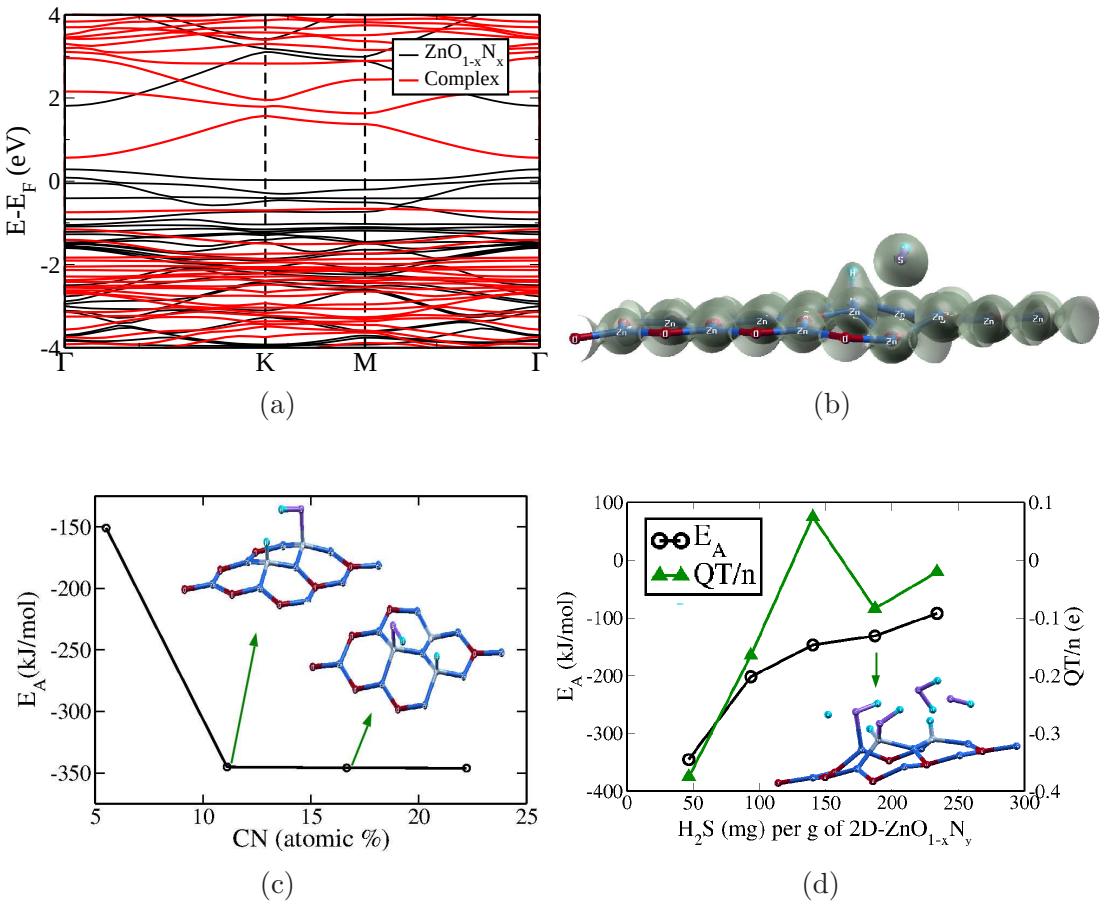

Figure 5.9: (a) Comparison of electronic band structure of 2D-$ZnO_{1-x}N_y$ and its complex with coverage of 93.6 mg of H_2S per g of 2D-$ZnO_{1-x}N_y$, (b) charge density plot of a complex with doping concentration(CN) 3.1% and H_2S coverage 26 mg per g of 2D-$ZnO_{1-x}N_y$, (c) adsorption energy as a function of doping concentration for a coverage of 46.8 mg of H_2S per g of 2D-$ZnO_{1-x}N_y$. The inset figures corresponds to doping concentration 11% (left) and 16.7% (right), and (d) adsorption energy as a function of H_2S coverage for a fixed doping concentration (11.1% N), the inset figure corresponds to H_2S coverage of 189.2 mg per g of 2D-$ZnO_{1-x}N_y$. Reproduced by permission of the Royal Society of Chemistry.

The adsorption energy increases till 11% doping concentration and saturates for higher doping concentration for a coverage of 46.8 mg of H_2S per g of 2D-$ZnO_{1-x}N_y$ [Figure 5.9c]. As the concentration of nitrogen increases, the charge transfer from the molecule to substrate increases and distance between dissociated H_2S molecule and substrate decreases as the substrate becomes more electronegative [see Inset Figure 5.9c]. The position and orientation of H_2S molecule is very important, as the

strength of adsorption decreases drastically when placed away from the vicinity of defect site.

For a fixed doping concentration (11%), we vary the concentration of the H_2S from 46.8 to 234 mg of H_2S per g of 2D-$ZnO_{1-x}N_y$. As the coverage of H_2S increases, the adsorption energy per molecule decreases [Figure 5.9d]. An increased electrostatic interaction between H_2S molecules and the substrate is evident from structural distortion of the relaxed structure. It is clear in the electronic structure for a coverage of 93.6 mg of H_2S [Figure 5.9a], the sub-bands at the Fermi level corresponding to p-orbitals of nitrogen shift down in energy opening a gap, and the gap increases with the coverage of H_2S, due to the formation of strong covalent bond with H leading to the splitting of H_2S. The decrease in adsorption energy can be attributed to (a) saturation of nitrogen dangling bonds, (b) decrease in the average distance between the H_2S molecules and substrate and (c) decrease in the total charge transfer with concentration, though charge transfer per molecule is same.

Oxygen vacancies

We now determine how oxygen vacancies in 2D-ZnO influence the adsorption of H_2S. Removing one of the oxygen atoms from the pristine 4 x 4 supercell of 2D-ZnO, i.e, creating a vacancy of 3.15 atomic percent, We first optimized the structure. Our estimate of the formation energy of oxygen vacancy is a bit high (8.05 eV/vacancy). We initially placed H_2S molecules at a distance of 1 Å from the O-vacancies with H and S in same plane parallel to the sheet. We find that the presence of oxygen vacancy leads to a negligible increase in the adsorption energy ($\sim$ 1 kJmol^{-1}) of H_2S.

We now increase the coverage of H_2S and place H_2S molecules in the vicinity of an oxygen vacancy. At lower coverages of H_2S ($\leq$52 mg of H_2S per g of 2D-ZnO_{1-x}), there is negligible effect on the strength of adsorption. As the coverage of H_2S

increases adsorption energy increases due to an increase in electrostatic interaction among the H_2S molecules and the substrate, this is evident in structural distortions that lead to splitting of H_2S accompanied by the formation of H_2 molecule [Figure 5.10a]. The primary reason for the splitting of H_2S is that O-vacancy site is replaced by S of H_2S indicating essential role of O-vacancy in H_2 production [Inset Figure 5.10a]. The above reaction can be written as

$$2D - ZnO_{1-x} + 2H_2S \rightarrow H_2 + HS\text{–}(2D - ZnO_{1-x})||||HS, \tag{5.8}$$

To calculate the amount of energy required to separate the H_2 from the complex, we have displaced the H_2 away from substrate. The amount of energy required to separate the H_2 molecule from the complex is quite low ($\sim$0.07 eV/molecule), indicating that 2D-ZnO_{1-x} may be a good candidate for the production of hydrogen fuel [Figure 5.10b, where d_o is the distance between the substrate and H_2 molecule in the relaxed structure, d is the distance of H_2 from the equilibrium position in the relaxed structure and E_o, E_d is the corresponding energy]. To explore the disproportionation of two HS radicals present at the adjacent adsorption sites, given by

$$HS^* + HS^* \rightarrow H_2S + S^*, \tag{5.9}$$

we have decreased the distance between two HS radicals and relaxed the structure. We see a strong repulsion between HS radicals leading to no disproportionation at low concentration of vacancy and coverage of H_2S.

To explore the reusability of defected material, we calculate the energy required to regenerate 2D-ZnO_{1-x} (E_R) from the sulphonated 2D-ZnO_{1-x}. E_R is determined using,

$$E_R = E_{2D-ZnO_{1-x}} - [E_{2D-ZnO_{1-x}S_x} - E_a^{isolated}(S)] \tag{5.10}$$

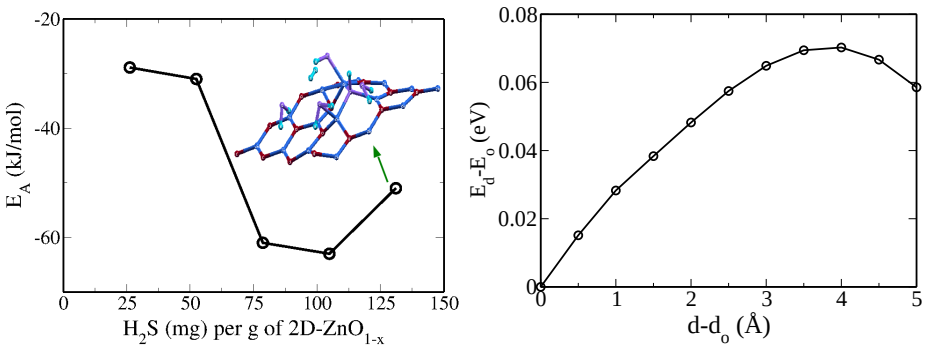

(a) (b)

Figure 5.10: (a) Adsorption energy as a function of H_2S coverage for a fixed oxygen vacancy, the inset figure corresponds to coverage of 130 mg of H_2S per g of 2D-ZnO_{1-x}, and (b) difference in energy of system with H_2 displaced at distance of d (Å) away from the equilibrium distance (d_o) in the relaxed structure for a coverage of 130 mg of H_2S per g of 2D-ZnO_{1-x}. Reproduced by permission of the Royal Society of Chemistry.

where, $E_{2D-ZnO_{1-x}}$, $E_{2D-ZnO_{1-x}S_x}$ and $E_a^{isolated}(S)$ are the total energies of 2D-ZnO_{1-x}, sulphonated 2D-ZnO_{1-x} and isolated sulphur atom respectively. Our estimate of energy cost of regenerating 2D-ZnO_{1-x} with 3.15 atomic percent sulphonated 2D-ZnO_{1-x} is 4.15 eV/S atom, which is less compared to formation energy of 3.15 atomic percent oxygen vacancy in prisitine 2D-ZnO (8.05 eV/vacancy), indicating that regeneration of 2D-ZnO_{1-x} from 2D-$ZnO_{1-x}S_x$ is easier compared to introducing oxygen vacancies.

5.2.7 Selectivity of adsorbate molecules on 2D-ZnO_{1-x}/2D-$ZnO_{1-x}N_y$

To check the selectivity of H_2S over other potentially reactive species like CO_2 and H_2O on defected 2D-ZnO, we have intially placed single gas molecule of CO_2/H_2O in the vicinity of oxygen vacancy at a distance of 1 Å from the substrate (2D-ZnO_{1-x}, 3.15 atomic percent oxygen vacancy). For the low concentrations of CO_2 considered (34 mg of CO_2 per g of 2D-ZnO_{1-x}), the E_A is positive (30 kJ/mol)

indicating no adsorption, where as H_2O bonds relatively stronger than H_2S, since O is more electronegative than sulphur. In neither of the cases (CO_2 or H_2O), the adsorbed gas molecule dissociates and fills the oxygen vacancy. We have also studied selectivity of H_2O over H_2S in presence of N-doping (3.15 atomic percent N-doping), We find that H_2O unlike H_2S does not dissociate to saturate the dangling bonds of N, instead bonds weakly with 2D-$ZnO_{1-x}N_y$ [Table 5.6]. H_2S binds preferrentially over CO_2/H_2O

Table 5.6: Comparison of energetics for selectivity of H_2S over CO_2 and H_2O.

Substrate	Molecule	E_A (kJmol^{-1})
2D-ZnO_{1-x}	H_2S	-28.9
	CO_2	30.3
	H_2O	-43.2
2D-$ZnO_{1-x}N_y$	H_2S	-151.0
	H_2O	-35.4

5.2.8 Conclusion

We find that the adsorption of H_2S on pristine 2D-ZnO is weak and mainly due to the van der Waals interaction for lower coverage of H_2S, and H_2S molecule prefers to occupy the site at center of hexagonal ring with the H atoms pointing towards the oxygen atoms of the substrate. N-substitution at O-sites leads to a marked increase in adsorption energy (by $\sim$5 times) with respect to the pristine 2D-ZnO, resulting in dissociation of H_2S. The adsorption energy increases with doping concentration and saturates above 11% defect concentration for a coverage of 46.8 mg of H_2S per g of 2D-$ZnO_{1-x}N_y$. When the coverage of H_2S increases for a fixed N-doping concentration, we see that the adsorption energy per molecule decreases due to saturation of N-dangling bonds, the decrease in the total charge transfer as well as an increase in the average distance between all the H_2S molecules and the substrate. O-vacancy has little effect on the adsorption at lower coverages of H_2S, but it strengthens with

an increase in the coverage due to electrostatic interactions. This leads to splitting of H_2S molecules in which S relocates to the site of O-vacancy in 2D-ZnO_{1-x} and H_2 is released. We find that the SW defects are unstable in 2D-ZnO.

Thus, we find that both N-substitution and O-vacancies in 2D-ZnO facilitate capture of H_2S and its splitting to generate H_2. The former has applications in maintaining a clean environment and the latter is useful as a green fuel for energy. In fact, the end product after consumption of this fuel is water which also enriches the quality of environment.

Chapter 6

Effect of nitrogen substitution in V_2O_3 on the metal-insulator transtion*

6.1 Introduction

Metal-insulator transitions constitute a fascinating aspect of the physics and chemistry of materials. M-I transitions have been found in many metal oxides, sulphides and other materials and the transition in metal oxides (VO_2, V_2O_3 and V_2O_5) has received considerable attention due to their very sharp transition temperature [173, 174]. This sharp temperature driven metal-to-insulator transition in these materials can be principally be used for gas sensing based on transition edge sensing phenomena largely known for superconducting materials [175]. However, the usage of superconducting sensing elements is quite expensive due to the requirement of cryogenic temperatures and at the same time realising these experimentally is difficult. Recently, the sharp change in conductivity of VO_2 has been

*This work has been published in *ChemPhysChem* [172]. Copyright (2015) by John Wiley & Sons, Inc., URL:*htpp://dx.doi.org/10.1002/cphc.201500439*.

proposed as a working principle for critical temperature sensors in gas sensing and uncooled TES microbolometers [176, 177]. The M-I transition in V_2O_3 is noteworthy because of 10-million fold jump in resistivity that occurs sharply around 150 K [173, 174]. The transition is accompanied by a change in the crystal structure (corundum-monoclinic) and magnetic properties (paramagnetic-antiferromagnetic). It is reported that pressure suppresses the transition temperature rendering the material metallic down to the lower temperature [173, 174]. Substitution of Ti and Cr have marked effect on the transition, with Ti exhibiting a positive pressure effect and Cr exhibiting negative pressure effect [173, 174]. Aliovalent anion substitution has been reported to have a significant effect on the M-I transition in case of VO_2 [178].

In this work, we explore the sensitivity of M-I transition of V_2O_3 on N-substitution. Nitesh *et al.*, [172] has experimentally investigated the effect of N-doping on the paramagnetic-antiferromagnetic transition associated with the metal-insulator transition of V_2O_3. They have found that the transition temperature of V_2O_3 is lowered to $\sim$120 K in the N-doped samples revealed by both the electrical resistivity and magnetic data [Figure 6.1]. In this chapter, we have carried out first-principles studies to understand how nitrogen-substitution affects the M-I transition of V_2O_3.

6.2 Computational Details

Our calculations are based on first-principles density functional theory (DFT) as implemented in QUANTUM ESPRESSO package [45], with interaction between ionic cores and valence electrons represented using ultrasoft pseudopotentials [47]. We use local spin density approximation of Perdew Burke-Ernzehof (PBE) parameterized form [44] and apply Hubbard U correction to treat on-site correlations of d-electrons of vanadium with U_{eff} = 3.5 eV, generally used for vanadium based systems [179].

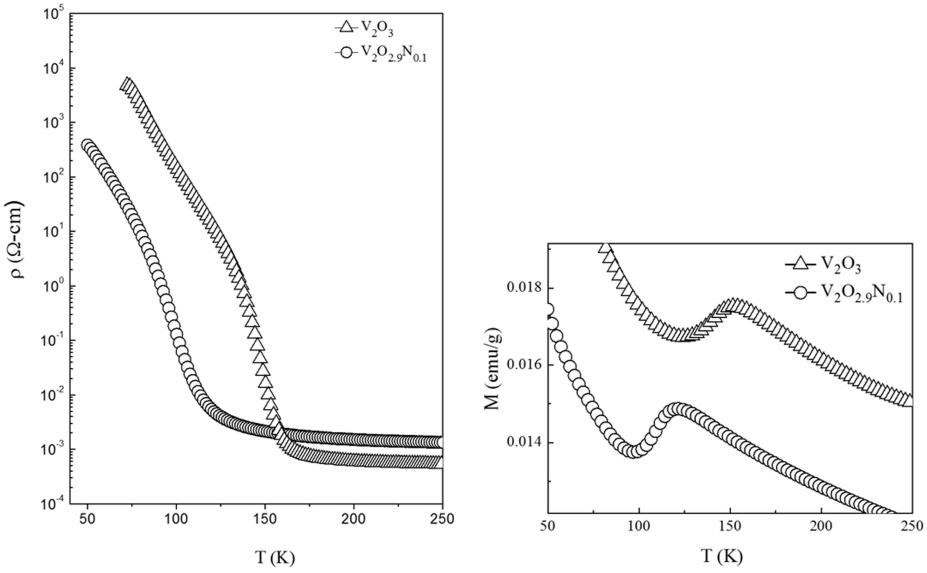

(a) (b)

Figure 6.1: Electrical resistivity and Magnetic data of bulk samples of V_2O_3 and $V_2O_{2.9}N_{0.1}$. Copyright (2015) by John Wiley & Sons, Inc.

We employ plane wave basis truncated with energy cutoffs of 30 Ry and of 180 Ry in representation of wave functions and charge density respectively. Within periodic boundary conditions, suitable supercells of monoclinic and corundum structures of V_2O_3 are used to model desired concentration of anion dopant. We use uniform mesh of 4 x 4 x 6 and 4 x 6 x 6 k-points in sampling integrations over Brillouin zone of corundum and monoclinic structures respectively, and smear the discontinuity in the occupation numbers of electronic states at Fermi level using Fermi-Dirac distribution with smearing width (k_BT) of 0.04 eV. We relax the structure to minimize energy until the Hellman-Feynman forces are less than 0.03 eV/Å in magnitude.

6.3 Results and Discussion

6.3.1 Structure and electronic properties

Crystalline V_2O_3 exists in two phases, anti-ferromagnetic (AFM) monoclinic phase (m-V_2O_3) below the Nèel temperature (T_N) and paramagnetic corundum phase (r-V_2O_3) at $T>T_N$, belonging to I2/a and R$\bar{3}$C space groups respectively [Figure 6.2a and 6.2b] [180]. The monoclinic phase is insulating and has a c-type AFM structure. Our estimates of lattice constants of the monoclinic phase are $a = 7.39$ Å , $b = 5.17$ Å and $c = 5.58$ Å , and those of corundum phase are $a = b = 4.90$ and $c = 14.22$ Å , which are within the typical DFT errors [180] with respect to their experimental values. Energetics reveal that the monoclinic phase of V_2O_3 is relatively more stable than the corundum phase (i.e., $\Delta E = E^m\text{-}E^r$ = -1.57 eV/f.u.; where E^m and E^r are the total energies of monoclinic and corundum phases respectively).

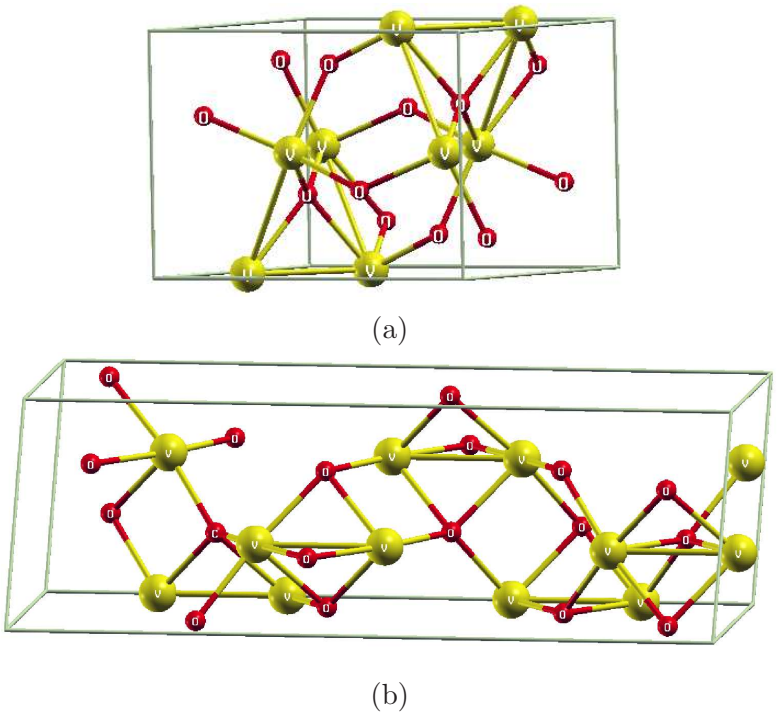

(a)

(b)

Figure 6.2: Crystal structure of V_2O_3 in AFM monoclinic (a) and NM corundum (b) phases. Copyright (2015) by John Wiley & Sons, Inc.

To benchmark our results further, we have analyzed the electronic structure of bulk m-V_2O_3 and r-V_2O_3. We find m-V_2O_3 exhibits a direct band gap of 1.23 eV, which is probably underestimated, as is typical of DFT, and we expect it to be an insulating material [Figure 6.3a]. On the other hand, r-V_2O_3 is metallic [Figure 6.3b]. Analysis of the projected density of states (PDOS) of m-V_2O_3 reveals that energy bands immediately below the gap are mainly constituted of *d*-orbitals of V and partially of *p*-orbitals of O, while conduction bands (just above the gap) are also contributed by *d*-orbitals of V, suggesting that the electronic gap of m-V_2O_3 arises from correlations, crystal field splitting and AFM superexchange [Figure 6.3c; V1, V2 represent V atoms with opposite spins]. In r-V_2O_3, the *d*-orbitals of V lie at the Fermi level with a slight contribution from *p*-orbitals of O, consistent with its weaker stability according to Stoner's criterian [Figure 6.3d].

6.3.2 Energetics of aliovalent substituted V_2O_3

To understand the observed reduction in Nèel temperature in experiments upon N-substitution in V_2O_3, we have studied three materials with different composition in both monoclinic and corundum phases i.e., (i) N substituted V_2O_3 with oxygen vacancy ($V_2O_{3-x}N_y$; 3y = 2x), (ii) N-substituted V_2O_3 ($V_2O_{3-x}N_y$; x = y), and (iii) O vacancy in V_2O_3 (V_2O_{3-x}; y = 0). The formation energy(E_f) of a substitution or vacancy defect is calculated using

$$E_f = E_{V_2O_{3-x}N_y} - E_{V_2O_3} + x.E_O - y.E_N \tag{6.1}$$

where E_α (α = $V_2O_{3-x}N_y$, V_2O_3) is the total energy of the corresponding system and E_β (β = N, O) is the energy of the corresponding isolated atom.

To correlate our results with experiment, we have considered a 2 x 2 x 1 periodic supercell of monoclinic phase containing 80 atoms and of corundum phase containing

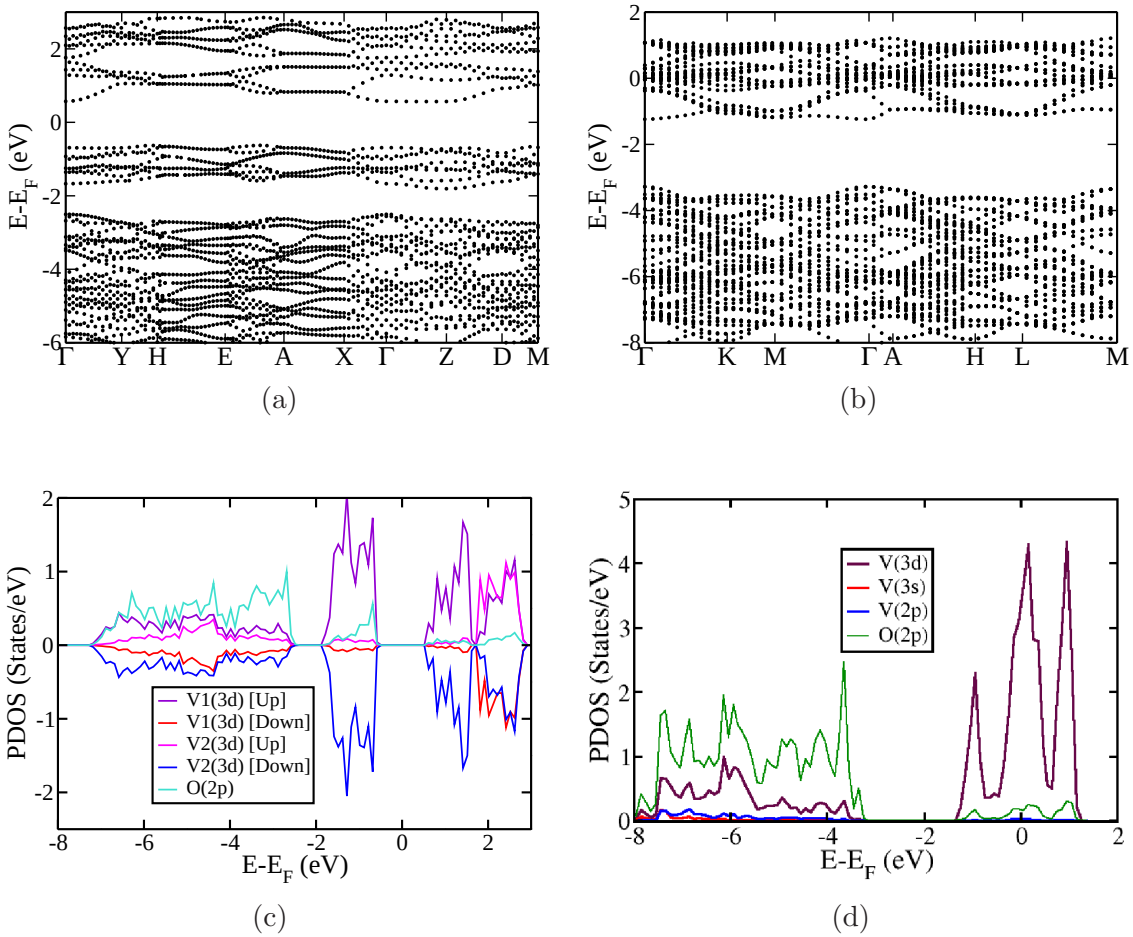

Figure 6.3: Electronic structure (a, b) and projected density (c, d) of electronic states of V_2O_3 in AFM monoclinic and NM corundum phases respectively. Copyright (2015) by John Wiley & Sons, Inc.

120 atoms. Substitution of N in V_2O_3 would be accompanied by oxygen vacancies to maintain charge neutrality. To simulate $V_2O_{3-x}N_y$, we have substituted three O atoms with two N atoms and O-vacancy in the supercell of 80 and 120 atoms of monoclinic and corundum structures respectively. This can be done in many ways or configurations. For simplicity and based on work of Pan *et al.* [181], we have substituted them bonded to the same V atom amounting to 3.75 at% concentration in monoclinic phase and 2.50 at% in corundum phase. We find that the formation energy of $V_2O_{3-x}N_y$ is quite high (∼6.7 - 8 eV/2N/vacancy) and, this is mainly due to the presence of oxygen vacancy (since E_f for V_2O_{3-x} is ∼9.22 − 9.31) [see

Table 6.1]. Our results clearly show that substitution of N in V_2O_3 with O-vacancy is relatively easier in the corundum phase (ΔE_f = -2.51 eV/2N, where $\Delta E_f = E_f^{V_2O_{3-x}N_y}$ - $E_f^{V_2O_{3-x}}$) than in monoclinic phase (ΔE_f = -0.64 eV/2N). Hence, N substitution and the accompanying oxygen vacancies reduce the energy of the high-temperature metallic phase relative to the insulating phase, leading to reduction in the Nèel temperature observed in experiments here. understand the structural origin of changes in the electronic structure upon inclusion of impurity (N-substitution or O-vacancies).

Table 6.1: Comparison of formation energies of defects in monoclinic and corundum phases of V_2O_3.

	Formation Energy (E_f)		
Units of E_f	System	Monoclinic	Corundum
eV/2N/vacancy	$V_2O_{3-x}N_y$	8.67	6.72
eV/N	$V_2O_{3-x}N_x$	-0.07	-1.37
eV/vacancy	V_2O_{3-x}	9.31	9.22

6.3.3 Bond valence analysis

To understand the observed change in T_N and relative stability of corundum phase, we now present bond valence analysis and understand the structural origin of changes in the electronic structure upon inclusion of impurity (N-substitution or O-vacancies). From the bond valence analysis, we see that V-O and V-V bond lengths of V atom attached to N impurity in m/r-$V_2O_{3-x}N_y$ are approximately 3.5-5% longer and 3.8-4.3% shorter respectively than those in the corresponding structures of pristine V_2O_3 [see Table 6.2]. The V-N bond length is relatively shorter by ∼1-5% (∼1.90-1.98, Å) compared to V-N complexes reported in literature [182]. We find a reduction in lattice parameters by ∼2-3% with respect to the corresponding pristine structures. The overall structural change in V_2O_3 on substitution of N accompanying O-vacancy involves a drastic decrease in the effective coordination number (ECN) ∼4.85 for V

attached to N impurity and negligible change in the ECN of V(∼5.82) in the vicinity of site of substitution. Thus, short V-N bonds constitute the structural origin of the significant changes in electronic and magnetic properties presented below.

Table 6.2: Comparison of structural parameters of $V_2O_{3-x}N_y$ in monoclinic and corundum phases with its corresponding pristine structures.

Structural parameter (Å)	Monoclinic		Corundum	
	Pristine	Doped	Pristine	Doped
d_{V-V}	2.82	2.70	2.61	2.51
d_{V-O}	1.97	2.07	2.05	2.00
d_{V-N}	–	1.91, 1.98	–	1.90, 1.95

6.3.4 Effect of N-substitution on electronic properties of V_2O_3

We now examine the effects of anion substitution on the electronic structure of V_2O_3. For r-$V_2O_{3-x}N_y$, the system still remains metallic, the N(2p) levels lie below the Fermi level around ∼-3 eV and we see a dip in electronic density of states at the Fermi level, contributing to its enhanced stability [Figure 6.4b]. In m-$V_2O_{3-x}N_y$, though a sub-band of $2p$ states of trivalent anion (N) associated with its strong bond with the cation (V) appears at the top of $2p$ states of O, it still lies below the sub-band of $3d$ states of V, revealing that the band gap is between the split d-orbitals [Figure 6.4a]. However, we see a significant change in band gap ($E_g^{m-V_2O_{3-x}N_y}$ = 0.83 eV) as a result of strong hybridization of N($2p$) orbitals with the V($3d$) orbitals, evident from its relatively narrow band of N(2p) states. N-substitution accompanying oxygen vacancy in m-V_2O_3 leads to a localized magnetic moment of -1 μB/N on vanadium atoms that would be bonded to the vacant site (shown by a pseudo light blue atom) [Figure 6.5]. Though the absolute magnetic moment remains same, the analysis of Löwdin charges reveals that the population of the spin-down electrons on V atoms in the vicinity of oxygen vacancies is relatively

higher than that of the spin-up electrons leading to an overall magnetic moment of -1 μB/N.

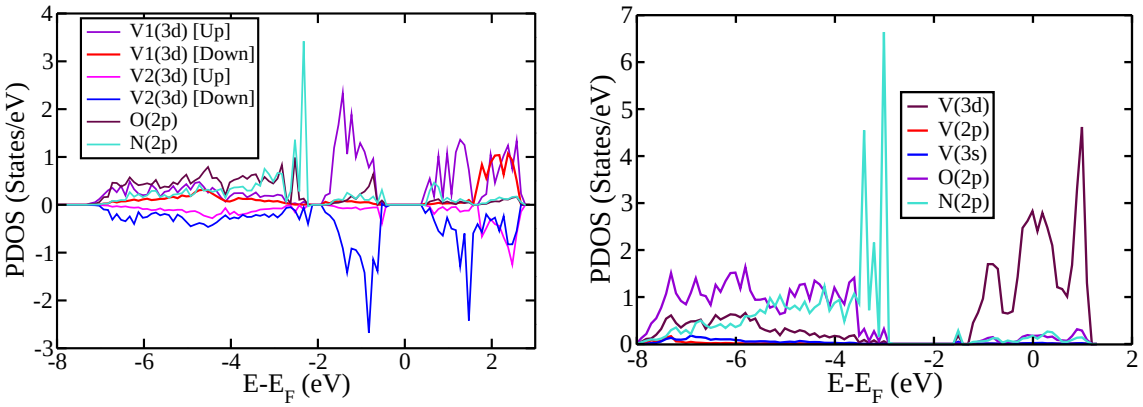

(a) (b)

Figure 6.4: Projected density of electronic states of $V_2O_{3-x}N_y$ in monoclinic (a) and corundum (b) phases. Copyright (2015) by John Wiley & Sons, Inc.

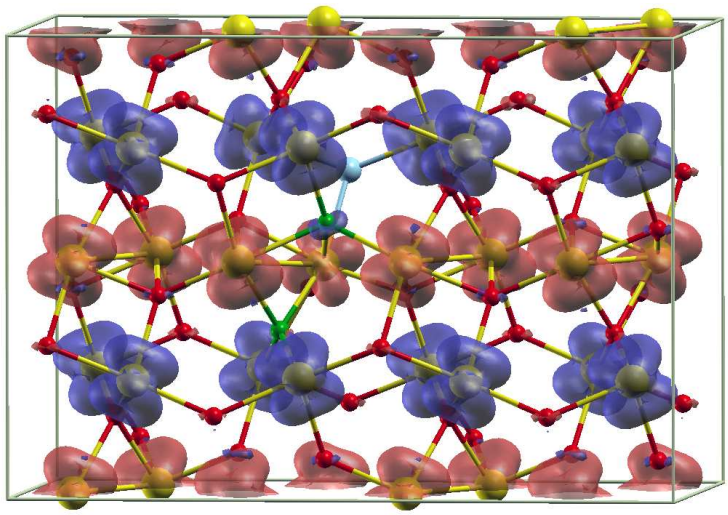

Figure 6.5: Visualization of spin-density of m-$V_2O_{3-x}N_y$ showing localized magnetic moments on vanadium atoms in the vicinity of O-vacancies (represented by a pseudo light blue atom). Copyright (2015) by John Wiley & Sons, Inc.

6.4 Conclusion

Our first-principles density functional theory-based calculations on anionic (N) substituted V_2O_3 reveals that N substitution in V_2O_3 (i) must be accompanied by introduction of oxygen vacancies, and (ii) makes the high temperature metallic corundum phase lower in energy, leading to the observed reduction in Nèel temperature. This is also indicated in the electronic structure of r-$V_2O_{3-x}N_y$, where we see a dip in electronic density of states at the Fermi level and wider sub-band of N($2p$) states. In the monoclinic phase (m-$V_2O_{3-x}N_y$) too, N($2p$) sub-band states of less electronegative atom lies above the O($2p$) states, but below V($3d$) states. However, the hybridization between N($2p$) with d-states of V results in reduction of d-d gap and a local magnetic moment of -1 μB/N on V atoms bonded to the N sites and in the vicinity of O-vacancies.

Part III

Materials for Energy Conversion

Chapter 7

Effect of aliovalent anionic co-substitution on electronic properties of CdS and ZnS*

7.1 Introduction

It is customary to substitute metal ions in oxides, sulfides and other inorganic materials to bring about changes in their structure and properties [184–187]. However, substitution of anions in these materials would be expected to bring about more significant changes in the electronic and optical properties. Thus, substitution of oxygen in colorless ZnO and TiO_2 by nitrogen changes the optical spectra giving rise to absorption in the visible region [154, 188–190]. Nitrogen substitution in oxides gives rise to oxygen vacancies and this is prevented by co-substitution of N and F in oxides [154, 190–192]. Such co-substitution changes the optical properties of ZnO and TiO_2 markedly rendering them orange and yellow colored, respectively, thereby reducing the band-gap of the oxides markedly. Accordingly, N, F co-substituted

*This work has been published in part in *Angew. Chem. Int. Ed* [183]. Copyright (2015) by John Wiley & Sons, Inc., URL: http://dx.doi.org/10.1002/anie.201501532

ZnO and TiO_2 prepared recently show that the oxides exhibit visible-light induced reactivities [154, 190–194]. In the light of the reports on the marked effects of co-substitution of N, F in oxides, it seemed important to explore how substituting the sulfide ion in metal sulfides by P, Cl and N, F change the electronic properties. Such co-substitution by P and Cl in CdS and ZnS would be of great value in view of the highly desirable attributes of these important semiconductors. We have investigated the effects of anionic co-substitution in CdS and ZnS. We also determine the role of the crystal structure of the host lattice in tuning the electronic properties of co-substituted CdS and ZnS.

7.2 Computational Details

Our calculations are based on first-principles density functional theory (DFT) as implemented in QUANTUM ESPRESSO package [45], with interaction between ionic cores and valence electrons represented using ultrasoft pseudopotentials [47]. We use two flavors of exchange-correlation energy functionals (a) generalized gradient approximation (GGA) of Perdew Burke-Ernzehof (PBE) and (b) local density approximation (LDA) of Perdew-Zunger (PZ) parameterized form respectively [42, 44]. We employ plane wave basis truncated with energy cutoffs of 30 Ry and of 180 Ry in the representation of wave functions and charge density respectively. Within periodic boundary conditions, suitable supercells of CdS and ZnS are used to model desired concentration of anion dopant's. We use uniform mesh of 12 x 12 x 9 and 12 x 12 x 12 k-points in sampling integrations over Brillouin zone of hexagonal and cubic structures respectively, and smear the discontinuity in the occupation numbers of electronic states using the Fermi-Dirac distribution with smearing width (k_BT) of 0.04 eV. We relax the structure to minimize energy until the Hellman-Feynman forces are less than 0.03 eV/Å in magnitude. Phonons and Born effective charges are

determined as the second derivatives of energy using density functional perturbation theory (DFPT).

7.3 Results and Discussion

7.3.1 Properties of pristine CdS

Crystalline CdS occurs in cubic (c-CdS) and hexagonal wurtzite (h-CdS) structures belonging to F43m (T_d^2) and $P6_3mc$ (C_{6v}^4) space groups respectively. The wurtzite phase of CdS (h-CdS) is found to be relatively more stable than c-CdS (ΔE= 2 meV) in our calculations. Our estimates of its lattice constant obtained within GGA and LDA are within the typical DFT errors [Table 7.1] [195]. To benchmark our results further, we have analyzed the electronic and vibrational spectra of bulk h-CdS. We find electronic structures obtained within LDA and GGA are quite similar, and h-CdS exhibits a direct band gap of $\sim$1.1 eV. It is noted that band gaps are typically underestimated in LDA or GGA based DFT. An improved estimate of band gap using HSE functionals is 2.35 eV, in good agreement with an experimental value of 2.5 eV [196]. From the projected density of states (PDOS), we find that the energy bands immediately below the gap are constituted of *p*-orbitals of S, and valence bands deeper in energy arise from the *d*-orbitals ($\sim$-8.5 to -7.5 eV) of Cd. Conduction bands (just above the gap) are primarily contributed by *s*-orbitals of Cd, while the bands around 2$-$3 eV arise from *p*-orbitals of Cd [Figure 7.1a]. Phonon spectrum of CdS confirms that the local structural stability of h-CdS [Figure 7.1b]. Analysis of phonons at the zone center (Γ-point) reveal that h-CdS has 3 IR-active modes with frequencies, ω = 212, 220, 220 cm^{-1}'s, visualization of their eigen displacements reveals that all Cd and S atoms move in opposite direction.

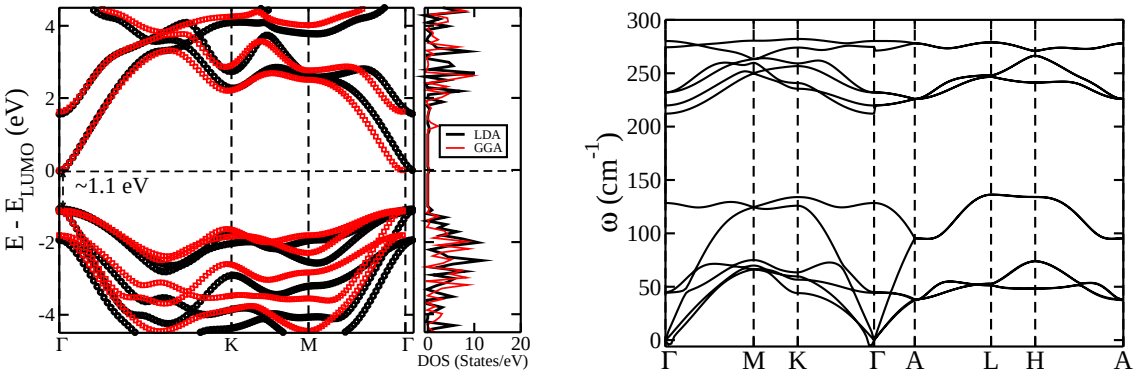

(a) (b)

Figure 7.1: Electronic band structure and density of states within GGA and LDA (a) and phonon dispersion within GGA (b) of h-CdS determined from first-principles. Copyright (2015) by John Wiley & Sons, Inc.

Table 7.1: Comparison of calculated lattice parameters and electronic band gap of h-CdS with experimental results.

	GGA	LDA	Experiment [195, 196]
a (Å)	4.197	4.05	4.14
$\frac{c}{a}$	1.626	1.629	1.623
d_{Cd-S}(Å)	2.57	2.48	2.54
E_g (eV)	1.11	1.05	2.5

7.3.2 Anion substitution in h-CdS

We consider three different kinds of anionic substitution in h-CdS: (i) A (= P, N) substituted CdS (h-$CdS_{1-x}A_x$), (ii) B (= Cl, F) substituted CdS (h-$CdS_{1-x}B_x$), and (iii) A, B co-substituted CdS (h-$CdS_{1-x-y}A_xB_y$). We have consider a 2 x 1 x 1 periodic supercell containing 16 atoms: Cd_8S_8 with substitution of (a) one of the sulphur atom with A amounting to 6.25%, (b) one of the sulphur atom with B (6.25%), and (c) two of the sulphur atoms with A and B (12.5%). In case of individual substitution of p-type or n-type atom at 6.25%, we have only one inequivalent configuration [197]. For co-substitution, there are many possible

configurations corresponding to different ordering of A and B type atoms. We employ the site occupancy disorder technique (SOD) which uses symmetry of the crystal to determine the inequivalent configurations [197]. We find 3 inequivalent configurations: A, B atoms present in different atomic plane bonded to same Cd atom (I), A, B atoms present in same atomic plane bonded to same Cd atom (II) and A, B atoms bonded to different Cd atoms (III) [Figure 7.2]. From their energies, we find that the configuration with A and B atoms occupying site bonding to the same Cd atom but present in different plane is the most stable one [see Table 7.2].

Table 7.2: Comparison of energetics for different configurations of h-Cd_8S_6AB.

Configuration (n)	$\Delta E = E_n\text{-}E_{Stable}$(eV)	
	h-Cd_8S_6PCl	h-Cd_8S_6NF
I	0	0
II	0.01	0.09
III	0.16	0.25

We first consider P and Cl for p-type and n-type doping respectively. The change in the lattice parameters upon substitution with phosphorus and chlorine for sulphur is small (within $\sim$ 1 - 2%). On the other hand, there are pronounced local structural distortions in the vicinity of the substitutional sites in the co-substituted CdS. The energetics of h-Cd_8S_7P, h-Cd_8S_7Cl and h-Cd_8S_6PCl reveal that (a) co-substitution with P and Cl is preferred over individual dopant substitutions with a lowering of energy by E_C=-1.94 eV per (P, Cl) pair, where E_C defines its relative stability:

$$E_C = E_{h-CdS_{1-x-y}A_xB_y} + E_{h-CdS} - E_{h-CdS_{1-x}A_x} - E_{h-CdS_{1-y}B_y} \tag{7.1}$$

where, E_α (with α = h-$CdS_{1-x-y}A_xB_y$, h-CdS, h-$CdS_{1-x}A_x$ and h-$CdS_{1-y}B_y$) represents the total energy of the corresponding complex. It is the relative energy of bulk CdS and co-substituted CdS with respect to individually anion substituted CdS. For

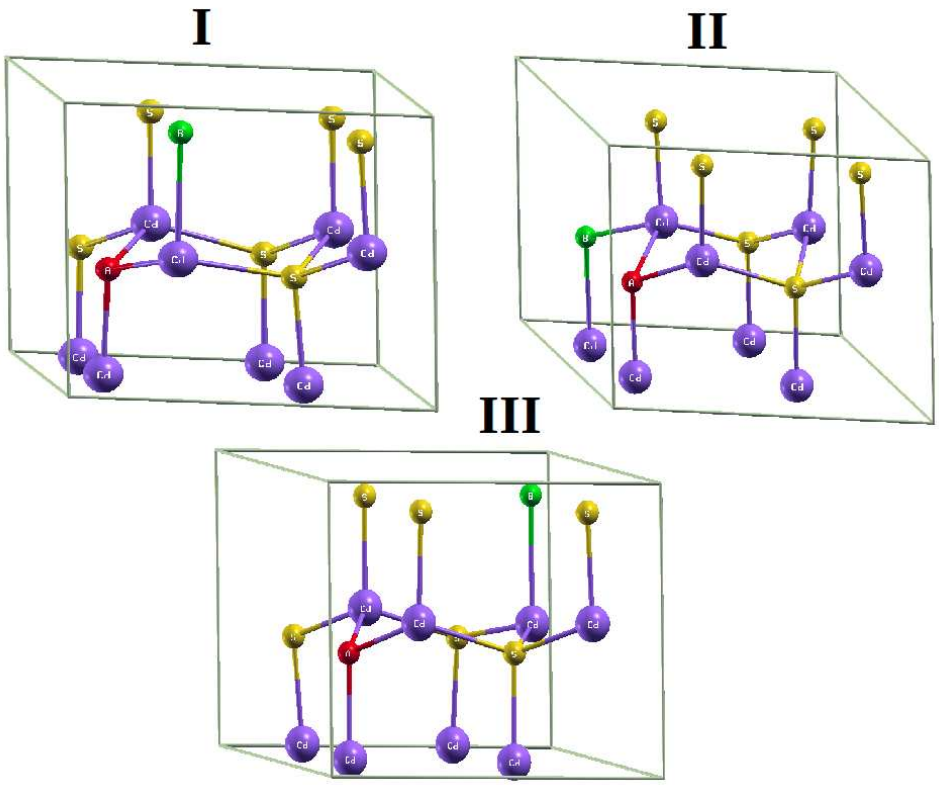

Figure 7.2: Different possible inequivalent configurations of h-Cd_8S_6AB. Copyright (2015) by John Wiley & Sons, Inc.

example, its negative value implies that co-substitution of P and Cl is energetically more favorable to P and Cl separately substituted in CdS. From bond valence analysis, Cd-P and Cd-Cl bond lengths are 2.49 Å and 2.98 Å respectively in Cd_8S_6PCl. Notably, these are 3% shorter and 9% longer respectively than the Cd-S bonds (2.57 Å) of bulk h-CdS, leading to a decrease in effective coordination number of Cd bonded with P and Cl in h-Cd_8S_6PCl to 3.31. These bond lengths are 4.2% shorter and 11.6% longer than average bond lengths of Cd-P (2.6 Å) and Cd-Cl (2.67 Å) respectively in other Cd-P and Cd-Cl compounds reported in literature [198, 199].

Electronic structure of h-Cd_8S_6PCl shows an isolated occupied band split from the rest of the valence bands [Figure 7.3a], leading to a drastic decrease in band gap (ΔE_g=0.58 eV, $E_g^{h-Cd_8S_6PCl}$=0.53 eV). To understand the nature of this isolated sub-band at the top of the valence band, we analyzed the density of electronic states

of h-Cd_8S_6PCl by projecting them onto atomic orbitals and compared with bulk h-CdS. In bulk h-CdS, the valence band is constituted primarily of p-orbitals of S with a little mixing of d-orbitals of Cd. The uppermost valence band is most affected by phosphorus $3p$ states emerging as a sub-band with bandwidth of about 0.64 eV [Figure 7.3b] in the gap. Our analysis of the density of electronic states of h-Cd_8S_7P, h-Cd_8S_7Cl and h-Cd_8S_6PCl reveals that (a) $3p$ states of strongly electronegative Cl atoms are deep lying in energy ($\sim$ -5–-2 eV) while those of the less electronegative P are concentrated at the top of the valence band, and (b) isolation of the sub-band of $3p$ states of P atom (in h-$CdS_{1-x-y}P_xCl_y$) from the rest of valence band becomes even more prominent on co-substitution with chlorine. The lowest energy conduction bands are essentially unaffected by P, Cl co-substitution and retain their Cd($3s$) character.

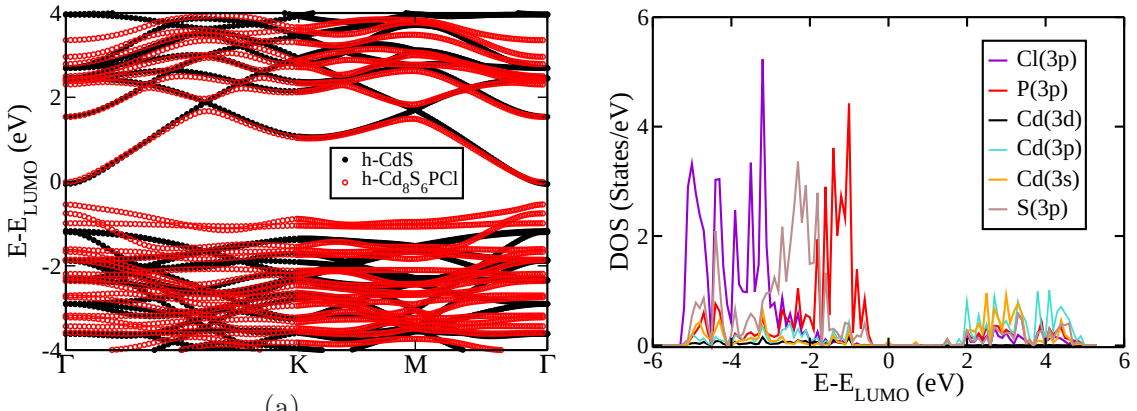

(a) (b)

Figure 7.3: Electronic structure (a) and projected density of states (b) of h-Cd_8S_6PCl clearly reveal an isolated band emerging from $3p$ orbitals of P at the top of valence band. Copyright (2015) by John Wiley & Sons, Inc.

The Born effective charge (BEC, $Z^*_{\alpha\beta}$) tensor is defined as the derivative of polarization P with respect to atomic displacement.

$$Z^*_{i\alpha\beta} = \Omega \frac{\partial P_\alpha}{\partial u_{i\beta}} \tag{7.2}$$

where i indexes an atom, α, β are Cartesian indices and Ω is the volume of the unit cell. Z^* gives the coupling between the electric field (e.g., IR radiation) and the ionic lattice. It reveals the nature of bonding in the system. The BECs of Cd ($Z^*_{xx,yy}$=2.23, Z^*_{zz}=2.33) and S ($Z^*_{xx,yy}$=−2.27, Z^*_{zz}=−2.35) are very close to its nominal ionic charges of +2 and -2 respectively indicating ionic nature in h-CdS. In h-Cd_8S_6PCl, the BECs of P are (Z^*_{xx}=−1.83, Z^*_{yy}=−1.73, Z^*_{zz}=−1.63), while those of Cl are (Z^*_{xx}=−1.82, Z^*_{yy}=−1.91Z^*_{zz}=−1.91). The anomaly in the BEC tensor of P is stronger compared to Cl, clearly showing a relatively high chemical activity of P and relative inertness of Cl and confirms the mixed ionic-covalent and largely ionic nature of Cd-P and Cd-Cl bonds respectively. Our calculations show an increase by 10−30% in the electronic dielectric constant (ε^∞), another effect of the reduction in the electronic band gap on properties [see Table 7.3].

Table 7.3: Comparison of electronic band gaps and electronic dielectric constant (ε^∞)of Cd_8S_6AB with pristine CdS in different crystal structures.

System	Hexagonal				Cubic
	E_g (eV)	ε^∞_{xx}	ε^∞_{yy}	ε^∞_{zz}	E_g (eV)
Pristine	1.11	7.12	7.12	7.28	1.00
Cd_8S_6PCl	0.53	7.91	8.99	7.17	0.97
Cd_8S_6NF	0.53	8.04	9.80	6.64	0.67

To study the effect of substitution of other anions on structural and electronic properties of h-CdS, we consider co-substituted h-CdS with (N, F) pair at the same doping concentration. Here too, we find that co-substitution is preferred over the individual dopant substitutions with lowering of energy by 2.34 eV per (N, F). The local structural distortions are even more pronounced in these complexes i.e, Cd-N is 2.15 Å and Cd-F is 4.16 Å, with slight weakening of Cd-S bond (2.64 Å), leading to a drastic reduction in ECN of Cd bonded with (N, F) pair to 1.98. This is expected from relatively smaller size of N and F anions than that of S.

Electronic structure reveals a similar change in the band gap, i.e, $E_g^{h-Cd_8S_6NF} = 0.53$ eV [Table 7.3]. Similar to h-Cd_8S_6PCl, the isolated band arises from $2p$-orbitals of less electronegative element (N) and the bands arising from more electronegative element (F) is much deeper in energy.

7.3.3 Role of crystal structure

We now determine how the crystal structure influences the effects of anion substitution on the electronic properties of CdS, and consider the cubic zinc-blend structure of CdS (c-CdS). Our estimate of the lattice parameter obtained with GGA is a = 5.93 Å and is in good agreement with the experimental value of 5.82 Å [200]. The calculated band gap of pristine c-CdS is 1.00 eV, slightly lower than that of its hexagonal form (E_g^{GGA}(hex) = 1.11 eV). We find that 12.5% co-substitution of (P, Cl) and (N, F) pair for S in c-CdS leads to changes in the lattice parameters of about 1-2% and the ECN is similar to that in the co-substituted h-CdS. Analysis of the projected density of states reveals that the orbital contributions to HOMO and LUMO are similar to what we find in co-substituted h-CdS. However, we find that change in band gap due P, Cl co-substitution (c-Cd_8S_6PCl) is negligible (ΔE_g=−0.03 eV), as compared to c-Cd_8S_6NF (ΔE_g=−0.33 eV) which is relatively weaker compared to h-Cd_8S_6AB for different *A, B* pair [Figure 7.4, Table 7.3]. This reveals that structure of CdS plays quite an important role in tunability of its electronic structure with anionic substitution.

7.3.4 Hexagonal and cubic ZnS

We now determine the effects of anionic co-substitution in ZnS, which also exists in cubic and hexagonal structures. Our estimates of lattice constant for pristine ZnS are a_{cubic}^{GGA}=5.45 Å and $a_{hexagonal}^{GGA}$=3.85 Å , $c_{hexagonal}^{GGA}$=6.302 Å and are found in good

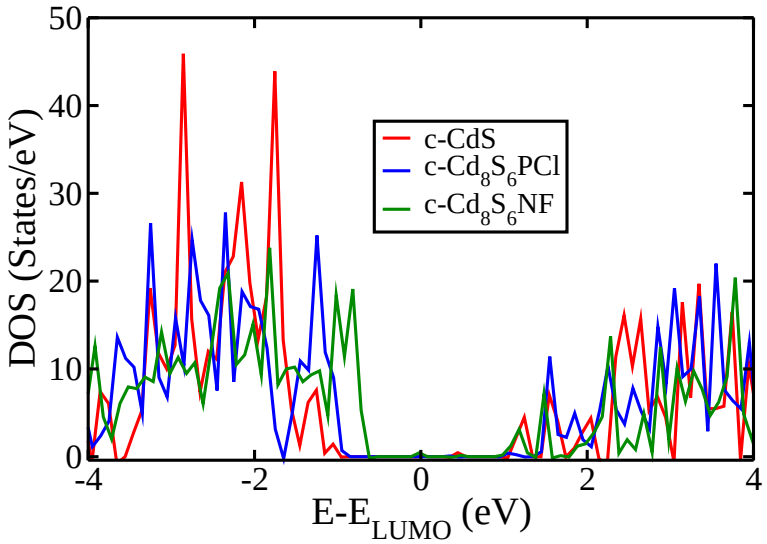

Figure 7.4: Comparison of density of states of c-Cd_8S_6AB with pristine c-CdS. Copyright (2015) by John Wiley & Sons, Inc.

agreement with experiment [201]. The calculated band gap of cubic and hexagonal phase of pristine ZnS are 2 and 2.07 eV, respectively. We consider co-substitution of (P, Cl) and (N, F) pair for S in ZnS at the doping concentration of 12.5%. On anionic co-substitution, changes in the lattice parameters of both crystal structures are similar to their CdS counterpart. Analysis of the projected density of states reveals that the orbital contributions to HOMO and LUMO are similar to what we find in cubic and hexagonal Cd_8S_6AB, and Zn playing a role very similar to Cd. The changes in band gap of hexagonal and cubic phases are similar to the Cd_8S_6AB compounds, except that $E_g^{h-Zn_8S_6NF} > E_g^{h-Zn_8S_6PCl}$ [Figure 7.5, Table 7.4]. Closer structural analysis reveal that though N and F prefer to be bonded to the same Cd atom, F is too weakly bonded to Zn (d_{Cd-F} = 3.46 Å) to affect the N states in Zn_8S_6NF, leading to relatively narrow isolated sub-band. This confirms that both the crystal structure and nature of anions are relevant to tunability of electronic structure of CdS or ZnS.

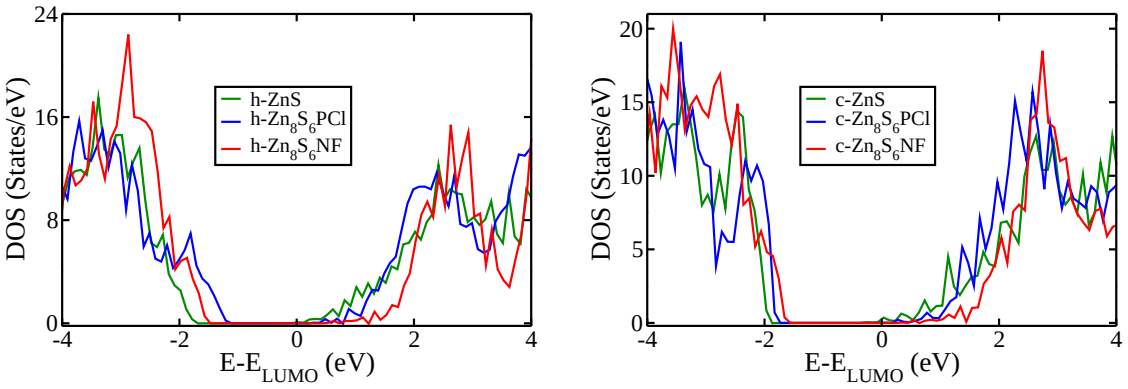

(a) (b)

Figure 7.5: Comparison of density of states of Zn_8S_6AB with pristine ZnS for (a) hexagonal and (b) cubic crystal structures. Copyright (2015) by John Wiley & Sons, Inc.

Table 7.4: Comparison of band gaps of Zn_8S_6AB with pristine ZnS in different crystal structures.

System	E_g(eV)	
	Hexagonal	Cubic
Pristine	2.00	2.07
Zn_8S_6PCl	1.33	1.88
Zn_8S_6NF	1.47	1.62

7.3.5 Experimental studies

Our theoretical findings has helped in designing the experiments. Kouser et al.[†] , were successful in doping P, Cl and N, F in both CdS and ZnS experimentally. They have observed similar shifts in the band gap. The preliminary studies of photocatalytic hydrogen generation using $CdS_{1-x-y}P_xCl_y$ showed an enhancement of hydrogen evolution activity by 300% compared to CdS.

[†]S. Kouser, S. R. Lingampalli, P. Chithaiah, A. Roy, S. Saha, U. V. Waghmare and C. N. R. Rao, *Angew. Chem. Int. Ed.*, doi: 10.1002/anie.201501532, 2015.

7.4 Conclusion

We find that CdS and ZnS become p and n-type semiconducting with substitution of A (=P or N) and B (=F or Cl) respectively. Anionic co-substitution is energetically preferred over the individual substitution by more than 1.5 eV/atom, and A, B atoms preferentially occupy the sites bonding to the same cation (Cd or Zn) atom in the lowest energy configuration. The reduction in band gap in co-substituted CdS/ZnS is due to the emergence of an isolated sub-band at the top of valence band, which is primarily contributed by the trivalent, less electronegative anions like P and N. Bands of more electronegative anions (Cl and F) lie deep in energy below the valence band.

We find that changes in the electronic band gap are more pronounced in hexagonal crystal structure for anion co-substituted CdS and ZnS. For cubic crystal structure, change in band gap of N, F co-substituted CdS or ZnS is larger than that of P, Cl co-substituted CdS or ZnS, indicating that the effects of anion co-substitution on the electronic structure are quite sensitive to the host lattice structure, specific host compound and nature of dopants. Our findings have given significant input to the experiments and helped in designing the experiments.

Chapter 8

Two-dimensional GaS*

8.1 Introduction

The present crisis due to dwindling energy resources and production of harmful gases upon combustion of nonrenewable fossil fuels requires solutions that tackle issues of energy and environment in an integrated manner. Renewable sources of energy are often directly or indirectly dependent on sunlight. Hydrogen produced from water using solar energy is a good option for the medium of clean renewable energy. Traditionally, H_2 is generated from water using catalysts in different chemical processes such as electrocatalysis, photocatalytic, or photoelectrocatalytic production of hydrogen [21]. Maeda and Domen [22] reported that more than ten thousand photocatalytic water splitting systems with energy conversion efficiency above 10% need to be established to meet one-third of the energy requirement of human beings by 2050 through photocatalytic production.

For the electrochemical decomposition of water, potential difference between the anode and cathode needs to be 1.23 eV. This potential difference is slightly less than the energy of visible radiation. Therefore, a suitable photocatalyst must have its

*This work has been published in part in *Small*, 2015 (in press). Copyright (2015) by John Wiley & Sons, Inc., URL: http://dx.doi.org/10.1002/smll.201501077.

electronic band positions that straddle the redox potentials, i.e., hydrogen evolution reaction (HER) and oxygen evolution reaction (OER) and a gap less than ≈1.6 eV to efficiently use solar energy and split H_2O to H_2 [23].

Efficient photocatalysts for water splitting include metal oxides, such as $SrTiO_3$, TiO_2, and $NaTaO_3$ [24–28]. These materials have suitable band structure, and are very stable during the photocatalytic process. However, most of them are active only under UV light, which only accounts for ≈4% of the energy of solar spectrum. So far, few efforts have focused on the development of sulfide-based photocatalysts for hydrogen production [29]. Sulfides, e.g., CdS typically possess relatively high conduction band positions suitable for H_2O reduction and exhibit better sunlight response than oxides, which originates from (a) the higher valence band positions composed of S $3p$ orbitals and conduction band positions negative enough to reduce H_2O to H_2, and (b) narrow band gaps with better response to the solar spectrum [30–32].

Among chalcogenides, layered transition metal sulfide or selenide such as MoS_2, $MoSe_2$, and TaS_2 have been found effective in catalyzing solar water splitting [32–35]. Zhuang and Hennig have theoretically predicted that the monolayer of group III monochalcogenides have ideal band edges for overall water splitting [36]. Monolayer GaS involves mixed covalent and ionic bonding exhibiting a moderate indirect band gap. With a similar direct band gap, it has the potential for use as a photocatalyst. Unfortunately, monolayer GaS has not been synthesized so far experimentally, while its bulk and nanoscale 2D forms have been synthesized using simple methods like single-zone heating furnace and mechanical cleavage, respectively [202, 203]. We use comparison of results of our calculations on monolayer GaS with the work of Zhuang and Hennig [36] as a benchmark.

As the band gap of monolayer GaS is little high for efficient use of visible light, it is desirable to tune the band gap to improve the solar response. The properties of 2D

materials can be modified by nanopatterning and chemical treatment, an application of external electric field or strain engineering [204–207]. However, nanopatterning and chemical treatment damage and induce disorders, which can deteriorate the performance of the devices. Recently, strain engineering was identified as one of the best possible strategies to tune the band gap in graphene and few TMD's [205, 206]. Ma *et al.* [208] has shown that monolayer GaS is very sensitive to mechanical strains, however they have explored only the response of a system to tensile strains. Here, we study the response of monolayer GaS to compressive strains and also demonstrate semiconductor-to-metal (S-M) transition.

In this chapter, we present a thorough analysis on the structural and electronic properties of different thickness of GaS (monolayer, multilayer, and bulk) using first-principles calculations based on density functional theory (DFT). We examine its band edge energies on the standard hydrogen electrode (SHE) potential scale, and discuss their relevance to water splitting in terms of the redox potentials of water. We extend these with theoretical studies of adsorption of water on GaS and predict that it is suitable for photocatalysis of water splitting. We have studied the response of monolayer GaS to compressive strains and compare with its response to tensile strains. We demonstrate semiconductor-to-metal phase transition on the application of biaxial strains and determine the stability of the system at these strains.

8.2 Computational Details

The first-principles calculations were based on the DFT as implemented in Quantum ESPRESSO package [45]. Exchange-correlation energy functionals were used with a local density approximation (LDA) functional of Perdew-Zunger (PZ) and generalized gradient approximation (GGA) functional of Perdew-Burke-Ernzenhof

(PBE) parameterized form with the Grimme term to capture van der Waals interaction [42, 44, 49]. Since the band gaps were typically underestimated in DFT, HSE hybrid functionals were used to calculate the band gaps accurately. Kohn-Sham wave functions were represented using a plane wave basis with an energy cutoff of 50 Ry and charge density was represented with basis truncated at cutoff of 400 Ry, and the interactions between ionic cores and valence electrons were represented using ultrasoft pseudopotentials (USPP) for GGA [47]. A uniform mesh of 15 x 15 x 1 K-points was employed in sampling integrations over the Brillouin zone [209]. A vacuum of 17 Å was used perpendicular to the sheet to keep the interactions between the periodic images weak. The structure was relaxed to minimize the total energy until the Hellmann-Feynman force on each atom was less than 0.03 eV $Å^{-1}$. The phonon dispersion was obtained on a finer q-mesh, i.e., 5 x 5 x 1 using density functional perturbation theory enforcing acoustic sum rule for q $\rightarrow$ 0.

8.3 Results and Discussion

8.3.1 Structural and vibrational analysis

GaS has a hexagonal layered structure belonging to P$\bar{6}$m2 space group (No. 187), with each layer consisting of S-Ga-Ga-S atomic planes stacked along c-axis. We first consider here a single layer of GaS [Figure 8.1a]. Our estimate of its lattice constant using GGA (a^{GGA} = 3.59 Å) is in good agreement with the experimental lattice parameter of monolayer GaS (i.e., a^{exp} = 3.585 Å), while it is significantly underestimated using LDA (a^{LDA} = 3.45 Å). The Ga-Ga and Ga-S bond lengths are overestimated by ≈1% using GGA and underestimated by ≈5% using LDA with respect to the experimental values [203, 210]. A detail comparison of structural parameters using different correlation functionals is reported in Table 8.1.

Phonon dispersion, obtained with DFT linear response calculations of the second

Table 8.1: Comparison of structural parameters and band gap of monolayer GaS obtained using different exchange-correlation functionals with experimental values.

Properties	LDA	GGA	Experimental[5]
a (Å)	3.47	3.59	3.585
d_{Ga-S}(Å)	2.26	2.47	2.48
d_{S-S} (Å)	2.32	2.35	2.37
E_g (eV)	2.56	2.56	3.05

derivatives of total energy with respect to atomic positions, reveals that monolayer GaS is locally stable. The weak structural instabilities associated with flexural modes in 2-D systems are typically the artifacts of the numerical errors coming from the mesh sizes and enforcement of acoustic sum rule only at the point. In GaS, it is further demanding due its structure consisting of four atomic planes. To this end, we have done calculations with finer q-mesh (5 x 5 x 1) and imposed the acoustic sum rule for q $\rightarrow$ 0 [Figure 8.1b] to eliminate these errors. We have identified Raman spectroscopic signatures of the monolayer GaS in four Raman active modes, i.e., E^1_{1g}, A^1_{1g}, E^1_{2g} and A^2_{1g}. Our LDA estimates of frequencies of Raman modes are in slightly better agreement with experiments [202], than the GGA estimates, which are underestimated by 20 cm^{-1} [Table 8.2].

Table 8.2: Comparison of frequencies (cm^{-1}) of Raman active modes of monolayer GaS obtained using different exchange-correlation functionals with experimental values.

Symmetry Label	LDA	GGA	Experimental[5]
E^1_{1g}	64	61	-
A^1_{1g}	181	176	185
E^1_{2g}	295	280	303
A^2_{1g}	356	339	363

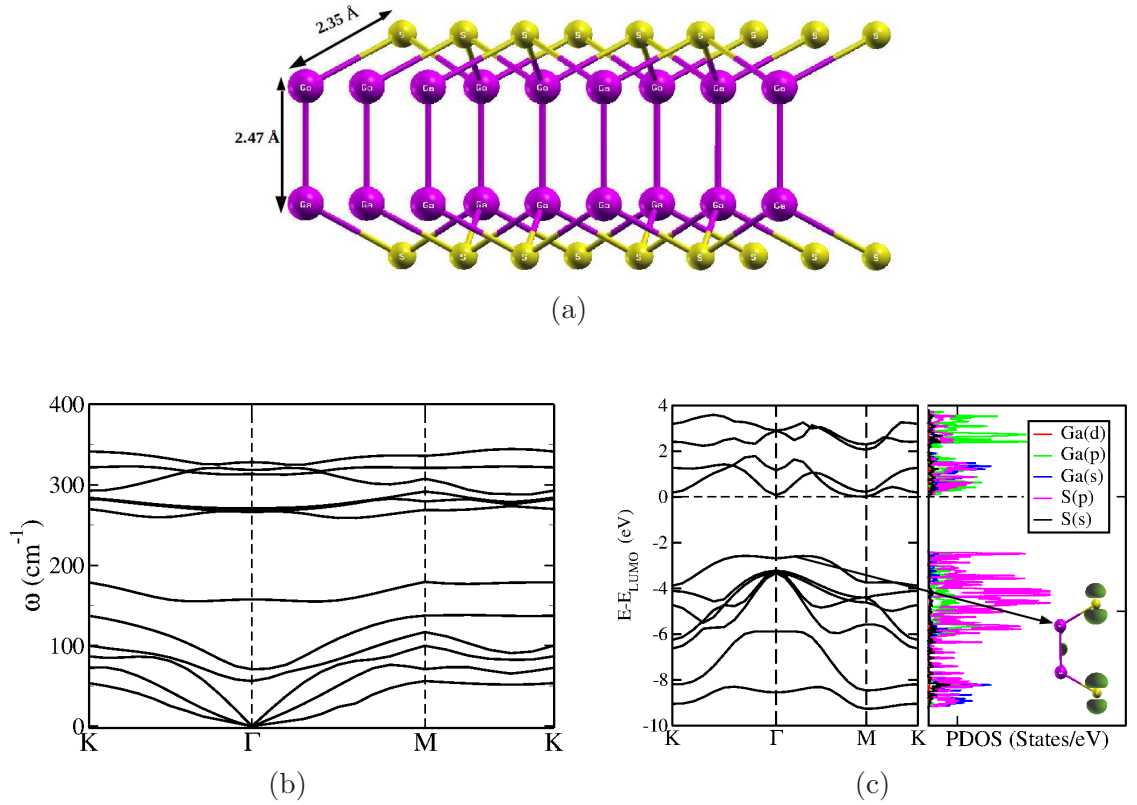

Figure 8.1: Relaxed structure (a), phonon dispersion (b), and electronic structure (c) of monolayer of GaS using GGA. Copyright (2015) by John Wiley & Sons, Inc.

8.3.2 Electronic structure analysis

From its electronic structure [Figure 8.1c], monolayered GaS is clearly a semiconductor with an indirect band gap of 2.52 eV, although the direct gap is only slightly larger (2.68 eV). We examine the projected density of states (PDOS) to study orbital contribution to valence and conduction bands. Contribution to the energy bands immediately below the gap is mainly from *p*-orbitals of S and has a weak component from *p*-orbitals of Ga [Inset Figure 8.1c]. Valence bands deeper in energy arise from *s*-orbitals of S and *d*-orbitals of Ga (≈-16 to -14 eV). Conduction bands are primarily made of *s* and *p*-orbitals of Ga. To analyze the contribution to the top most valence band, we have visualized its charge contribution and found

that it is primarily constituted from the p-orbitals of S [Inset Figure 8.1c]. As band gaps are typically underestimated in DFT, we have used Heyd-Scuseria-Ernzerhof (HSE) hybrid functional to obtain an accurate estimate of the band gap and precise positions of valence and conduction bands relative to vacuum. The HSE-based estimate of band gap is E_g^{HSE}= 3.5 eV. However, the gap is sensitive to lattice constant and hence to the DFT errors. We find a better agreement of band gap with the experiment (E_g^{exp} = 3.05 eV) using HSE functionals by fixing the lattice parameter to its experimental value (a = b = 3.58 Å) $E_g(a^{exp})$ = 3.19 eV [202].

To benchmark our results, we determine its band edge energies and align them on the SHE potential scale. Based on these, we discuss their positions relative to the redox potentials of water splitting using different exchange-correlation energy functionals. Reactivity of a catalyst is determined by its work function (ϕ), which is defined as the minimum amount of the work done required to remove an electron from the interior of a solid to vacuum and is given by

$$\phi = E_{vac} - E_F. \tag{8.1}$$

Since the density of electronic states at Fermi energy (E_F) is nonzero only for metals, we consider ϕ of a p-type semiconducting GaS as

$$\phi = E_{vac} - E_{VBM} \tag{8.2}$$

where E_{VBM} is the energy of valence band maxima. From the macroscopic planar average of electronic potential of monolayer GaS obtained as a function of z (perpendicular to its plane), we determine the vacuum level, and estimate ϕ = 6.23 and 6.33 eV with GGA and LDA, respectively, and 6.72 eV by using hybrid functional (HSE) (at a^{exp} =3.585 Å) [Figure 8.2a]. These are comparable to the work function of other Ga^{2+} compounds and that of CdS (7.12 eV), indicating that GaS may have

a better catalytic activity than CdS [211]. From the valence and conduction bands aligned on SHE scale, we find that the redox potentials of H_2O splitting are properly straddled by the valence and conduction bands suggesting monolayered GaS does hold some promise for use as a photocatalyst for water splitting [Figure 8.2b].

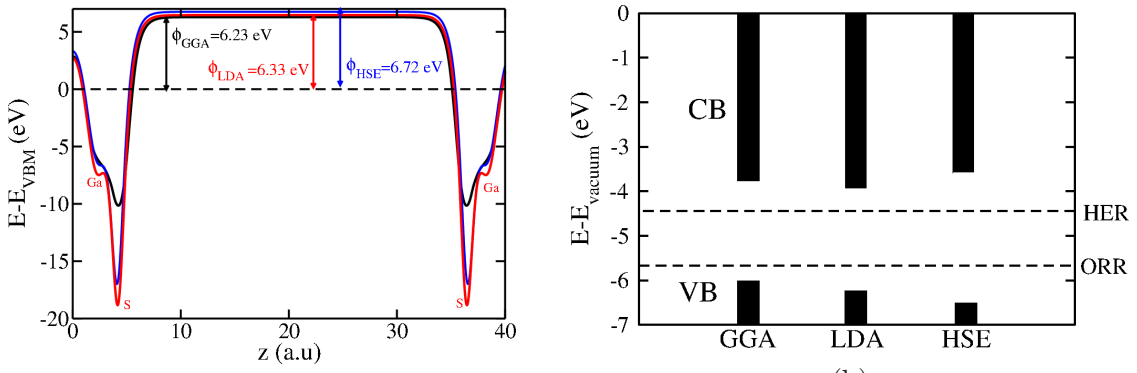

Figure 8.2: Work function (a), and band alignment (b) of monolayer GaS using GGA and HSE functionals. Copyright (2015) by John Wiley & Sons, Inc.

8.3.3 Adsorption studies

To verify the potential of monolayered GaS as a photocatalyst, we have simulated adsorption of H_2O molecules at various coverages of water molecules on the surface of 2D-GaS. All the coverages are calculated by considering only top two atomic layers of monolayer GaS. Water molecules were initially placed at a distance of 1.4 Å from GaS. At a coverage of 24.3 mmol g^{-1}, H_2O molecules drift away from the substrate. To quantify the strength of interaction between H_2O and 2D-GaS, we obtain adsorption energy (E_A)

$$E_A = \frac{E_{complex} - E_{substrate} - nE_{H_2O}}{n} \tag{8.3}$$

where $E_{complex}$, $E_{substrate}$, and E_{H_2O} are the total energies of the optimized structures of the H_2O-substrate complex, GaS substrate, and an isolated H_2O molecule, respectively, and n is the total number of H_2O molecules. We find moderate adsorption energy of about -46.3 kJ mol^{-1} of H_2O. To understand the mechanism of adsorption, we determine the energy of interaction between the H_2O molecules in the complex by freezing them in their adsorbed positions and removing the substrate. The interaction energy of H_2O molecules $E_{int}^{H_2O}$ is calculated with

$$E_{int}^{H_2O} = \frac{E_{n.H_2O} - nE_{H_2O}}{n} \tag{8.4}$$

where $E_{n.H_2O}$ and E_{H_2O} are the total energies of n frozen H_2O molecules without substrate and an isolated H_2O molecule respectively. We find that $E_{int}^{H_2O}$ is -45.8 kJ/mol indicating that the adsorption energy is largely due to the intermolecular interaction of H_2O molecules. Thus, the interaction between an infinite 2D-GaS and H_2O is rather weak.

To study this interaction in the presence of GaS edges, we have considered a 2 x 3 supercell of monolayered GaS with periodicity along one direction (nanoribbon) and different coverages of H_2O (2.7-16.2 mmol g^{-1}, i.e., $n = 1-6$ per 2 x 3 supercell). At a low coverage (i.e., 2.7 mmol g^{-1}), we find weak interaction (E_A = -10.8 kJ mol^{-1}) between H_2O molecule and the substrate purely due to van der Waals forces. As the concentration increases, adsorption energy increases and becomes positive for higher concentration (16.2 mmol g^{-1}), where H_2O dissociates to give H_2 [Figure 8.3a]. In the initial structure used in structural relaxation, H_2O molecules were placed at a distance of 1.4 Å from the S atomic plane of GaS. After relaxation, it led to the splitting of water and chemisorption of the released oxygen through the formation of Ga-O-S bonds [Figure 8.3a]. We note that H_2O cannot be split into H_2 without absorption of photons, it is clearly reflected in the positive cost of energy required

for the splitting of H_2O into H_2 (189 kJ mol^{-1}), which is sourced externally through absorption of light or an application of electric field.

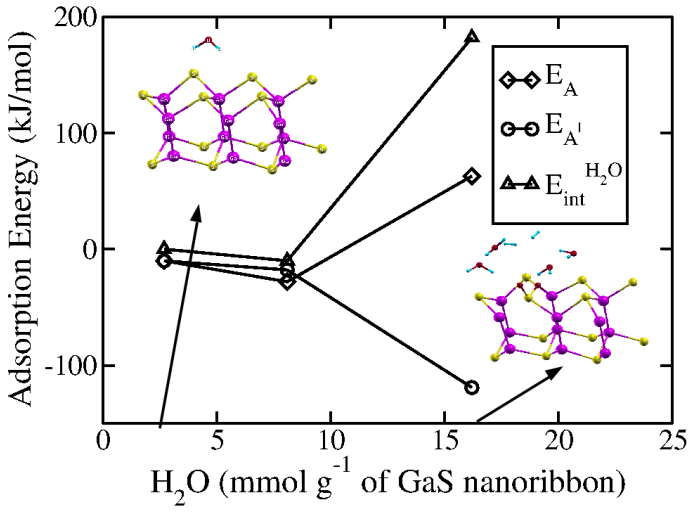

(a)

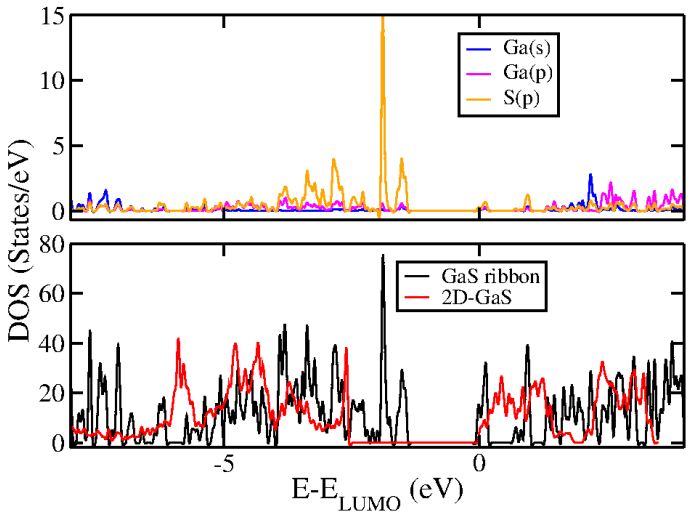

(b)

Figure 8.3: Adsorption energy as a function of different coverage of water molecules on GaS nanoribbon (a), comparison of density of states for 2D-GaS and GaS nanoribbon (b). Copyright (2015) by John Wiley & Sons, Inc.

To understand such anomalous adsorptive behavior, we have separated intermolecular interaction energy from that of the H_2O molecules with substrate (E'_A)

and H_2O molecules themselves ($E_{int}^{H_2O}$), where E'_A is calculated as

$$E'_A = E_A - E_{int}^{H_2O} \tag{8.5}$$

We see that the positive value of adsorption energy is due to dissociation of H_2O molecules ($E_{int}^{H_2O}$ = 181.9 kJ/mol). At relatively lower concentrations of adsorption on GaS nanoribbons than that considered for infinite sheet, we see that H_2O molecules split to give H_2 indicating that the presence of edges may activate the surface sites. To understand the role of edges, we examine the electronic density of states of the GaS nanoribbon in comparison with that of monolayered GaS. We find that the band gap decreases notably in the presence of edges (E_g^{GGA}= 1.43 eV) [Figure 8.3b], projected density of states of edge atoms reveal that valence band and conduction band at the gap are mainly contributed by *s*, *p*-orbitals of Ga and partially by *p*-orbitals of S located at the edges. Thus, (a) the adsorptive interaction is facilitated through the channels of these frontier orbitals that are localized at the edges, and (b) the reduced band gap should result in better absorption of solar energy by the nanoscale layered GaS.

The straddling of the redox potentials of HER and OER by the valence and conduction bands of monolayer GaS means that surface sites of photoexcited GaS are capable of splitting water. The edge states, on the other hand, can result in partial splitting even without photoexcitation, though with a positive energy cost [Figure 8.3a]. While such dissociation is not energetically favorable, it shows that the interaction of H_2O with edges of the ribbon reduces this energy cost significantly because oxygen bonds chemically to GaS and H_2 is released. Thus, the H_2O-GaS interaction is strengthened by the edges, though splitting of water is not feasible indeed, without photoexcitation.

8.3.4 Polytypes of monolayered GaS

Depending on the sequence of Ga and S stacking, a monolayer of GaS exists in three other polytypic structures, namely, BABA (2H), BAAC ($4H_2$), and CABD ($4H_3$) apart from most stable BAAB ($4H_1$) [Figure 8.4a]. The energy difference between these polytypes and the most stable polytype (BAAB, ΔE) along with their band gaps calculated using HSE are listed in Table 8.3. Band alignment shows that the valence and conduction bands of all the forms of 2D-GaS straddle the redox potentials nicely, suggesting that 2D-GaS in any of its polytypes is expected to be a good photocatalyst [Figure 8.4b].

Table 8.3: Comparison of energies and band gap of different polytypes of monolayer GaS using HSE.

Polytype	ΔE (meV/f.u.)	E_g (eV)
$4H_1$	0	3.5
$4H_2$	5	3.65
$4H_3$	5	3.62
2H	5	3.64

8.3.5 Thickness dependent photocatalytic activity

Since the band gap of monolayered GaS is a bit high for efficient use of visible light, we have carried out a systematic analysis of the electronic structure of GaS of different thickness using HSE functionals. The band gap decreases with increase in the thickness as expected, making few layered GaS more efficient in absorption in the visible range. We have aligned valence and conduction bands on SHE scale to analyze its potential with thickness [Figure 8.3b]. The reference vacuum level for the bulk is obtained by converging E_{vacuum} with thickness (l). As thickness increases, the valence band moves up closer to vacuum giving a limit on thickness (l $<$ 8 layers, i.e., 5.5 nm) at which the valence and conduction bands straddle the redox

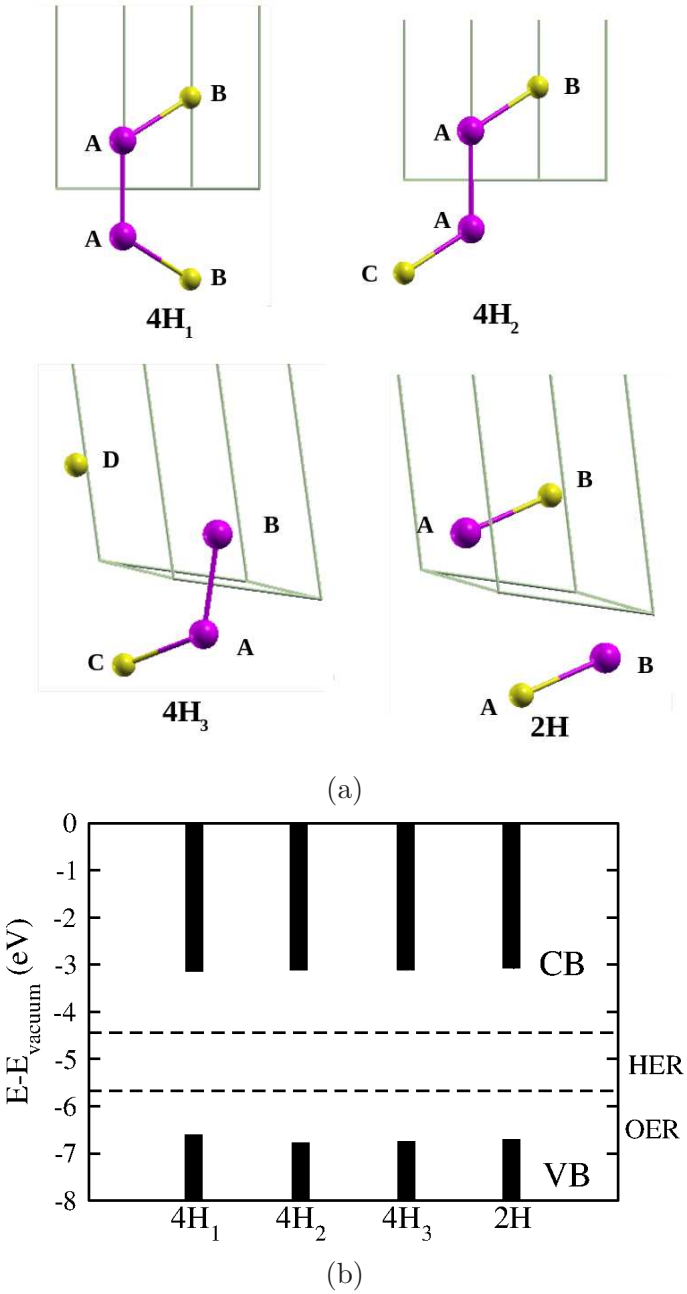

Figure 8.4: Structures (a), and band alignment (b) of different polytypes of monolayer GaS. Copyright (2015) by John Wiley & Sons, Inc.

potentials of HER and OER. Though the band gap of thicker layers of GaS is ideal for absorption in visible range, the valence band lies above the redox potential of OER for $l > 8$ making it inefficient for overall water splitting. However, we find that

the position of conduction band is above the hydrogen evolution potential for all thickness of GaS, making it feasible for photocatalytic hydrogen evolution with the help of sacrificial agents. Hence, a controlled synthesis of GaS with finite thickness and proper tailoring of edges is predicted to be useful in photocatalysis for overall water splitting.

8.3.6 Effect of interlayer stacking on photocatalytic activity

To understand the influence of interlayer stacking in multilayer GaS, we have studied different configurations of bilayer of GaS obtained with variation in the interlayer stacking [Table 8.4] by fixing the lattice constant equal to the experimental value of monolayer GaS (i.e., a_{exp} = 3.585 Å). Energetics reveal that BAAB ABBA stacking is the most stable one as observed experimentally. Electronic structure and band alignment on SHE using HSE functionals for all six structures show a small change in electronic band gap (0.01-0.48 eV, higher change for relatively unfavorable structure) maintaining the straddling of redox potentials by valence and conduction bands, indicating that different interlayer stacking does not affect the electronic properties significantly and hence the catalytic activity [Figure 8.5].

Table 8.4: Comparison of energies and band gap of configurations with different interlayer stacking in bilayer GaS.

Configuration	Stacking sequence	ΔE (meV/f.u.)	E_g^{HSE} (eV)
I	BAAB ABBA	0	2.89
II	BAAB ACCA	0.3	2.90
III	CAAC ABBA	0.3	2.90
IV	BAAB BAAB	25	2.71
V	BAAB BCCB	1.5	2.41
VI	BAAB CAAC	26	2.70

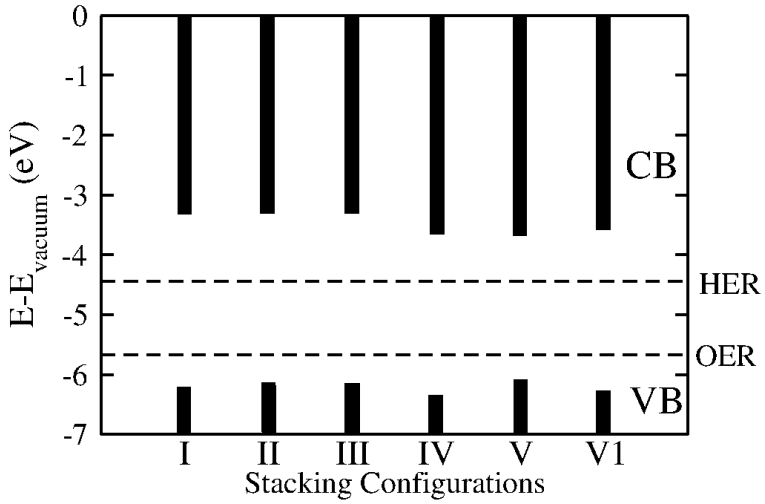

Figure 8.5: Band alignment of different interlayer stacking in bilayer GaS. Copyright (2015) by John Wiley & Sons, Inc.

8.3.7 Strain engineering of band gap*

We now move to pressure dependence of electronic properties of GaS. All the band gaps reported in this section are determined using GGA. We use the same terminology used in Johari *et al.* [205] and define here for reference (a) uniaxial strain along x-direction (xx) or y-direction (yy), (b) isotropic biaxial strain *i.e.* tensile (compressive) strains along x and y directions simultaneously denoted by +xx+yy (-xx-yy), (c) anisotropic biaxial strain *i.e.*, compressive strain along one direction (x) and tensile along the other (y) and vice versa (+xx-yy or -xx+yy).

We first present a comparative analysis of sensitivity of monolayer GaS to uniaxial strain and biaxial isotropic strains. We see that at zero external strain (experimental lattice parameter) monolayer GaS has a band gap of 2.52 eV. As the system is subjected to tensile strains (+xx, +xx+yy), there is a drastic decrease in the band gap confirming that the system is sensitive to external strains as predicted

*This work is in progress and yet to be published.

by Ma *et al* [208] due to strong electron-phonon coupling or mechanical deformation potential. However, we see that the system is more sensitive to (a) compressive strains (-xx/-xx-yy) and (b) isotropic biaxial strains compared to uniaxial strains, reflected by relatively steeper curves. We find similar results for anisotropic biaxial strains, hence our further analysis is focused on isotropic biaxial strains [Figure 8.6].

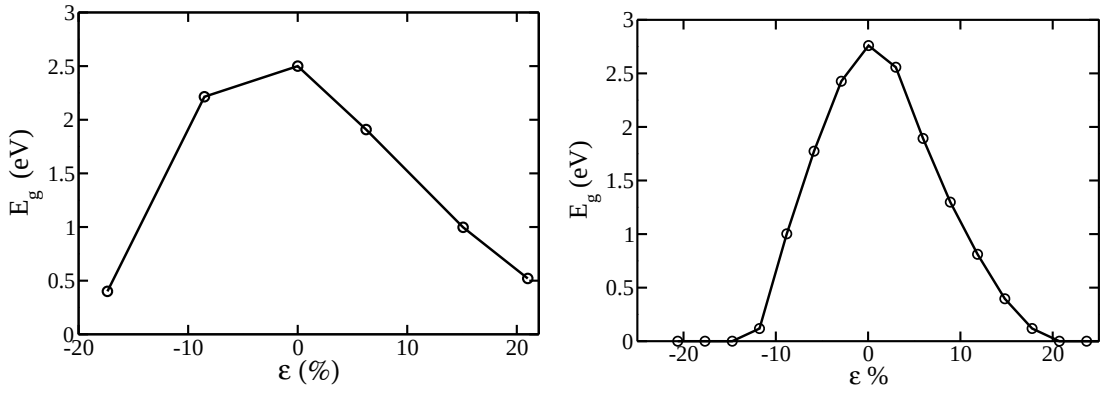

(a) (b)

Figure 8.6: Band gap-strain phase diagrams of monolayer GaS under uniaxial (xx/yy) (a) and biaxial (xx+yy/-xx-yy) (b) strains.

On application of isotropic biaxial strains, we see that the system undergoes a phase transition from semiconducting to metallic phase at $\varepsilon \leq$ -17% and $\varepsilon \geq$20%. For device application, it is essential to check the stability of the system, especially at such high strains. We have calculated phonon dispersions at different strains. Figure 8.7a shows the lowest frequency at each high symmetric point for different isotropic biaxial strains for BAAB stacking. We see that the system is locally stable only for strains, $\varepsilon \geq$-11% and $\varepsilon \leq$12%, weak instabilities emerging at M and K points on further increment of compressive or tensile strains. For the strains at which S-M transition is predicted, the instability gets more pronounced revealing that the above phase transition is not achievable merely by an application of external strains.

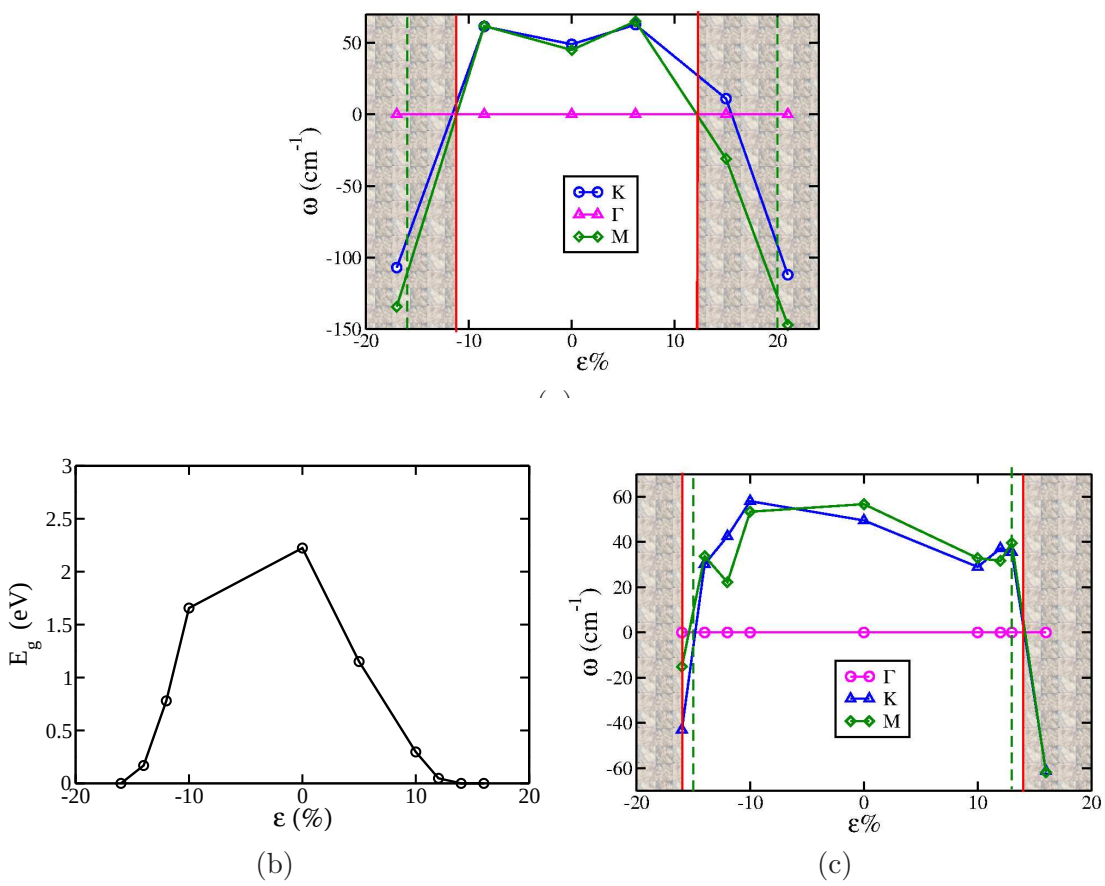

(b) (c)

Figure 8.7: Stability phase diagram for BAAB stacking (a), band gap-strain (b), and stability (c) phase digrams for BAAC polytype of monolayer GaS (green dotted line indicates the critical strains for S-M phase transition; red lines and region shaded beyond it indicate the strains at which the system becomes unstable.

Since all the polytypes of GaS are energetically very similar, we determine their band gap-strain phase diagrams on application of isotropic biaxial strains to examine the existence of S-M transition. We find that CABD and BABA are also unstable in their metallic phase except BAAC, which undergoes a S-M transition at relatively lower strains $\varepsilon \leq$-16% and $\varepsilon \geq$13% [Figure 8.7b. For a small window of external strains, the metallic phase remains stable [Figure 8.7c]. Comparison of energetics of BAAB and BAAC polytypes at different strains reveal that the BAAC becomes relatively more stable with the application of small compressive strains (-4%), indicating a possible structural phase transition from BAAB to BAAC [Figure 8.8].

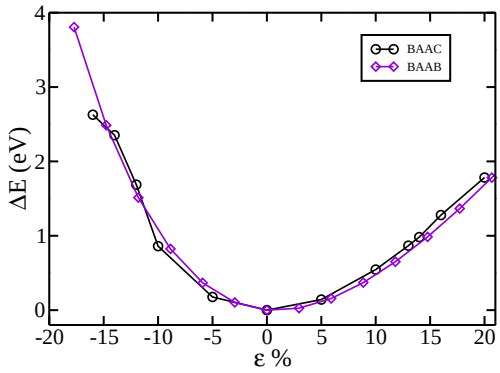

Figure 8.8: Comparison of energies of BAAB and BAAC polytypes at different external strains.

8.4 Conclusions

Using first-principles calculations of the thickness-dependent electronic structure of layered GaS and its polytypes, we show that ultra-thin (thickness < 5.5 nm) films of GaS exhibit electronic structure with valence and conduction bands that straddle the redox potentials of hydrogen evolution and OER, making them suitable as photocatalysts for splitting of water and conversion of solar energy into chemical energy in the form of hydrogen. We show that (a) the band gap of a GaS film decreases with thickness making it more efficient in absorption of wide range of solar spectrum, though its valence conduction band edges become unfavorable for OER for thickness > 5.5 nm, and (b) the edges of nano-scale flakes of GaS interact more effectively with water molecule leading to their splitting. Thus, we predict that GaS synthesized with controlled thickness and edges should be an efficient photocatalyst for solar splitting of water. Our prediction is partially verified by experiments that show moderate hydrogen evolution in presence of different sacrificial agents supporting that GaS acts as both light absorption and hydrogen evolution site. We have

shown that the band gap of monolayered GaS can be tuned with external strain owing to a strong electron-phonon coupling, with a possible structural phase transition from polytype BAAB to polytype BAAC upon application of compressive strains.

Summary

The central theme of this dissertation has been to explore and tune the properties of bulk and nano-scale materials towards the development of new functionality and/or devices for applications that are more energy efficient and eco-friendly. The materials studied in this thesis are not only technologically important, but are also fundamentally interesting as they exhibit unusual phenomena involving fascinating physics. We have used first-principles density functional theory and model-based Molecular Dynamics simulations in our theoretical analysis. We have summarized the work in this thesis in a schematic below [Figure I].

The thesis is divided into three parts based on the functionality of the materials explored: (1) materials for memory, (2) materials for environment and (3) materials for photocatalyst.

Materials for Memory

We have shown that the ferroelectric ordering in ultra-thin films of $PbTiO_3$ is often inhomogeneous, sensitive to and hence tunable to film thickness, epitaxial strain and nature of electrodes. The origin of domain stability lies in strong strain-phonon coupling between ferroelectric thin-film and the substrate. We also demonstrated a diffuse phase transition due to the domain structure that forms in the presence of imperfect electrodes. The effect of domain walls on dielectric properties in ABO_3 perovskites ($PbTiO_3$ and $BaTiO_3$) are sensitive to the A cation due to difference in

their bulk structures. The presence of domain walls separating domains of opposite polarization (180° domain structure) leads to giant dielectric response of $PbTiO_3$, while it does not significantly affect dielectric properties of $BaTiO_3$. Our findings are relevant to use of ferroelectric oxides in nano-scale devices with applications in ultra-high density memory devices.

Materials for Environment

We find that a large surface area in 2-D honeycomb lattices (graphene and 2D-ZnO) facilitate the adsorption of toxic molecules (pesticide and H_2S), which can be further enhanced by the presence of defects. We have shown that a pesticide adsorption on graphene is thermodynamically feasible due to water-mediated interactions, and hence its removal from water is possible through the formation of graphene-water-pesticide precipitate. We find that the presence of defects *i.e.*, N-substitution and O-vacancies in 2D-ZnO facilitates the capture of H_2S and its splitting to generate H_2. The present study reveals the richness of interactions of these 2-D materials with molecular systems, and opens a way for further research in this important field of environment friendly applications.

We report that N-substitution in V_2O_3 lowers the energy of high temperature metallic corundum phase relative to antiferromagnetic phase leading to reduction in the metal-to-insulator transition temperature observed in experiments. This finding indicates that V_2O_3 is highly sensitive to anion substitution, and this could be useful in tuning properties for applications in gas sensing based on metal-insulator transition edge sensing.

Materials for Energy Conversion

We find that aliovalent anion co-substitution (P, Cl and N, F) in CdS and ZnS leads to increase in their visible-light response and hydrogen evolution through reduction

in band gap. This is mainly due to the emergence of an isolated sub-band of p-states of less electronegative trivalent anion at the top of valence band, while maintaining the position of conduction band desirable for water splitting. Our work also reveals that the effects of anion co-substitution on electronic structure are quite sensitive to the host lattice structure, specific host compound and choice of dopants.

We predict that a few layered GaS (thickness < 5.5 nm) and its polytypes exhibit electronic structure with valence and conduction bands that straddle the redox potentials of hydrogen evolution reaction and oxygen evolution reaction that govern water splitting, making them suitable as photocatalysts. The solar-light response of GaS can be further improved by external strain due to a strong electron-phonon coupling it exhibits. Thus, GaS synthesized with controlled thickness, edges and external strain should be an efficient photocatalyst for solar splitting of water.

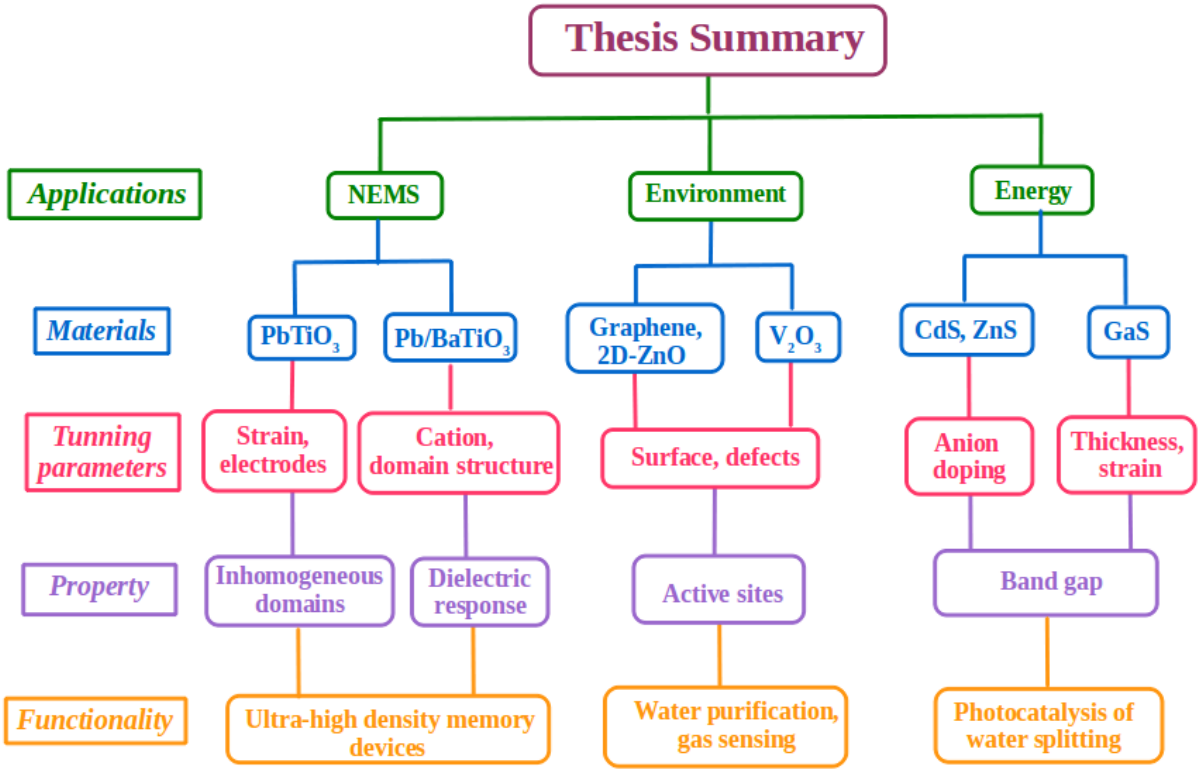

Figure I: Schematic summarizing the work presented in the thesis.

Bibliography

[1] S. M. Maliyekkal *et al.*, Small **9**, 273 (2013).

[2] J. Scott, Science **315**, 954 (2007).

[3] J. F. Scott, F. D. Morrisona, M. Miyakea, and P. Zubko, Ferroelectrics **336**, 237 (2006).

[4] M. Dawber, K. M. Rabe, and J. F. Scott, Rev. Mod. Phys. **77**, 1083 (2005).

[5] K. J. Choi *et al.*, Science **306**, 1005 (2004).

[6] J. F. Scott and C. A. P. De Araujo, Science **246**, 1400 (1989).

[7] C. H. Ahn, K. M. Rabe, and J.-M. Triscone, Science **303**, 488 (2004).

[8] D. D. Fong *et al.*, Science **304**, 1650 (2004).

[9] Y. Yoneda *et al.*, J. Appl. Phys. **83**, 2458 (1998).

[10] G. Catalan *et al.*, Nature Mater. **10**, 963 (2011).

[11] G. Catalan, J. Seidel, R. Ramesh, and J. F. Scott, Rev. Mod. Phys. **84**, 119 (2012).

[12] S. Kouser, U. V. Waghmare, and N. Tit, Phys. Chem. Chem. Phys. **16**, 10719 (2014).

[13] M. M. Khin *et al.*, Energy Environ. Sci. **5**, 8075 (2012).

[14] M. Bosetti, A. Masse, E. Tobin, and M. Cannas, Biomaterials **23**, 887 (2002).

[15] L. Liu, C. Zhao, and F. Yang, Water research **46**, 1969 (2012).

[16] H. F. Lin, R. Ravikrishna, and K. Valsaraj, Sep. Purif. Technol. **28**, 87 (2002).

[17] O. Schmidt *et al.*, Superlattices Microstruct. **39**, 8 (2006).

[18] O. Schmidt *et al.*, Jpn. J. Appl. Phys. **44**, 7271 (2005).

[19] E. Comini *et al.*, Appl. Phys. Lett. **81**, 1869 (2002).

[20] S. Bosso and J. Enzweiler, Water research **36**, 4795 (2002).

[21] J. Barber, Chem. Soc. Rev. **38**, 185 (2009).

[22] K. Maeda and K. Domen, J. Phys. Chem. Lett. **1**, 2655 (2010).

[23] K. H. Akira Fujishma, Nature **232**, 37 (1972).

[24] K. Domen, A. Kudo, and T. Onishi, J. Catal. **102**, 92 (1986).

[25] K. Domen, S. Naito, T. Onishi, and K. Tamaru, Chem. Phys. Lett. **92**, 433 (1982).

[26] A. Kudo, K. Domen, K. Maruya, and T. Onishi, Chem. Phys. Lett. **133**, 517 (1987).

[27] H. Kato and A. Kudo, Catal. Lett. **58**, 153 (1999).

[28] A. Kudo and H. Kato, Chem. Phys. Lett. **331**, 373 (2000).

[29] K. Zhang and L. Guo, Catal. Sci. Technol. **3**, 1672 (2013).

[30] Y.-H. Zhang *et al.*, Comput. Mater. Sci. **69**, 222 (2013).

[31] S. R. Lingampalli, U. K. Gautam, and C. N. R. Rao, Energy Environ. Sci. **6**, 3589 (2013).

[32] U. Maitra *et al.*, Angew. Chem. Int. Ed. **52**, 13057 (2013).

[33] U. Maitra, S. R. Lingampalli, and C. N. R. Rao, Curr. Sci. **106**, 518 (2014).

[34] U. Gupta *et al.*, APL Mater. **2**, 092802 (2014).

[35] U. Gupta *et al.*, Chem. Asian J. **9**, 1311 (2014).

[36] H. L. Zhuang and R. G. Hennig, J. Phys. Chem. C **117**, 20440 (2013).

[37] J. F. Reber and K. Meier, J. Phys. Chem. **88**, 5903 (1984).

[38] M. Born and J. R. Oppenheimer, Ann. d. Physik **84**, 457 (1927).

[39] P. Hohenberg and W. Kohn, Phys. Rev. **136**, B864 (1964).

[40] W. Kohn and L. J. Sham, Phys. Rev. **140**, A1133 (1965).

[41] D. M. Ceperley and B. Alder, Phys. Rev. Lett. **45**, 566 (1980).

[42] J. P. Perdew and A. Zunger, Phys. Rev. B **23**, 5048 (1981).

[43] J. P. Perdew and W. Yue, Phys. Rev. B **33**, 8800 (1986).

[44] J. P. Perdew, K. Burke, and M. Ernzerhof, Phys. Rev. Lett. **77**, 3865 (1996).

[45] P. Giannozzi *et al.*, J. Phys. Condens. Matter **21**, 395502 (2009).

[46] X. Gonze *et al.*, Comput. Mater. Sci. **25**, 478 (2002).

[47] D. Vanderbilt, Phys. Rev. B **41**, 7892 (1990).

[48] I. E. Dzyaloshinskii, E. Lifshitz, and L. P. Pitaevskii, Sov. Phys. Usp. **4**, 153 (1961).

[49] S. Grimme, J. Comput. Chem. **27**, 1787 (2006).

[50] A. Tkatchenko and M. Scheffler, Phys. Rev. Lett. **102**, 073005 (2009).

[51] C. Adamo and V. Barone, J. Chem. Phys. **110**, 6158 (1999).

[52] R. M. Sternheimer, Phys. Rev. **96**, 951 (1954).

[53] S. Baroni, S. de Gironcoli, A. Dal Corso, and P. Giannozzi, Rev. Mod. Phys. **73**, 515 (2001).

[54] X. Gonze and C. Lee, Phys. Rev. B **55**, 10355 (1997).

[55] U. V. Waghmare and K. M. Rabe, Phys. Rev. B **55**, 6161 (1997).

[56] T. Nishimatsu, U. V. Waghmare, Y. Kawazoe, and D. Vanderbilt, Phys. Rev. B **78**, 104104 (2008).

[57] U. V. Waghmare, E. J. Cockayne, and B. P. Burton, Ferroelectrics **291**, 187 (2003).

[58] S. Kouser, T. Nishimatsu, and U. V. Waghmare, Phys. Rev. B **88**, 064102 (2013).

[59] T. J. Yang, V. Gopalan, P. J. Swart, and U. Mohideen, Phys. Rev. Lett. **82**, 4106 (1999).

[60] D. Lee *et al.*, Phys. Rev. B **80**, 060102 (2009).

[61] C.-L. Jia *et al.*, Science **331**, 1420 (2011).

[62] C. T. Nelson *et al.*, Nano Lett. **11**, 828 (2011).

[63] R. K. Vasudevan *et al.*, Nano Lett. **12**, 5524 (2012).

[64] A. Kholkin *et al.*, Adv. Funct. Mater. **21**, 1977 (2011).

[65] M. Tyunina *et al.*, Adv. Funct. Mater. **23**, 467 (2013).

[66] S. Bin-Omran, I. Kornev, I. Ponomareva, and L. Bellaiche, Phys. Rev. B **81**, 094119 (2010).

[67] R. D. King-Smith and D. Vanderbilt, Phys. Rev. B **49**, 5828 (1994).

[68] J. Paul, T. Nishimatsu, Y. Kawazoe, and U. V. Waghmare, Phys. Rev. Lett. **99**, 077601 (2007).

[69] D. D. Fong *et al.*, Phys. Rev. Lett. **96**, 127601 (2006).

[70] N. A. Pertsev, A. G. Zembilgotov, and A. K. Tagantsev, Phys. Rev. Lett. **80**, 1988 (1998).

[71] D. G. Schlom *et al.*, Annu. Rev. Mater. Res. **37**, 589 (2007).

[72] A. G. Zembilgotov, N. A. Pertsev, H. Kohlstedt, and R. Waser, J. Appl. Phys. **91**, 2247 (2002).

[73] J. H. Haeni *et al.*, Nature **430**, 758 (2004).

[74] Y. L. Li and L. Q. Chen, Appl. Phys. Lett. **88**, 072905 (2006).

[75] Y. L. Li, S. Y. Hu, Z. K. Liu, and L. Q. Chen, Appl. Phys. Lett. **78**, 3878 (2001).

[76] G. Sheng *et al.*, J. Appl. Phys. **108**, 084113 (2010).

[77] L. Hong and A. K. Soh, Mech. Mater. **43**, 342 (2011).

[78] V. Garcia *et al.*, Nature **460**, 81 (2009).

[79] A. M. Glazer, S. A. Mabud, and R. Clarke, Acta Crystallogr. **34**, 1060 (1978).

[80] S. D. Bond, B. J. Leimkuhler, and B. B. Laird, J. Comput. Phys. **151**, 114 (1999).

[81] L. Menten and M. Michaelis, Biochem Z **49**, 333 (1913).

[82] J. H. Kim, J. Jang, and W.-C. Zin, Langmuir **17**, 2703 (2001).

[83] S. Tinte and M. G. Stachiotti, Phys. Rev. B **64**, 235403 (2001).

[84] J. Junquera and P. Ghosez, Nature **422**, 506 (2003).

[85] E. C. V. Tarasenko, Sov. Phys. JETP **56**, 618 (1982).

[86] A. M. Bratkovsky and A. P. Levanyuk, Phys. Rev. Lett. **84**, 3177 (2000).

[87] A. M. Bratkovsky and A. P. Levanyuk, Phys. Rev. Lett. **94**, 107601 (2005).

[88] S. Chattopadhyay *et al.*, J. Mater. Res. **17**, 669 (2002).

[89] T. Nishimatsu *et al.*, J. Phys. Soc. Jpn. **81**, 124702 (2012).

[90] A. Kumar, K. M. Rabe, and U. V. Waghmare, Phys. Rev. B **87**, 024107 (2013).

[91] W. Zhong, D. Vanderbilt, and K. M. Rabe, Phys. Rev. Lett. **73**, 1861 (1994).

[92] T. H. Kim *et al.*, Appl. Phys. Lett. **95**, 262902 (2009).

[93] A. J. Schellekens *et al.*, Nat. Commun. **3**, 847 (2012).

[94] C.-L. Jia *et al.*, Science **331**, 1420 (2011).

[95] C. T. Nelson *et al.*, Nano Lett. **11**, 828 (2011).

[96] P. Maksymovych *et al.*, Nano Lett. **12**, 209 (2012).

[97] M. Tyunina *et al.*, Adv. Funct. Mater. **23**, 467 (2013).

[98] Z. Jiang *et al.*, Phys. Rev. B **89**, 214113 (2014).

[99] J. Guyonnet, I. Gaponenko, S. Gariglio, and P. Paruch, Adv. Mater. **23**, 5377 (2011).

[100] S. Farokhipoor and B. Noheda, Phys. Rev. Lett. **107**, 127601 (2011).

[101] G. D. Cole *et al.*, Nat. Commun. **2**, 231 (2011).

[102] M. Daraktchiev, G. Catalan, and J. F. Scott, Phys. Rev. B **81**, 224118 (2010).

[103] T. Sluka, A. K. Tagantsev, P. Bednyakov, and N. Setter, Nat. Commun. **4**, 1808 (2013).

[104] B. Meyer and D. Vanderbilt, Phys. Rev. B **65**, 104111 (2002).

[105] S. Pöykkö and D. J. Chadi, Appl. Phys. Lett. **75**, 2830 (1999).

[106] L. He and D. Vanderbilt, Phys. Rev. B **68**, 134103 (2003).

[107] M. Li *et al.*, Phys. Rev. B **90**, 054106 (2014).

[108] J. C. Wojdeł and J. Íñiguez, Phys. Rev. Lett. **112**, 247603 (2014).

[109] T. Pradeep *et al.*, Thin Solid Films **517**, 6441 (2009).

[110] A. K. Leight and R. F. Van Dolah, Environ. Toxicol. Chem. **18**, 958 (1999).

[111] S. L. Simonich and R. A. Hites, Environmental Science & Technology **29**, 2905 (1995).

[112] A. Sreekumaran Nair and T. Pradeep, Curr. Sci. **84**, 1560 (2003).

[113] W. Chen, L. Duan, and D. Zhu, Environ. Sci. Technol. **41**, 8295 (2007).

[114] M. L. Schipper *et al.*, Nat. Nanotechnol. **3**, 216 (2008).

[115] A. Magrez *et al.*, Nano lett. **6**, 1121 (2006).

[116] K. S. Novoselov *et al.*, Science **306**, 666 (2004).

[117] N. Kurra, A. A. Sagade, and G. U. Kulkarni, Adv. Funct. Mater. **21**, 3836 (2011).

[118] S. Stankovich *et al.*, Nature **442**, 282 (2006).

[119] Z. Liu, J. T. Robinson, X. Sun, and H. Dai, J. Am. Chem. Soc. **130**, 10876 (2008).

[120] F. Schedin *et al.*, Nat. Mater. **6**, 652 (2007).

[121] R. S. Sundaram *et al.*, Adv. Matter. **20**, 3050 (2008).

[122] L. Tang *et al.*, Adv. Funct. Mater. **19**, 2782 (2009).

[123] N. Jung *et al.*, ACS Nano **4**, 7005 (2010).

[124] C. Rao, A. Sood, K. Subrahmanyam, and A. Govindaraj, Angew. Chem. Int. Ed. **48**, 7752 (2009).

[125] G. K. Dimitrakakis, E. Tylianakis, and G. E. Froudakis, Nano lett. **8**, 3166 (2008).

[126] C. Liu, F. Li, L.-P. Ma, and H.-M. Cheng, Adv. Mater. **22**, E28 (2010).

[127] D. R. Dreyer, H.-P. Jia, and C. W. Bielawski, Angew. Chem. Ind. Ed. **122**, 6965 (2010).

[128] Y. Zhu *et al.*, Adv. Mater. **22**, 3906 (2010).

[129] W. Hu *et al.*, ACS Nano **4**, 4317 (2010).

[130] J. Chen *et al.*, Anal. Chim. Acta **678**, 44 (2010).

[131] T. Sreeprasad *et al.*, ACS Appl. Mater. Interfaces **3**, 2643 (2011).

[132] V. Chandra *et al.*, ACS nano **4**, 3979 (2010).

[133] W. Gao *et al.*, ACS Appl. Mater. Interfaces **3**, 1821 (2011).

[134] G. Zhao *et al.*, Adv. Mater. **23**, 3959 (2011).

[135] S. Memon, N. Memon, S. Memon, and Y. Latif, J. Hazard. Mater. **186**, 1696 (2011).

[136] J. Weber *et al.*, Sci. Total Environ. **408**, 2966 (2010).

[137] X. Zhao and H.-M. Hwang, Arch. Environ. Contam. Toxicol. **56**, 646 (2009).

[138] C. Sujatha, S. Nair, and J. Chacko, Water Res. **33**, 109 (1999).

[139] F. Tuinstra and J. L. Koenig, The Journal of Chemical Physics **53**, 1126 (1970).

[140] R. G. Baughman, S. K. Jorgensen, and R. A. Jacobson, Journal of Agricultural and Food Chemistry **26**, 576 (1978).

[141] J. Lindenmann *et al.*, Diving Hyperb. Med. **40**, 213 (2010).

[142] E. R. Parivash Dezham and D. Jenkins, Int. J. Quant. Chem. **60**, 514 (1988).

[143] Q.-L. Tang, Int. J. Quant. Chem. **113**, 1992 (2013).

[144] J. A. Rodriguez *et al.*, J. Am. Chem. Soc. **122**, 12362 (2000).

[145] J. Zaman and A. Chakma, Fuel Process. Technol. **41**, 159 (1995).

[146] G. F. Fine, L. M. Cavanagh, A. Afonja, and R. Binions, Sensors **10**, 5469 (2010).

[147] M. Hulko, I. Hospach, N. Krasteva, and G. Nelles, Sensors **11**, 5968 (2011).

[148] C. Li *et al.*, Appl. Phys. Lett. **82**, 1613 (2003).

[149] X. Zou *et al.*, Nano Lett. **13**, 3287 (2013).

[150] D. N. Huyen, N. T. Tung, N. D. Thien, and L. H. Thanh, Sensors **11**, 1924 (2011).

[151] K. K. Kasem, J. Mater. Sci. Technol. **26**, 619 (2010).

[152] O. Bikondoa *et al.*, Nat. Mater. **5**, 189 (2006).

[153] J. A. Rodriguez, S. Chaturvedi, M. Kuhn, and J. Hrbek, J. Phys. Chem. B **102**, 5511 (1998).

[154] R. Saha *et al.*, ChemPhysChem **14**, 2672 (2013).

[155] D. Thomas, J. Phys. Chem. Solids **15**, 86 (1960).

[156] D. Reynolds, D. Look, and B. Jogai, Solid State Commun. **99**, 873 (1996).

[157] D. C. Reynolds *et al.*, Phys. Rev. B **60**, 2340 (1999).

[158] Y. Chen *et al.*, J. Appl. Phys. **84**, 3912 (1998).

[159] A. Ohtomo *et al.*, Appl. Phys. Lett. **72**, 2466 (1998).

[160] A. Ohtomo *et al.*, Appl. Phys. Lett. **75**, 4088 (1999).

[161] T. Makino *et al.*, Appl. Phys. Lett. **77**, 1632 (2000).

[162] Z. Tu, J. Comput. Theor. Nanosci. **7**, 1182 (2010).

[163] M.-W. Ahn *et al.*, Appl. Phys. Lett. **93**, 263103 (2008).

[164] S. C. Lee *et al.*, Sensors **13**, 3889 (2013).

[165] V. I. Hegde *et al.*, Surf. Sci. **621**, 168 (2014).

[166] D. C. Langreth and M. J. Mehl, Phys. Rev. B **28**, 1809 (1983).

[167] J. P. Perdew, Phys. Rev. Lett. **55**, 1665 (1985).

[168] M. Topsakal, S. Cahangirov, E. Bekaroglu, and S. Ciraci, Phys. Rev. B **80**, 235119 (2009).

[169] J. C. Meyer *et al.*, Nano lett. **8**, 3582 (2008).

[170] F. A. Cotton, Acc. Chem. Res. **2**, 240 (1969).

[171] J. Sheldon, Australian Journal of Chemistry **17**, 1191 (1964).

[172] N. Kumar *et al.*, ChemPhysChem **16**, 2745 (2015).

[173] H. Wich, Kristall und Technik **10**, K57 (1975).

[174] P. Edwards, T. Ramakrishnan, and C. Rao, J. Phys. Chem. **99**, 5228 (1995).

[175] K. D. Irwin and G. C. Hilton, *Transition-edge sensors* (Springer, ADDRESS, 2005), Vol. n/a, pp. 63–150.

[176] E. Strelcov, Y. Lilach, and A. Kolmakov, Nano lett. **9**, 2322 (2009).

[177] C. Chen, X. Yi, X. Zhao, and B. Xiong, Sensor. Actuat. A: Phys. **90**, 212 (2001).

[178] W. Zhang *et al.*, J. Phys. Chem. C **118**, 12837 (2014).

[179] R. J. O. Mossanek and M. Abbate, Phys. Rev. B **75**, 115110 (2007).

[180] P. D. Dernier and M. Marezio, Phys. Rev. B **2**, 3771 (1970).

[181] J. Pan *et al.*, ChemPhysChem **16**, 1502 (2015).

[182] A. Butler, Coord. Chem. Rev. **187**, 17 (1999).

[183] S. Kouser *et al.*, Angew. Chem. Int. Ed. **127**, 8267 (2015).

[184] A. Kudo and Y. Miseki, Chem. Soc. Rev. **38**, 253 (2009).

[185] I. Tsuji, H. Kato, H. Kobayashi, and A. Kudo, J. Am. Chem. Soc. **126**, 13406 (2004).

[186] A. Kudo and M. Sekizawa, Chem. Comm. **15**, 1371 (2000).

[187] J. F. Reber and M. Rusek, J. Phys. Chem. **90**, 824 (1986).

[188] H. Qin, W. Li, Y. Xia, and T. He, ACS Appl. Mater. Interfaces **3**, 3152 (2011).

[189] Z. Zhang *et al.*, R. Soc. Chem. Adv. **3**, 7215 (2013).

[190] S. Lingampalli and C. Rao, J. Mater. Chem. A **2**, 7702 (2014).

[191] N. Kumar *et al.*, Inorg. Chem. **52**, 10512 (2013).

[192] N. Kumar *et al.*, J. Phys. Condens. Matter **25**, 345901 (2013).

[193] H. Irie, Y. Watanabe, and K. Hashimoto, J. Phys. Chem. B **107**, 5483 (2003).

[194] G. Liu *et al.*, J. Am. Chem. Soc. **131**, 12868 (2009).

[195] S.-H. Wei and S. B. Zhang, Phys. Rev. B **62**, 6944 (2000).

[196] B. S. Zou, R. B. Little, J. P. Wang, and M. A. El-Sayed, Int. J. Quantum Chem **72**, 439 (1999).

[197] R. Grau-Crespo, S. Hamad, C. Catlow, and N. De Leeuw, J. Phys. Condens. Matter **19**, 256201 (2007).

[198] R.-Q. Zhu, Acta Crystallogr. Sect. A **67**, m1416 (2011).

[199] M. S. Bharara, C. H. Kim, S. Parkin, and D. A. Atwood, Polyhedron **24**, 865 (2005).

[200] H. Derin and K. Kantarli, Surf. Interface Anal. **41**, 61 (2009).

[201] S. Desgreniers, L. Beaulieu, and I. Lepage, Phys. Rev. B **61**, 8726 (2000).

[202] K. Kokh *et al.*, Crystal Research and Technology **46**, 327 (2011).

[203] D. J. Late *et al.*, Adv. Funct. Mater. **22**, 1894 (2012).

[204] H. Tanaka, J. Zhang, and T. Kawai, Phys. Rev. Lett. **88**, 027204 (2001).

[205] P. Johari and V. B. Shenoy, ACS Nano **6**, 5449 (2012).

[206] G. Cocco, E. Cadelano, and L. Colombo, Phys. Rev. B **81**, 241412 (2010).

[207] H.-H. Park *et al.*, J. Mater. Chem. **21**, 657 (2011).

[208] Y. Ma *et al.*, Phys. Chem. Chem. Phys. **15**, 7098 (2013).

[209] H. J. Monkhorst and J. D. Pack, Phys. Rev. B **13**, 5188 (1976).

[210] P. Hu *et al.*, Nano lett. **13**, 1649 (2013).

[211] J. L. Freeouf and J. M. Woodall, Appl. Phys. Lett. **39**, 727 (1981).